Interacting Bose-Fermi mixtures in optical lattices

Dissertation

zur Erlangung des Grades

Doktor

der Naturwissenschaften

am Fachbereich Physik, Mathematik und Informatik

der Johannes Gutenberg-Universität

in Mainz

Thorsten Best

geboren in Bonn

Mainz, den 11. Oktober 2010

D77

1. Berichterstatter:
2. Berichterstatter:

Datum der mündlichen Prüfung: 27. Mai 2011

Abstract

In this thesis, we investigate mixtures of quantum degenerate Bose and Fermi gases of neutral atoms in threedimensional optical lattices. Feshbach resonances allow to control interspecies interactions in these systems precisely, by preparing suitable combinations of internal atomic states and applying external magnetic fields. This way, the system behaviour can be tuned continuously from mutual transparency to strongly interacting correlated phases, up to the stability boundary. The starting point for these investigations is the spin-polarized fermionic band insulator. The properties of this non-interacting system are fully determined by the Pauli exclusion principle for the occupation of states in the lattice. A striking demonstration of the latter can be found in the antibunching of the density-density correlation of atoms released from the lattice. If bosonic atoms are added to this system, isolated heteronuclear molecules can be formed on the lattice sites via radio-frequency stimulation. The efficiency of this process hints at a modification of the atom number distribution over the lattice caused by interspecies interaction. In the following, we investigate systems with tunable interspecies interaction. To this end, a method is developed which allows to assess the various contributions to the system Hamiltonian both qualitatively and quantitatively by following the quantum phase diffusion of the bosonic matter wave. Besides a modification of occupation number statistics, these measurements show a significant renormalization of the bosonic Hubbard parameters. The final part of the thesis considers the implications of this renormalization effect on the many particle physics in the mixture. Here, we demonstrate how the quantum phase transition from a bosonic superfluid to a Mott insulator state is shifted towards considerably shallower lattices due to renormalization.

Zusammenfassung

In dieser Arbeit untersuchen wir Mischungen quantenentarteter Bose- und Fermigase neutraler Atome in dreidimensionalen optischen Gittern. Dabei erlauben Feshbach-Resonanzen, die Interspezies-Wechselwirkung in diesen Systemen präzise durch Präparieren geeigneter Kombinationen atomarer Zustände und Anlegen externer Magnetfelder zu kontrollieren. Damit lässt sich das Systemverhalten stetig von wechselseitiger Transparenz zu stark wechselwirkenden korrelierten Phasen bis hin zur Grenze der Stabilität einstellen. Den Ausgangspunkt der Untersuchungen bildet der spinpolarisierte fermionische Bandisolator, ein wechselwirkungsfreies System, dessen Eigenschaften allein durch das Pauli-Prinzip bei der Besetzung der zur Verfügung stehenden Zustände im optischen Gitter bestimmt sind, Dieses lässt sich eindrucksvoll anhand des Antibunching in der Dichte-Dichte-Korrelation aus dem Gitter frei gelassener Atome beobachten. Fügt man dem System bosonische Atome hinzu, so lassen sich durch Radiofrequenzstimulation auf den Gitterplätzen isolierte heteronukleare Moleküle bilden. Die Effizienz dieses Prozesses gibt Hinweise darauf, dass die Atomzahlverteilung über das Gitter aufgrund der Interspezies-Wechselwirkung deutlich modifiziert sein könnte. Im folgenden werden Systeme mit einstellbarer Interspezies-Wechselwirkung untersucht. Dabei wird zunächst eine Methode entwickelt, die unterschiedlichen Beiträge des System-Hamilton-Operators anhand der Quantenphasendiffusion der bosonischen Materiewelle qualitativ und quantitativ zu erfassen. Dabei zeigt sich neben der Modifikation der Besetzungszahlstatistik eine signifikante Renormierung der bosonischen Hubbard-Parameter. Diese kann anhand der wechselwirkungsinduzierten Änderung der Wannier-Orbitale verstanden werden. Die Arbeit schließt mit einer Untersuchung der Auswirkung dieses Renormierungseffekts auf die Vielteilchenphysik des Mischungssystems. Dabei wird gezeigt, wie sich der Quantenphasenübergang zwischen dem bosonischen Superfluid und dem Mott-Isolator-Zustand aufgrund der Renormierung zu wesentlich flacheren Gittern hin verschiebt.

Contents

Introductory remarks

Degenerate Bose-Fermi mixtures

In recent years, quantum physics has made remarkable progress on the way from a somewhat obscure way of calculating properties of the microcosm, to mainstream technology. Manifestly quantum systems can nowadays be prepared in many laboratories all around the world, they can be manipulated coherently, and their behaviour can be analyzed in great detail. Much has been learned from these systems about basic ingredients of quantum physics, such as superposition, coherence, entanglement and many more. Interacting quantum many-body systems are of special interest in this context, due to the striking effects that strong correlations of the components may have on the behaviour of the total system. The new field of quantum simulation has emerged in this context, which aims at gaining understanding about many-body quantum systems with strong correlations from experiments under suitably tailored and well-controlled conditions, where reliable approximative theoretical treatments are rare, and full numerical calculations hit the wall of practical feasibility in terms of computational complexity.

The ability to experimentally create and control such quantum systems is strongly linked to the progress in the field of cooling and trapping of neutral atoms in recent years. Ultracold atoms seem to be ideal candidates for quantum simulation, as they allow to reproducibly prepare systems of adjustable size, ranging from the single-particle level all the way to truly mesoscopic samples. Furthermore, they offer enough internal degrees of freedom to build highly nontrivial model systems, yet still few enough to maintain full control over the initial quantum state of the system. Even better, they often come with tunable interactions, and the associated timescales are very convenient from an experimental point of view. Finally, a well-equipped toolbox of manipulation and detection techniques exists for these systems, while new methods allowing for ever more insight are still being developed on a regular basis.

An additional twist has been added to the field with the introduction of optical lattices, which are periodic potentials created by light intensity patterns. These periodic potentials lead to the emergence of a band structure and thereby open up the way to quantum simulation of condensed matter physics, which naturally plays on a lattice structure, namely the crystal lattice. An important step on the way towards this goal has been the realization of the Bose-Hubbard model Hamiltonian with neutral bosonic Rubidium atoms in a threedimensional optical lattice potential.

In the beginning, experimental research has focussed exclusively on bosonic quantum gases. As experimental capabilities have evolved, fermionic quantum gases, and, more recently, mixed species systems have come into reach experimentally. In this work, we combine a resonantly interacting Bose-Fermi mixture with a threedimensional optical lattice. Thereby, we realize for the first time an instance of the Bose-Fermi-Hubbard model system with tunable interactions. On the way, we clarify the roles of intra- and interspecies interactions, occupation numbers of individual lattice sites, inhomogeneiety and three-body losses, revealing the importance of effects beyond the usual single-band approximation. We demonstrate how these effects can, to a large degree, be understood in terms of a renormalized effective single-band Bose-Fermi-Hubbard system.

Outline of the thesis

In the first chapter of this thesis, we will describe the experimental apparatus and procedure needed for the preparation, manipulation and detection of ultracold Bose-Fermi mixtures made up of ^{87}Rb and ^{40}K atoms. Chapter two introduces the basic concepts needed to understand the physics in optical lattices. Starting from a non-interacting perspective, we derive the single-particle band-structure. Next, we present two experiments that can be understood within this context, namely the demonstration of free fermion antibunching for atoms released from an optical lattice, and the radio-frequency association of heteronuclear molecules near a Feshbach resonance. We then proceed to consider interactions and introduce the fundamental Bose-Fermi Hubbard model. The chapter ends with the introduction of self-consistent Wannier functions, and a simple model describing their consequences for the many-body system, the most important one being a significant renormalization of all Bose-Hubbard parameters. The third chapter presents experiments suitable to demonstrate and quantitatively evaluate the renormalization effects and changes in the filling statistics induced by Bose-Fermi interactions, making use of the Quantum phase diffusion induced by a sudden quench of the system Hamiltonian that freezes out the atom number distribution. The fourth chapter investigates the modification of the many-body physics in the presence of tunable Bose-Fermi interactions. After a short survey of the relevant theoretical predictions, we present experiments demonstrating the dominant role of renormalization of bosonic Hubbard parameters. The thesis ends with a short outlook on open questions and possible future directions of research.

One

Preparation of ultracold mixtures

This chapter describes the experimental apparatus constructed in the course of this work as well as the experimental methods relevant for the preparation, manipulation and detection of the quantum gas mixture. We focus here on aspects of particular relevance for the experiments presented in later chapters of this thesis. A first version of the laser-cooling setup has been described previously in [11].

1.1 Atom sources and laser cooling

Laser cooling constitutes the initial step in all experiments on degenerate quantum gases. This can conveniently be accomplished in a magneto-optical trap (MOT) [121, 106] which captures atoms from vapour [109]. In our case, both atomic species are trapped in a common MOT, which is loaded from dispenser sources[1]. This kind of dispenser-based common MOT setup has been demonstrated previously in [56]. The dispensers are heated at currents in the range of 5 to 7.5 A for several seconds. A Peltier element attached to the dispenser mount on the outside of the vacuum chamber, backed by a water cooling facility, assures fast cool-down as soon as the currents are switched of. Therefore, the dispensers essentially work as switched atomic beam sources with switch-on/off times of few seconds [129]. Figure 1.1 shows the dispenser sources in action. The cooling light for both Rubidium and Potassium atoms is provided by home-built tapered

---

[1] While Rb dispensers are commercially available, the low natural abundance of the fermionic Potassium isotope forbids the use of standard Potassium sources. Therefore, Potassium dispensers had to be home-built from isotope-enriched material. See [35, 129] for details.

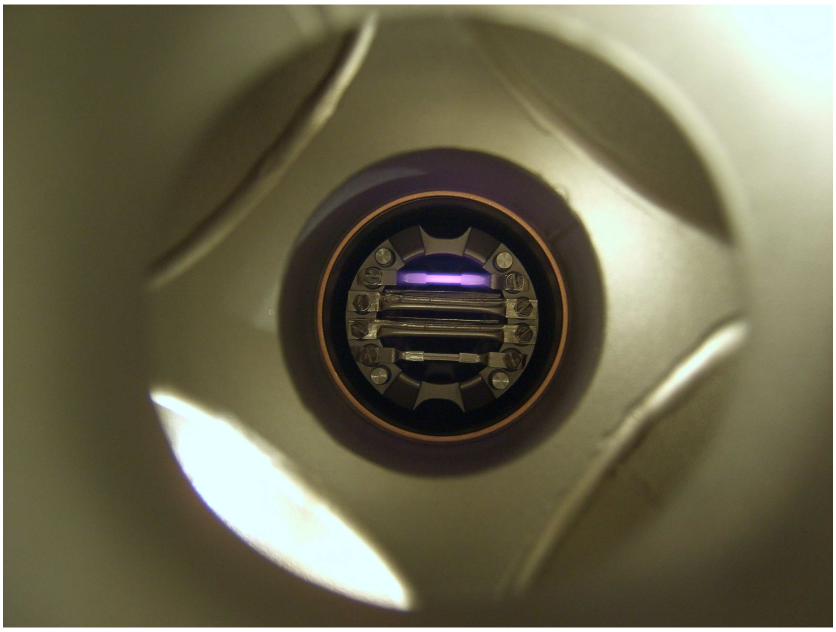

Figure 1.1: Dispenser atom sources for Potassium and Rubidium. Both the Potassium (inner) and Rubidium (outer) dispensers are provided redundantly. This picture shows the uppermost dispenser in operation, at a current slightly exceeding the normal operation current.

amplifier systems seeded by grating-stabilized diode lasers[2] in Littrow configuration [125]. Repumping light, which is needed to close the cooling cycle transition, is provided by a second diode laser, which seeds a second tapered amplifier in the case of Potassium, where large amounts of repumping light are mandatory due to the small excited state hyperfine splitting [25]. In the case of Rubidium, an injection-locked slave diode provides sufficient repumping power. A schematic of the laser system can be found in appendix C, for more details see reference [11].

The Rubidium cooling laser as well as both cooling and repumping laser for Potassium are frequency-offset locked to additional reference lasers, which in turn are stabilized using saturated-absorption frequency modulation spectroscopy [13, 65]. In the case of Rubidium, the $F = 2 \rightarrow F' = (3, 1)$ crossover is used for locking the reference laser. Light for optical pumping and imaging can then be derived straightforwardly from this laser using acousto-optic modulators for frequency shifting. In the case of ^{40}K, the sit-

---

2) diode types are Sharp GH0781 series for Rb and Eagleyard EYP–RWE-0770 series for Potassium

uation is slightly more complicated, as the low abundance of the fermionic isotope does not permit detection of the corresponding transitions in a standard vapor cell. Therefore, we reference our laser to the $F = (2, 1)$ groundstate crossover feature in the most abundant ^{39}K isotope. As this feature is more than 600 MHz away from either of the transitions of interest, an additional diode laser is used to provide optical pumping and imaging light. The locking scheme for this laser can be found in appendix C. The frequency offset locking relies on detection of a beat node with the respective reference laser on a fast photodiode[3]. The feedback signal is then derived either using an interferometric setup of Grimm type [139], or direct electronic frequency-to-voltage conversion of a prescaled[4] intermediate frequency representation of the beat node signal. These setups are capable of providing up to 1 GHz lock range. The detunings of all offset locks can be changed on the fly by computer control. It is therefore straightforward to use the existing setup for laser cooling of either isotope of Potassium simply by changing the detuning values, and magneto-optical trapping of both ^{39}K and ^{41}K has been demonstrated. The magneto-optical trap for ^{87}Rb can be loaded to saturation in less than five seconds, while the ^{40}K MOT takes longer to collect atoms. During the time when both MOTs are operated simultaneously, considerable losses of trapped Potassium atoms can be observed, which are probably due to light-assisted collisions. A similar behaviour has also been reported in reference [145]. We therefore start cooling the Potassium first and only add Rubidium cooling light after ten seconds, thus keeping the time window of simultaneous operation short. After three more seconds, the dispensers are switched off and the pressure starts dropping. We leave the cooling light on for two more seconds, the last 500 ms of which are dedicated to a bright MOT phase for the Potassium atoms in which the cooling laser is tuned very close to resonance. This phase presumably compresses the Potassium cloud [82] and yields an increase of approximately 50% in atom number that can be trapped in the magnetic trap. Afterwards, a short optical molasses further cools the Rubidium atoms. Figure 1.2 shows typical MOT loading fluorescence traces recorded with two photodiodes behind narrow spectral filters for the Rubidium and Potassium D2 wavelength, respectively. Subsequently, an offset magnetic field of approximately 1 G is applied, which serves to spin-polarize both species with a short light pulse on the σ^+ $F = 2 \rightarrow F' = 2$ and $F = \frac{9}{2} \rightarrow F' = \frac{9}{2}$ transitions, respectively.

---

[3] Type Hamamatsu G4176-03 on a Kuhne KU0180A broadband amplifier

[4] A prescaler is a fast digital circuit, which will provide at its output a low-to-high transition for every 2^n-th transition at the input. Prescalers exist as integrated circuit components and are widely used in telecommunication applications

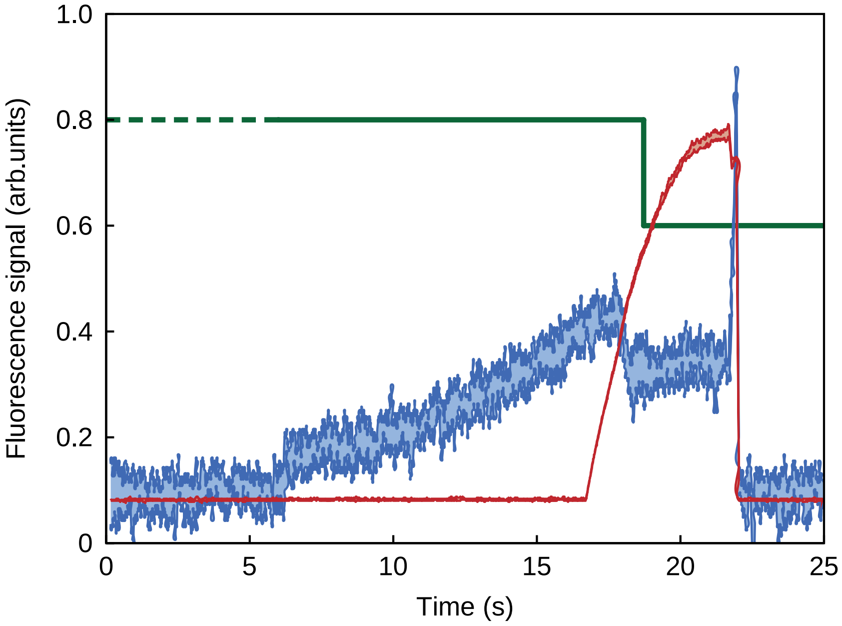

Figure 1.2: MOT fluorescence of Rubidium (red) and Potassium (blue) atoms. The traces show the full range of values observed in five subsequent experimental runs. The green curve denotes the dispenser preheating (with no laser light present), heating, and switch-off. The loss of ^{40}K atoms at the onset of the ^{87}Rb MOT phase is clearly visible. The large increase in Potassium fluorescence at the end of the MOT phase and the corresponding slight loss of Rubidium atoms is due to the reduced detuning in the bright MOT phase.

The number of atoms of both species that can be cooled and trapped in the two-species MOT is limited by interspecies loss processes, as can clearly be seen from figure 1.2. Presumably, such losses are due to light assisted collisions. It turns out that optimum performance of the two-species MOT is obtained if the two clouds are spatially separated on a millimeter scale by means of radiation imbalance along one cooling beam axis.

1.2 Magnetic trapping and transport

The spin-polarized mixture is captured in a magnetic quadrupole trap. To this end, the coils which provide the magnetic field for the MOT are instantaneously switched on again. In order to achieve a fast rise of the magnetic field, a pulsed current source is used, which mainly consists of a large capac-

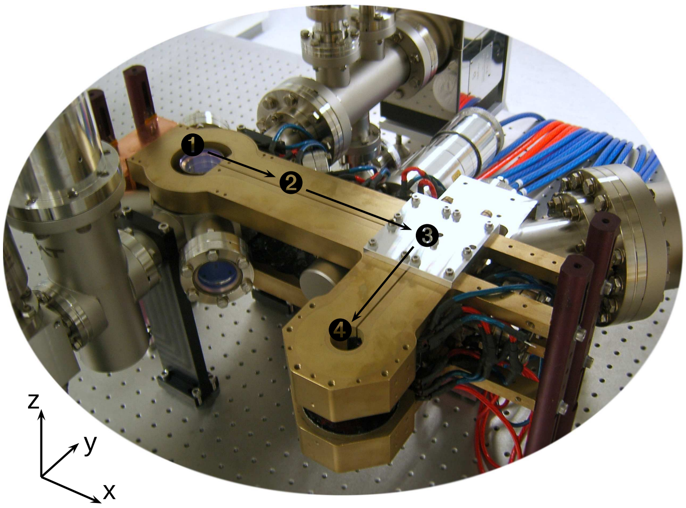

Figure 1.3: Experimental apparatus in the construction phase, without surrounding optics. The additional coils used for background field cancellation, Bias offset fields and Stern-Gerlach detection are not yet mounted. The magnetic transport of the atoms starts in the MOT region ❶, through a tube containing the differential pumping section ❷, bends around the corner ❸, to end up in a glass cell ❹. The coils needed for the transport and the subsequent magnetic trapping are mounted on the inside of the monolithic brass blocks above and below the vacuum chamber, which also contain a water cooling pipeline.

itor discharging into the coil through a small damping resistor upon closing of a FET switch[5]. In this case, the discharging of the capacitor during the rise time $\tau_\uparrow$ can essentially be neglected, and we have $\tau_\uparrow \approx \frac{L}{R}$, where L is the coil inductance and R the series resistance. While the capacitor is discharged on a longer time scale $\tau_\downarrow \approx RC$, a programmable power supply can gradually take over the current. By careful choice of the precharging value for the capacitor, and the capacitance and resistance values, a rise time $\tau_\uparrow < 300\,\mu$s, and thus a speed-up by more than two orders of magnitude, can be achieved. The gradient of the resulting magnetic trap is roughly 2×10^2 G/cm. The trapped atoms are then magnetically transported into an optical quality glass cell where evaporative cooling takes place. To this end, overlapping pairs of coils in quadrupole fiel configuration are placed along

---

[5] FET = Field effect transistor. Switching of currents is usually accomplished using Enhancement type MOSFET devices, such as STE180N10. In the following, these are always referred to as FETs

the transport path. By smoothly ramping the currents in neighbouring coil pairs, the trap center can be made to move with the atoms following adiabatically. The procedure is analogous to the one demonstrated first for cold Rubidium atoms [59]. In our case, the transport sequence involves 13 pairs of coils, driven by four programmable power supplies[6]. The whole transport procedure takes 2.5 seconds, until the atoms end up in the glass cell. No attempt has been made to calibrate the atom loss and heating caused by the transport systematically, since the atom clouds after transport are both too large and too dilute to be amenable to standard absorption imaging. However, from the fact that a slower transport is slightly less efficient, we conclude that this is currently not a limiting factor for the experiments. Figure 1.3 shows the setup during the construction phase, without any surrounding optics, where the transport system is clearly visible.

1.3 Trapping and evaporation of mixtures

At the end of the transport, the atoms are held in a magnetic quadrupole trap. Forced evaporative cooling is then carried out in a two-step procedure, which was developed in the course of this work. In a first step, radio-frequency forced evaporative cooling of the bosons takes place in an optically plugged magnetic quadrupole trap. The mixture is then transferred into a crossed optical dipole trap, where further evaporation leads to simultaneous quantum degeneracy of the two species.

Optically plugged quadrupole trap and evaporation therein

After transport, the atoms are trapped in a magnetic quadrupole trap, approximately 4 mm and 9 mm from the surfaces of an optical-quality glass cell. This kind of trap allows efficient forced evaporative cooling via radio-frequency induced spin-flips [32]. Unfortunately, magnetic quadrupole traps are not suitable for cooling into the quantum degenerate regime due to losses occuring near the zero crossing of the magnetic field due to Majorana spin flips [100]. Therefore, in previous experimental setups similar to the one presented in this work, the quadrupole trap was smoothly converted into a QUIC trap [43]. While this kind of trap is very robust and easy to use, it breaks the cylindrical symmetry of the original quadrupole trap and shifts

---

[6] Delta SM15-100

the trap center closer to the surface of the glass cell, approximately 5 mm away from the geometrical center.

The experiments described in this thesis require a very high degree of control over both travelling and standing light waves. This can not be achieved close to the surface of the glass cell in which the experiments take place, as parasitic reflections on the glass-vacuum interface will lead to additional interference patterns[7]. Therefore, it is desirable to trap the atoms in the center of the glass cell. Also, as we will see in section 1.5, in the context of interspecies Feshbach resonances, a natural way to produce the necessary high magnetic fields is by inverting the current in one coil of the quadrupole trap pair, thus essentially creating a Helmholtz field. Unfortunately, as soon as one goes away from the symmetry axis of the trap, a strong field gradient arises in the horizontal direction, making it hard or even impossible to hold atoms in a dipole trap. Again, these issues are solved as soon as the trapped atoms are located in the center of the glass cell, which is on the quadrupole symmetry axis. These considerations led to the development of a new trapping scheme for the Rubidium-Potassium mixture. To overcome the Majorana losses while avoiding the geometrical problems outlined above, an optically plugged quadrupole trap can be used. This trap design has been used in the early days of Bose-Einstein condensation [31], but was given up soon after for the limitations the plug beam imposed on experiments with the BEC. However, in the present setup, the plugged trap is only an intermediate cooling stage, thus these limitations do not apply here[8]. The optical plug is provided by $P = 600\,\mathrm{mW}$ of blue detuned light at a wavelength $\lambda = 760\,\mathrm{nm}$, focussed down to a Gaussian beam waist $w_0 = 15\,\mu\mathrm{m}$. The resulting effective potential is visualized in Figure 1.4. The plug beam points along the vertical symmetry axis of the quadrupole trap. After a coarse initial alignment, the presence of the plug results in substantially higher atom numbers and lower temperatures after some evaporation in the quadrupole trap. These quantities can then be used as a benchmark for further precision alignment. Figure 1.5 shows the outcome of such a procedure, demonstrating the need for alignment precision on a few-micron level, which in our case can be obtained through the use of a piezo-controlled mirror mount. The fact that the plug wavelength is closer to resonance for the Potassium atoms compensates for the a priori stronger

---

[7] The outer surface of the glass cell has a broadband anti-reflection coating, yet this coating is not suitable for the dipole trap wavelength. The inner surfaces are uncoated.

[8] To our knowledge, this is the first time that optical plugging has been used for a two-species mixture. The success of the method in the present setup has inspired several other laboratories to build up optically plugged traps for mixtures.

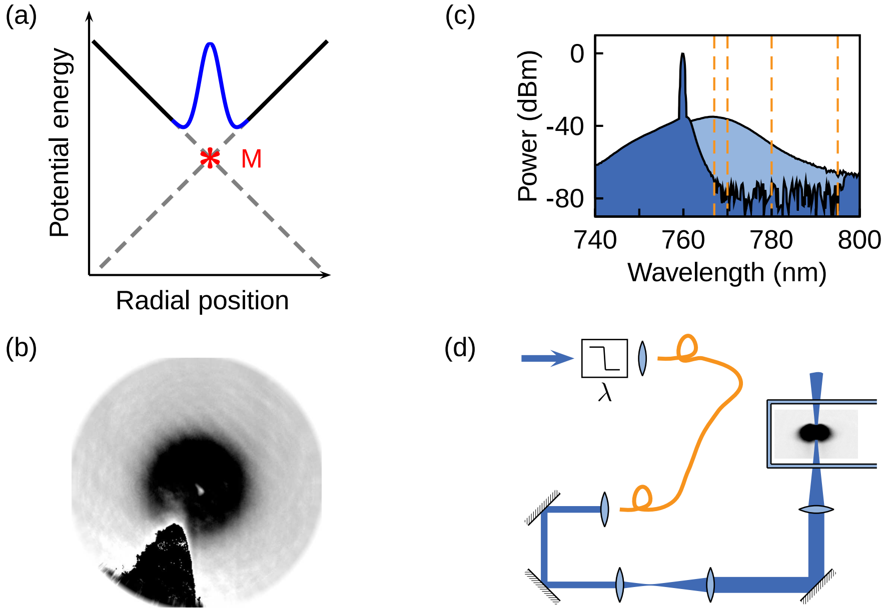

Figure 1.4: Optically plugged quadrupole trap. (a) Effective potential in the radial direction. The plug beam repulsive potential (blue) prevents spin flips from the trapping (black) to the antitrapping (dashed grey) Zeeman level at the position of the Majorana hole (M). (b) The geometry can be visualized using insitu imaging of a cloud of Rubidium atoms (top view). The depletion at the cloud center due to the presence of the optical plug is clearly visible. The dark feature in the lower-left part of the image is due to local saturation of the CCD camera by the light from the plug beam. The apparent off-center position of this saturation feature is due to a chromatic shift in the imaging system, which is important to take into account in the alignment procedure. (c) Spectrum of the tapered amplifier laser system providing the plug light, with and without filtering. The light-shaded area is cut away by the filter, yielding a suppression by up to 30 dB at the atomic D-line resonance wavelengths (dashed lines). (d) Schematic of the optical setup used for the plug beam. The optical fiber is necessary for spatial filtering of the TA mode profile. The final steering mirror is equipped with remotely controlled piezo actuators to allow precision alignment.

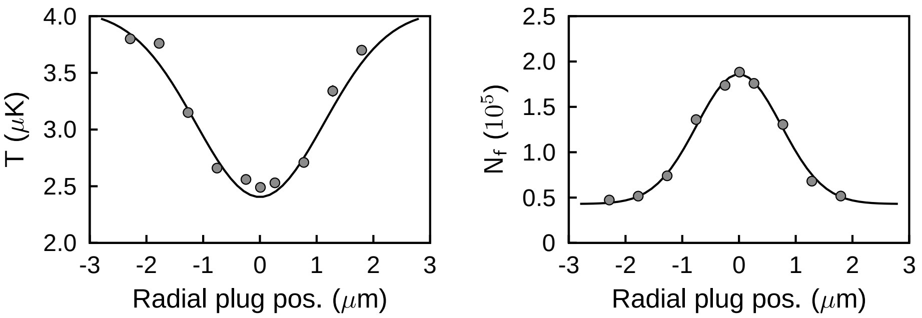

Figure 1.5: Precision alignment scan of the optical plug beam. Both the temperature (left-hand panel) and the atom number (right-hand panel) at the end of the evaporation sequence give a clear indication of the optimum lateral position of the plug. The lines are Gaussian fits to the data, with a FWHM of 1.1 and 0.7 μm respectively, significantly smaller than the plug beam waist.

Majorana losses of this lighter atom. We have measured the efficiency of the optical plug in terms of remaining atom numbers for both Potassium and Rubidium atoms. The results are shown in figure 1.6. Although a saturation effect is reached slightly earlier for Rubidium, both species are clearly saturated at optical powers of no more than 400 mW, a level which can be obtained from a standard tapered amplifier setup coupled through a polarization-maintaining single-mode optical fiber (see also figure 1.4 (d)). However, care must be taken in order to reduce the spectral background of the tapered amplifier, which reaches well into the region of the D-line resonances of our atoms. This task can be accomplished using an angle-tuned edge filter, as can be seen in figure 1.4 (c). The optical setup for the plug is described in more detail in [17]. After an initial compression of the trap to a gradient of about 3×10^2 G/cm, which increases the collision rate, we perform radio-frequency forced evaporative cooling down to approximately 2 μK in 9 seconds. It is essential to obtain high densities especially in the temperature regime around 100 μK to maintain interspecies thermalization in this regime, as the interspecies collisional cross-section was found to be suppressed by a Ramsauer-Townsend type resonance [122, 134, 6]. As the evaporation proceeds, we gradually decrease the magnetic field gradient by about 20%, until, at temperatures below 5 μK, the trap is decompressed rather quickly in approximately 0.2 s by a factor of 15 to 20 in order to prevent three-body collisions. At such low gradients, gravity leads to a substantial tilt of the potential around the minimum in the vertical axis. It has turned out that the parameters of this decompression procedure can

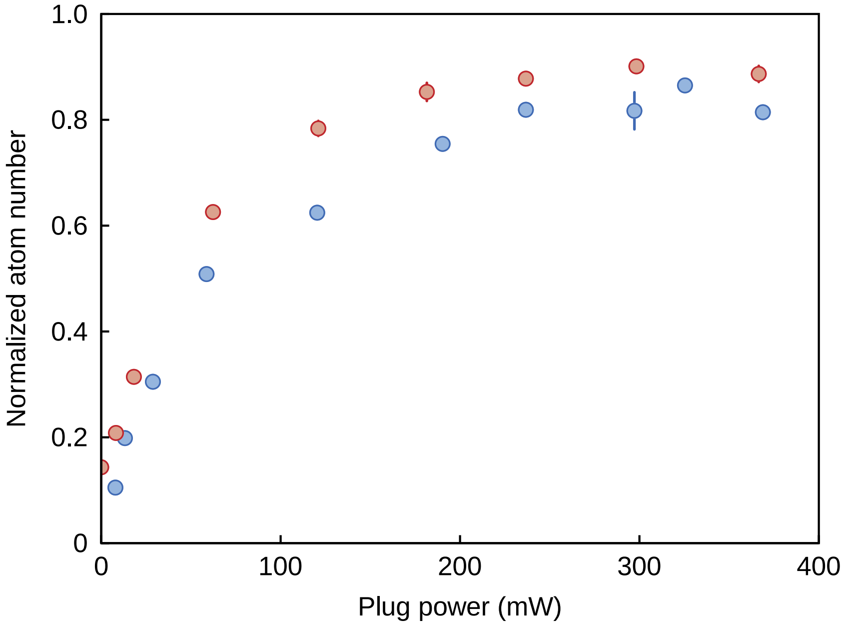

Figure 1.6: Efficiency of optical plug for two atomic species. The red and blue points correspond to Rubidium and Potassium atoms, respectively. With ample power requirements, saturation of the atom numbers of both species can be reached, indicating that the Majorana hole is fully plugged.

serve as a sensitive control knob in order to tune the ratio of Potassium and Rubidium atoms at constant final temperature.

The efficiency of radio-frequency forced evaporation in the optically plugged trap potentially suffers from a spatially varying coupling between the atomic spins and the oscillating magnetic field. For a transition to an untrapped Zeeman state to happen, it is necessary that the magnetic field vector be perpendicular to the quantization axis, i.e. the static trapping field. However, in a quadrupole type trap, there is no unique field direction, instead, atomic spins point radially outwards in a ring around the field minimum. Even more complicated, as atoms sag in the combined potential, they see an increasing vertical field component. The situation is sketched in figure 1.7. In the experiment, the RF field is created by a three-loop spiral antenna, the field vector being essentially parallel to the antenna axis, which is almost radial in the horizontal x-y-plane. As it turns out, the efficiency of the process vanishes gradually at very low temperatures. To understand this behaviour, it is important to note that the region where atoms are cut away by the RF knife is a circle in a plane below the trap center. As the evaporation progresses, the knife moves upwards, accompanied by a change

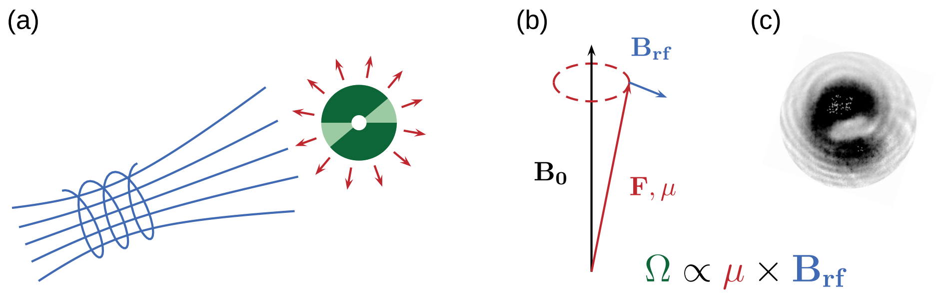

Figure 1.7: Coupling to the RF knife in the plugged quadrupole trap. (a) Sketch of the geometry of RF antenna, oscillating magnetic field (in blue), the atomic cloud (in green) and the local spatial orientation of the atomic spin (red arrows). Dark and light shaded regions indicate atoms experiencing good or poor coupling to the RF field, respectively. (b) Vectorial representation of the precondition for efficient RF coupling. For a transition to be allowed, a torque must be exerted on the atom's magnetic moment. (c) Absorption image of a cloud of Rubidium atoms at the end of the RF evaporation procedure, for a very low final RF frequency of 300 kHz. The regions of good and bad coupling from part (a) can be identified qualitatively. The slight asymmetry stems from the fact that in contrast to (a), the RF antenna is slightly tilted in the real system, and the atoms are therefore located off-axis.

in the static field direction. Towards the end of the evaporation procedure, the dominant field component is pointing radially outwards. In this situation, the coupling to the RF field varies between full strength and zero as one goes around the ring. At the same time, the symmetry of the trap hinders thermalization along the ring, as the trapping frequency vanishes along the ring. Therefore, thermal equilibrium is only reached locally in this situation. This effect leads to a dramatic apparent increase in temperature in the first few hundred milliseconds after the end of evaporation, due to the delayed thermalization. In fact, it is possible to observe this effect in absorption images taken from Rb clouds shortly after release from the trap, see figure 1.7 (b). From such images, it it can be seen, that for very low temperatures, thermal equilibrium takes hundreds of milliseconds to establish after the end of forced evaporation. In previous experiments with optically plugged quadrupole traps, this effect did not come into play as the circular symmetry was broken either by gravity [31] (the plug beam was transversal to the trap symmetry axis in this configuration) or by the use of an elliptical plug beam [111].

In order to avoid such complications as the thermalization issue and the fading away of the couling efficiency, we stop the RF evaporation procedure well above the critical temperature for Bose condensation, and transfer the precooled atoms into an optical dipole trap for the final evaporation step. This trap, the evaporation procedure therein, and the actual transfer procedure will be discussed in the following sections.

Optical dipole trap and evaporation to degeneracy

Optical dipole potentials

Optical trapping of atoms or molecules does not require for the particles to be in a low-field-seeking Zeeman state, thus providing more flexibility than magnetic trapping. Instead, the trapping effect relies on the optical dipole force. This force can be thought of as the interaction of the electric part of the light field with the electric dipole moment which it induces in the atom. Fundamentally, an off-resonant light field $\vec{\mathcal{E}}$ leads to an atomic dipole moment

$$\vec{d} = \alpha\,(\omega)\dot{\vec{\mathcal{E}}} \tag{1.1}$$

which can be described by the frequency-dependent polarizability $\alpha\,(\omega)$. The induced dipole moment has a potential energy in the light field of intensity $\mathcal{I}(\vec{r})$ given by [62]

$$\Delta E_{dip} = -\tfrac{1}{2\,\epsilon_0 c}\,\Re[\alpha\,(\omega)]\,\mathcal{I}(\vec{r}) \tag{1.2}$$

Therefore, it is possible to trap atoms or molecules inside a Gaussian beam profile, provided that $\Re[\,\alpha(\omega)] < 0$. This is the operating principle of the optical dipole trap[9].

For a quantitative understanding of dipole potentials, we need to know the atomic polarizability. For a two-level atom, the dipole moment induced by an electric field $\vec{\mathcal{E}}$ which harmonically oscillates at a frequency ω somewhere in the vicinity of an atomic resonance frequency ω_0 is given by [2]

$$\vec{d}(t) = \frac{e^2}{m}\,\frac{1}{\omega_0^2 - \omega^2 + i\omega\,\Gamma}\,\vec{\mathcal{E}}(t)\,, \tag{1.3}$$

where Γ denotes the natural damping of the oscillation due to decay of the excited state. Therefore, the real part of the atomic polarizibility can be

---

[9] It is worth mentioning that the same line of arguments holds for a macroscopic polarizability of non-atomic objects. The so-called optical tweezers [5] which can trap and manipulate objects such as polystyrol balls, viruses or even living cells, are by no means different from a dipole trap as described here.

expressed as

$$\Re[\alpha\,(\omega)] = \frac{e}{m}\,\frac{\omega_0^2 - \omega^2}{(\omega_0^2 - \omega^2)^2 + \omega^2\,\Gamma^2}\;. \tag{1.4}$$

The most relevant situation in practice is the case of large detuning, characterized by the hierarchy

$$\Gamma \ll \delta \ll \omega, \omega_0, \tag{1.5}$$

where $\delta = \omega - \omega_0$ is the detuning from resonance. In this case, we may assume that $\omega \approx \omega_0$, and $\omega_0^2 - \omega^2 \approx -2\,\omega_0\,\delta$. With these approximations, we can simplify our result to read

$$\Re[\,\alpha\,(\omega)] \propto -\frac{1}{\delta}. \tag{1.6}$$

The energy of the atom is thus upshifted in the presence of blue-detuned light ($\delta > 0$) and lowered in a red-detuned light field ($\delta < 0$). Therefore, red-detuned laser beams can be used for dipole-trapping of effective two-level atoms. If several excited states need to be considered, their individual contributions can be summed up to give the total energy shift. In the case of alkali atoms, the dominant contribution to the polarizability is related to the D-line doublet. The resulting ground state energy shift in the case of linearly polarized light becomes [62]

$$\Delta E = \tfrac{1}{3}\,(\Delta E_{D1} + 2\,\Delta E_{D2})\,. \tag{1.7}$$

A crossed dipole trap

The optical dipole trap used in the experiments described in this thesis is formed by the intersection of two laser beams crossing under an angle of almost 90° in the horizontal plane. The light is derived from a single Yb:YAG laser[10] operating at a wavelength of $\lambda = 1030\,\mathrm{nm}$, yielding almost identical AC Stark shifts for both species. The main design criterion in the context of this thesis was to make the dipole trapping potential as flat as possible in order not to introduce inhomogenieties. Essentially, this can be achieved by chosing large beam waists for the trapping beams. However, the trap can not be made arbitrarily flat in the vertical axis, as it still needs to hold atoms against gravity. Therefore, the trap is formed by elliptical beams with an aspect ratio of almost four to one. The dipole beams have

---

[10] ELS Versadisc 18W

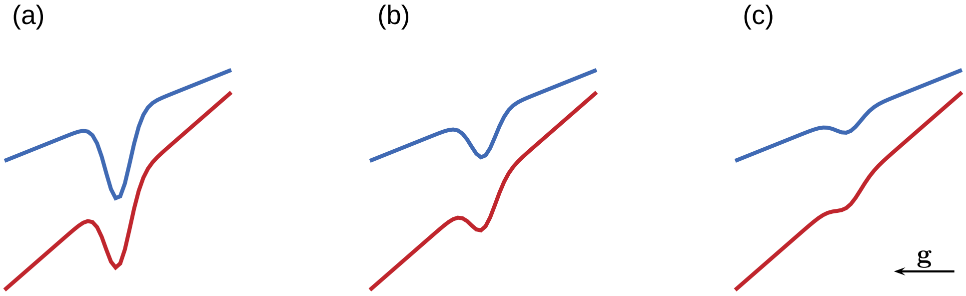

Figure 1.8: Effective potentials of the crossed dipole trap in the vertical direction in the presence of gravity for both Rubidium and Potassium, (a) for maximum compression, (b) for intermediate compression still above the Rubidium trap bottom, and (c) for very weak compression, in between the trap bottoms of the two species. The mass ratio of the two species provides a straightforward mechanism for species-selective evaporation.

orthogonal polarization and are frequency offset with respect to each other by 20 MHz using acousto-optic modulators (AOMs). This prevents Raman transitions between the two beams. The beam waists are $w_h = 150\,\mu$m and $w_v = 45\,\mu$m in the horizontal and vertical direction, respectively, leading to a minimum Rayleigh length

$$z_R = \frac{\pi w_0^2}{\lambda} \tag{1.8}$$

on the order of 6 mm, which allows to neglect the longitudinal contributions for all practical purposes. The resulting potential in the case of a symmetric trap (equal confinement in x and y directions) thus essentially takes the form

$$V_{\mathrm{dip}} = -V_0 \left(e^{-2\,x^2/w_h^2} + e^{-2\,y^2/w_h^2} \right) \cdot e^{-2\,z^2/w_v^2} + m\,g\,z. \tag{1.9}$$

This effective potential is visualized in figure 1.8. Figure 1.9 shows the resulting trap depths and harmonic trap frequencies for both the horizontal and vertical axes and both species. It should be pointed out that while the crossed structure can easily be visualized with thermal clouds on the order of $10\,\mu$K (see Figure 1.10), the trap can be considered perfectly ellipsoidally symmetric in the ultracold regime. This can be seen from the harmonic approximation

$$V_{dip} \approx 2\,V_0 \left(\frac{x^2 + y^2}{w_h^2} + \frac{(z - z_0)^2}{\chi(z_0)\,\omega_v^2} \right), \tag{1.10}$$

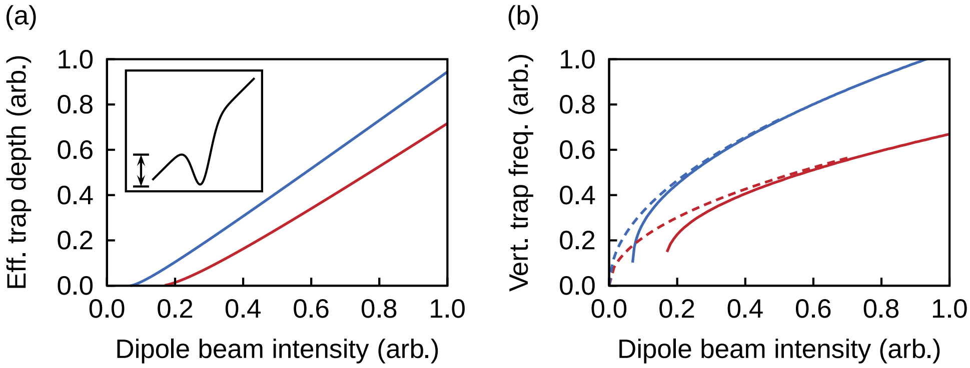

Figure 1.9: Parameters of the crossed dipole trap. (a) Effective trap depth in the presence of gravitational sag for Rubidium (red curve) and Potassium atoms (blue curve). The inset shows the definition of the trap depth in turn of the barrier height in the vertical direction. For intensities above approximately twice the respective trap bottom value, the depth linearly increases with intensity. (b) Effective trap frequency in the vertical direction for Rubidium (solid red curve) and Potassium atoms (solid blue curve). The dashed lines show the harmonic approximation in the absence of gravity.

where $-\frac{1}{2}w_v < z_0 < 0$ is the equilibrium position in the presence of gravitational sag[11], and $\chi(z_0) < 1$ parametrizes the local minimum in the vertical direction, the trap frequency of which is always reduced as compared to the sag-free case.

Evaporation in the dipole trap

Evaporative cooling in the dipole trap is achieved by symmetrically ramping down both dipole beams, thus reducing the effective trap depth. The rampdown is exponential and takes 4 s. As can be seen from figure 1.8, the trap is always deeper for Potassium as compared to Rubidium due to the higher mass, thus this process selectively only expels Rubidium from the trap. However, significant amounts of Potassium are lost due to inelastic interspecies collisions upon the density increase associated with the formation of a BEC.

Using the evaporation procedure outlined above, we regularly achieve BEC of up to 4×10^5 Rb atoms in the $|F = 1, m_F = 1\rangle$ state coexisting with

---

[11] The Gaussian potential features a maximum restoring force at half the waist away from the center, where the function changes curvature. For larger excursions from the center, the restoring force gradually drops to zero, and no equilibrium exists for a constant external driving force, such as gravity.

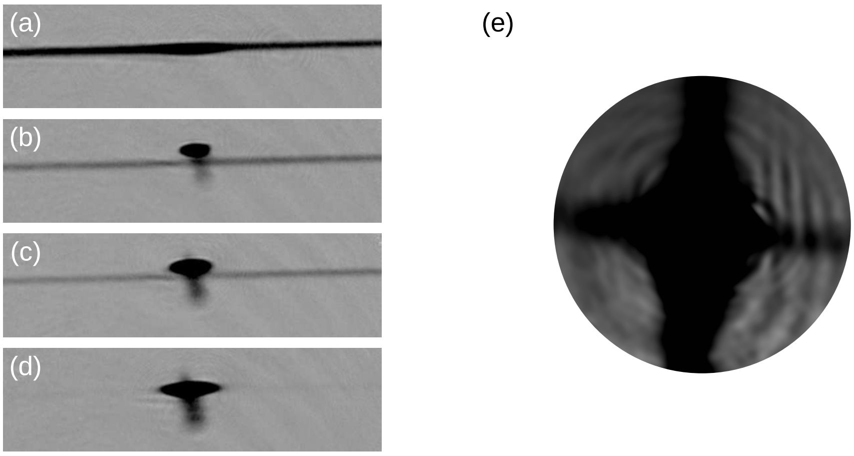

Figure 1.10: Visualization of the dipole trap isopotential surfaces with thermal atoms. (a)-(d) horizontal view along one dipole beam. Starting from a single-beam dipole trap (a), the relative alignment of the beams is improved (b) to (d) resulting in a final aspect ratio of approximately 1 : 4. During this process, less and less atoms escape along the beam axes, where the confinement is weakest. (e) vertical view, revealing the cross structure. The asymmetry in the image reveals a slight intensity imbalance between the two dipole beams. The picture has been subjected to a 5 px Gaussian blur, in order to suppress imaging artifacts. Note that once the temperatures are low enough, the atoms sample only a very small region of the trap, which then appears perfectly round.

a degenerate Fermi gas of up to 3×10^5 K atoms in the $|F = 9/2, m_F = -9/2\rangle$ state at $T \approx 0.2\,T_F$, where T_F is the Fermi temperature in the system. Lower temperatures down to $T \approx 0.15\,T_F$ can be obtained at lower fermion-to-boson ratios.

After reaching degeneracy with the two-species mixture, it is possible to recompress the trap by increasing the trapping beam intensities. It should be noted that this rampup also decreases the sag of the clouds and improves their spatial overlap. Figure 1.11 shows the gravitational sag for both species as a function of the dipole trap depth. From this measurement, the existence of a regime of good spatial overlap is clear, as well as the significant difference in the trap bottom for the two species, which allows the controlled removal of all bosons for experiments on pure Fermi gases [131, 138, 64, 137]. Furthermore, we can make use of the gravitational sag in order to calibrate the harmonic trapping frequencies of our dipole trap. To this end, the trap is strongly compressed adiabatically, such that the atom's

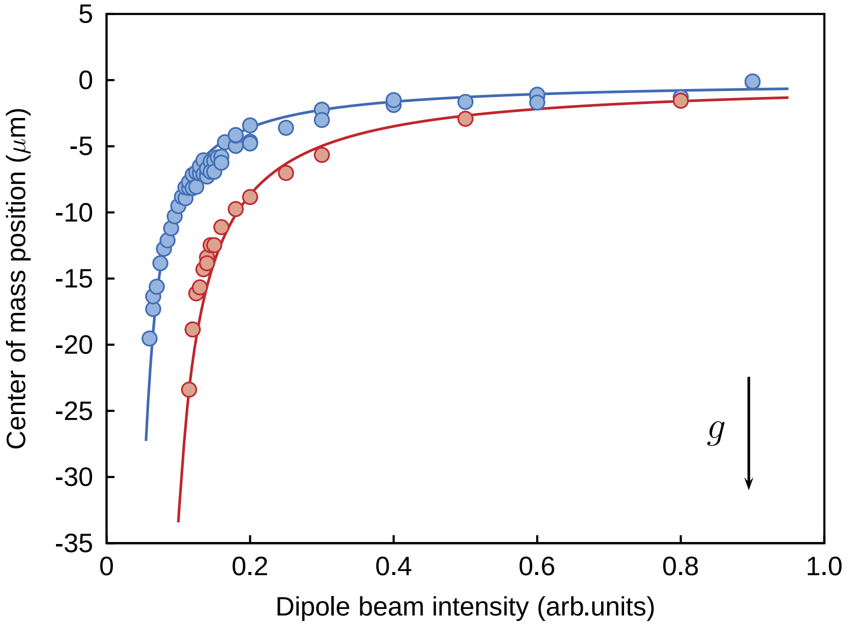

Figure 1.11: Gravitational sag for the two species for various depths of the dipole trap. The solid lines are calculated using a harmonic approximation above the respective trap bottom, with a global intensity scaling factor as the only free parameter. The relative vertical position of the experimental curves has been corrected for chromatic aberrations of the imaging system.

center of mass moves upwards. If the intensity is then suddenly lowered, the atoms fall back towards the center and a vertical center of mass oscillation sets in. As the plane defined by the dipole beams slightly deviates from the horizontal by about two degrees, such an oscillation can also couple to the transverse degrees of freedom, such that all trap frequencies can in principle be measured by this single excitation.

Rampover procedure from quadrupole to dipole trap

In the process of transfering the atoms from the plugged quadrupole trap to the crossed optical dipole trap, the most important issue is to preserve the spin polarization of the atomic sample. This is complicated by the fact that in the quadrupole trap, there exists no globally defined quantization axis. Instead, the orientation of the atomic spins is prescribed by the local magnetic field, pointing along the radial direction in the horizontal plane, but displaying also a finite axial component away from this plane. At the end of the transfer procedure, however, we want to have a well-defined quantization axis throughout the whole sample.

Maintaining spin polarization

The basic idea to perform the required breaking of the symmetry in a way which will preserve the spin polarization of the atoms is guided by the observation that the magnetic field configuration created by the quadrupole coils does provide a rather well-defined field orientation, in the region around the vertical axis, sufficiently far away from the magnetic field minimum which provides the actual trap. We will therefore try to pull the magnetic field zero out of the sample along the vertical axis, in a controlled way, leaving the atoms in this region of well-defined field orientation. To this end, we ramp on the crossed dipole trap to a high intensity. Thereby, we pin the atomic position to the center of the coil geometry[12]. Subsequently, part of the current which creates the quadrupole field is made to bypass the upper coil through a variable shunt[13]. Thereby, the magnetic field minimum (and thus the Majorana hole) moves upwards. At the same time, the strong vertical confinement of the crossed dipole trap prevents the atoms from following. Thus, by choosing suitable shunt currents, we can make sure that the zero of the magnetic field is located well above the trapping volume. Therefore, the magnetic field is now pointing in the vertical direction at the position of the cloud. To maintain the spin polarization upon switchoff of the magnetic trap, an additional offset field is applied in the horizontal direction. This has to be done adiabatically with respect to the local Larmor frequencies. The additional offset field is created by a pair of helper coils with the trapped atoms in the symmetry center, therefore, no additional gradients are introduced by this field at the position of the atoms. The magnetic field minimum however will be pulled further upwards along the offset field axis. This makes sure that the minimum does not cross the cloud position at the moment the quadrupole trap is switched off. This is especially important as we cannot exclude eddy currents in the first few hundred microseconds of the switchoff process, which might cause the actual field minimum to wiggle around in a rather uncontrolled way. The currents in the quadrupole coils are then quickly ramped to zero, and subsequently switched off alltogether. At the same time, the role of the

---

12) In fact, it has turned out to be favorable to align the dipole trap a few micron below this position, which might be due to the role of gravity.

13) This shunt consists of a FET with a linearizing analogue driving circuit in series with a small resistor. Typically, we sent less then 2 A through this shunt, so heat dissipation is not a serious issue.

offset field to define the quantization axis is taken over adiabatically by an additional pair of coils with their symmetry axis along the horizontal x-axis. This step is needed for technical reasons only, as the helper offset coils in the preceeding step consist of ordinary wire and lack any cooling, mainly due to space constraints. They would therefore overheat and eventually burn through within few seconds. The second pair of coils taking over the job is water-cooled and can stand the necessary currents indefinitely. The adiabaticity of this rotation of the quantization axis is trivially fulfilled in a simple make-before-break switch-on/off configuration, as the current rise timescale dictated by the coil inductance is slow compared to the sub-microsecond Larmor period. As a final step, the plug is switched off instantaneously[14], and the dipole trap evaporation procedure described in the previous section starts immediately afterwards. The whole procedure is illustrated in figure 1.12.

1.4 State preparation and analysis

An important point to keep in mind in the preparation of a two-component mixture is stability with respect to relaxation of the internal states of the atoms. Whether or not a particular mixture of hyperfine states is stable depends on multiple factors. Relaxation mechanisms which have to be taken into account are hyperfine relaxation, dipolar relaxation or spin exchange. These mechanisms provide ways for energy stored in the internal states of the atoms to be transferred into the external degrees of freedom. Typically, the energy released in this process is large enough to lead to particle loss from the trap. It is therefore necessary to work with a combination of states in which these processes are suppressed. This suppression is provided by approximately or perfectly conserved quantities. These can be

- **Total angular momentum.** Although the spin angular momentum of each individual atom is usually not a good quantum number in an interatomic collision event, the total angular momentum of the pair and it's projection are always conserved. The same holds to a good approximation for the total spin angular momentum of the pair, as the release of orbital angular momentum from an incoming s-wave is suppressed due to the near-perfect spherical symmetry of

---

[14] Adiabatic rampdown, which intuitively seems more favorable, was experimentally found to result in lower atom numbers and higher temperatures in the transferred sample. This might be due to spontaneous scattering of photons, which counter-intuitively may increase for a weaker plug.

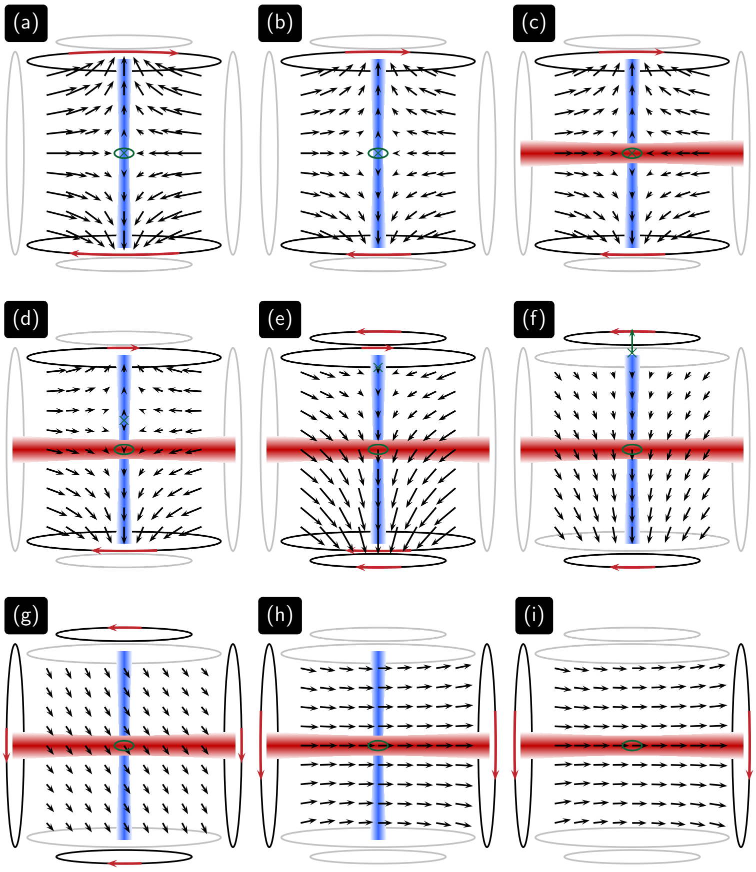

Figure 1.12: Illustration of the ramp-over from the plugged quadrupole trap to the optical dipole trap, in the x-z plane, with a schematic (not to scale) representation of the magnetic field (black arrows), the currents in the quadrupole, helper, and polarization offset coils, the laser beams for the optical plug (blue) and the x-axis dipole trap (red). The overall potential minimum always remains within the central green ellipse. The magnetic field minimum (if any) is indicated by the green cross. (a) Tightly compressed quadrupole magnetic trap for RF evaporation. (b) Decompressed quadrupole trap. (c) Dipole trap beams are ramped up. (d) The upper quadrupole coil is partially shunted, and the magnetic field minimum is vertically pulled out of the cloud, which remains pinned by the dipole trap. (e) A vertical offset field is applied to maintain spin polarization. (f) Quadrupole coils are switched off, the magnetic field minimum disappears along the vertical axis. (g)-(h) Horizontal offset field is gradually ramped up, adiabatically rotating the quantization axis into the horizontal x direction. (i) The plug beam is switched off, transfer is complete.

the system[15]. In our case, a *safe haven* would be the fully stretched state $|F = 2, m_F = +2\rangle \otimes |F = \frac{9}{2}, m_F = +\frac{9}{2}\rangle$, which are used in the magnetic trap, or the opposite state $|F = 2, m_F = -2\rangle \otimes |F = \frac{9}{2}, m_F = -\frac{9}{2}\rangle$, which is of limited use as it is hard to prepare from the magnetically trappable states without transient occupation of instable state combinations.

- **Energy.** Alternatively, it is possible to construct a *safe haven* from the conservation of energy. To this end, it has to be made sure that either the state combination of interest is the absolute ground state of the system[16], namely the combination of the lowest two Zeeman states $|F = 1, m_F = +1\rangle \otimes |F = \frac{9}{2}, m_F = -\frac{9}{2}\rangle$. This combination of states is used for most of the experiments described in this work, as it has the additional benefit of featuring a practically usable interspecies Feshbach resonance, see section 1.5. However, one also finds good stability of the mixture in any combination of states where ^{87}Rb is in it's lowest Zeeman state, while ^{40}K is in any state of the $F = \frac{9}{2}$ hyperfine manifold. This is due to the fact that both species have different Landé factors, which makes the Zeeman splitting between the m_F states of the bosons larger than the corresponding splitting for the fermions by a factor of approximately two at any (reasonably small) magnetic field. This means that in any possible spin exchange process, the amount of Zeeman energy released by the fermion would be much smaller than what the boson needs to pick up, and the kinetic energies in the sample are insufficient to provide for the missing energy. These state combinations are used transiently in the state preparation procedure, and one of them, namely the $|F = 1, m_F = +1\rangle + |F = 9/2, m_F = -7/2\rangle$, which is the second-lowest in terms of Zeeman energy, is used in the interaction switching procedure described in section 1.6.

Figure 1.13 shows the lifetime for various combinations of hyperfine states at a magnetic bias field of 13.4 G. The efficiency of the protection via

---

[15] Non-spherically symmetric interactions, such as direct magnetic coupling between the spins, can safely be neglected. However, it is interesting to note that in a deep optical lattice, the contribution of higher order partial waves to the scattering event can not be neglected a priori, as both rotational symmetry is broken and kinetic energies are high enough for penetration of angular momentum barriers.

[16] Clearly, the absolute ground state for two atoms would be the rovibrational ground state of a singlet molecule. However, we do not deal with deeply bound molecules in this work, they are nothing but a loss channel to the *metastable* absolute Zeeman ground state $|F = 1, m_F = +1\rangle \otimes |F = \frac{9}{2}, m_F = -\frac{9}{2}\rangle$.

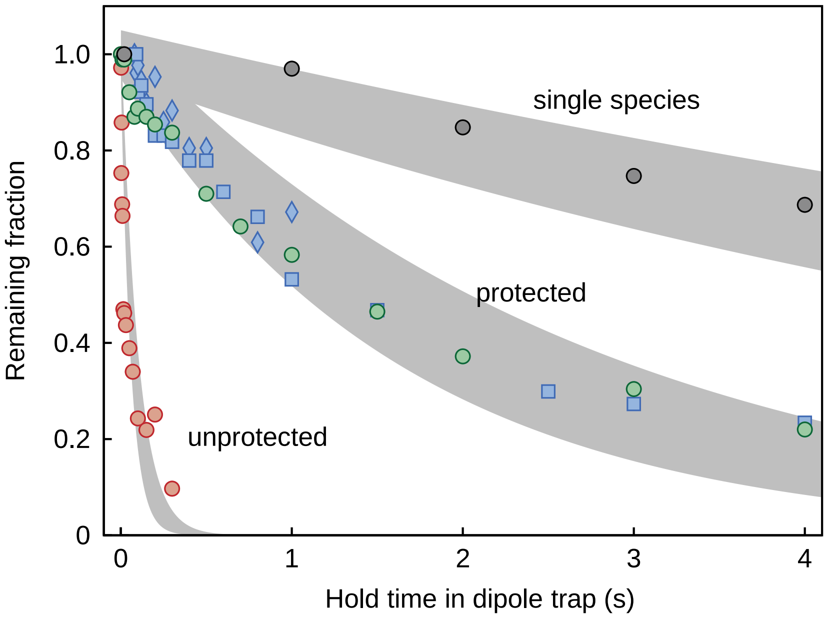

Figure 1.13: Comparison of stability for various combinations of hyperfine states. The shaded areas correspond to purely exponential decay, with lifetimes of $10, 2.2$, and $0.08\,\mathrm{s}$ respectively, assuming 5% shot-to-shot atom number fluctuations and a lifetime uncertainty of 25%.

conserved quantities is easily seen, as compared to the disastrous behaviour of the *worst case* scenario of preparing Potassium in its absolute ground state, while leaving Rubidium in the $|F = 2, m_F = +2\rangle$ initial state, giving rise to hyperfine relaxation. Within the experimental uncertainties, the lifetimes for all *protected* state combinations can be considered the same. Therefore, for all experiments presented in the remainder of this work, we transfer both atomic species into their respective Zeeman ground state. This state preparation procedure can in principle take place at any time during the evaporation ramp, still, we found it advantageous to prepare the Rubidium ground state right after transfer from the quadrupole trap[17]. The transfer of the Potassium is delayed for $3.5\,\mathrm{s}$ to minimize interspecies losses[18].

---

[17] Condensation of Rubidium works best in the $F = 1$ manifold already in the absence of Potassium.

[18] Strictly speaking, the above arguments only hold at very low temperatures. For hotter samples, the energy-conservation approach to suppression of bad collisions works less well, giving rise to more losses.

Preparation of Rubidium in the ground state

First, Rubidium is transferred to the $F = 1$, $m_F = +1$ state by means of microwave rapid adiabatic passage (RAP). Using a 250 kHz wide, 10 ms linear frequency sweep, we achieve transfer efficiencies better than 0.97. To prevent the remaining $F = 2$ atoms from fatal collisions with the $F = 1$ atoms, we apply a few millisecond resonant light cleaning pulse on the $5S_{1/2}\, F = 2 \rightarrow 5P_{3/2}\, F' = 3$ σ^+ transition. We have not observed any $F = 2$ atoms after application of this cleaning pulse, which leaves the $F = 1$ atoms unaffected.

Preparation of Potassium in the ground state

The absolute ground state of ^{40}K atoms in the presence of a magnetic field is the $|F = \frac{9}{2},\, m_F = -\frac{9}{2}\rangle$ state. This state features a practically useful interspecies Feshbach resonance with the ^{87}Rb $|F = 1,\, m_F = +1\rangle$ state at 547 Gauss [117, 86]. Therefore, we transfer the Potassium atoms all the way from $m_F = +\frac{9}{2}$ to $m_F = -\frac{9}{2}$ by radio frequency adiabatic passage in a single 60 ms long, 400 kHz wide downward sweep. Within our detection limits, this process has unit efficiency[19], also, it can be stopped at any point in between to prepare moderately pure samples of any of the ten $F = \frac{9}{2}$ Zeeman components. If preparation of other Zeeman states is required with higher fidelity, this can be achieved using RF RAP at a higher magnetic offset field, where the quadratic Zeeman shift allows for better state-selectivity, or using Raman hyperfine transfer to be discussed in section 1.6.

Detection of internal states

Spin state analysis can be achieved in a Stern-Gerlach type experiment [55, 144]. After switchoff of the trap, the free-falling atomic cloud is subjected to a pulsed magnetic gradient field for a few milliseconds. The atoms experience a force, depending on the strength of the field gradient and the magnetic moment of their internal states. The predominant field gradient is oriented orthogonally both to the vertical falling direction of the atoms and the offset magnetic field providing the quantization axis. The atoms will

---

19) A fraction of $\approx 5\%$ of the Potassium atoms initially in the $m_F = +\frac{7}{2}$ state ends up in the $m_F = -\frac{7}{2}$ state at the end of the RAP. These atoms can in principle be removed from the trap using a combination of microwave excitation to the $F = \frac{f}{2}$ hyperfine state, and subsequent optical push-out. In the context of this work, we have not used such a procedure in order to avoid associated heating processes.

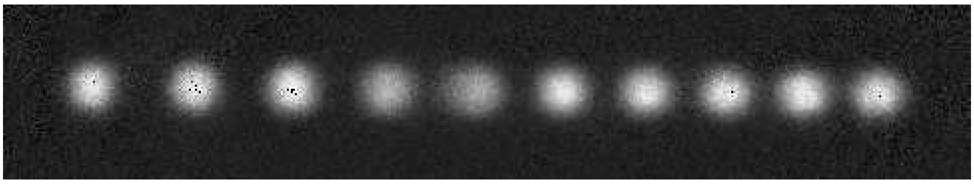

Figure 1.14: All Zeeman components of ^{40}K atoms revealed in a Stern-Gerlach experiment during time of flight.

thus aquire a transversal velocity component depending on their magnetic moment. Thereby, the internal state of the atom is encoded in the position of the atomic cloud after time of flight, which can then be evaluated using absorption imaging (see section 1.7). A sample picture showing all Zeeman components of the $F = \frac{9}{2}$ groundstate hyperfine manifold of ^{40}K atoms can be seen in figure 1.14.

For Rubidium, the usual imaging procedure only detects atoms in the $F = 2$ hyperfine manifold. However, most experiments presented in this thesis are carried out using Rubidium atoms in the lower $F = 1$ manifold. In order to detect these atoms, they are optically repumped to the $F = 2$ manifold by a short light pulse at the end of time of flight expansion. This repumping pulse can easily be combined with the aforementioned Stern-Gerlach technique. Moreover, it is possible to take two subsequent pictures of the same Rubidium cloud with a repumping pulse in between the pictures, thus selectively detecting the population of one hyperfine manifold on either picture[20].

1.5 Ultracold collisions, and tuning via Feshbach resonances

Ultracold collisions

The predominant interactions between neutral ground state atoms are elastic two-body collisions. While in principle, the physics of scattering processes from interatomic Born-Oppenheimer potentials is quite complex, there are some particularities of ultracold collisions, which in effect will allow us to ignore many of the details, and come to a very simple effec-

---

[20] The atoms that were detected in the first picture are usually no longer present when the second picture is taken, unless the time between images is very short, because of the recoil momentum the atoms aquire by scattering photons from the imaging beam.

tive description of interactions. Specifically, the following points need to be taken into account:

- Typical particle densities are on the order of $10^{13}\,\mathrm{cm}^{-3}$ for a standard BEC, and $10^{15}\,\mathrm{cm}^{-3}$ on a single site of an optical lattice. Usually, the mean interparticle distance is larger than the typical scale of the interaction potential by at least one order of magnitude. It is therefore reasonable to assume that two-body collisions are the dominant process, while three-body collisions are significantly less frequent.

- Once the temperature is low enough, the kinetic energy at the beginning of the collisions can safely be neglected, that is, the collisions happen right at the threshold of the respective scattering channel.

- As hardly any kinetic energy can be redistributed in the collision, elastic collisions dominate, unless a change of scattering channel is resonant, i.e. the difference in total energy between the two channels is smaller than the very small kinetic energy spread in the sample. Otherwise, inelastic processes only happen in three-body collisions, where they are almost always accompanied by trap loss of one or more of the atoms involved[21].

- The interaction potentials in question are spherically symmetric[22]. Therefore, total angular momentum is conserved, and it is useful to treat the scattering process in a partial-wave expansion [27]. Due to the lack of kinetic energy, high partial waves do not contribute to the outcome of the collision process, as the corresponding rotational barrier effectively hinders the incoming wave from entering the central region where it could be affected by the interaction potential. Thus, only the lowest partial waves contribute, and in the ultracold limit, we only need to consider *s-wave* contributions.

- Quantum statistics needs to be taken into account properly. If a collison is to happen between indistinguishable particles, then the total wavefunction needs to be symmetric (antisymmetric) with respect to

---

[21] The molecular energies released in such processes in the form of kinetic energy are almost always orders of magnitude larger than the trap depth.

[22] Strictly speaking, there is a very weak anisotropy both due to direct magnetic dipole-dipole coupling and molecular hyperfine structure. These effects are too small to be of any importance in the present context. See e.g. [91] for the observation of such effects and [57] concerning their possible consequences in optical lattice systems.

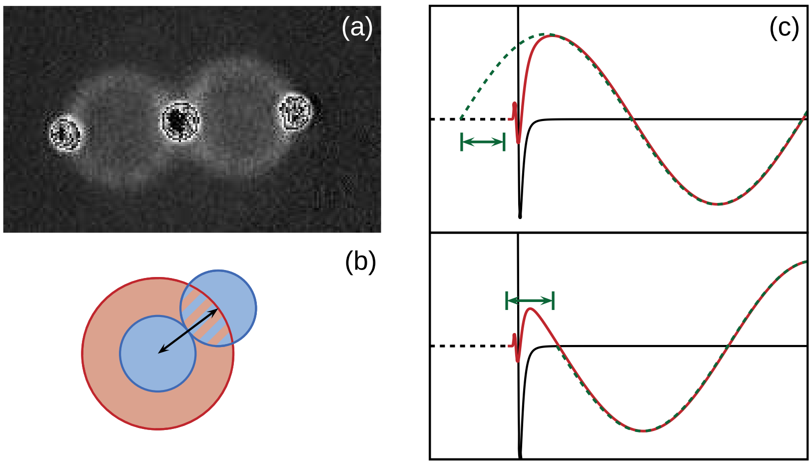

Figure 1.15: Ultracold short-range s-wave collisions. (a) The occurence of *scattering spheres* in the collision of two momentum components of a Bose-Einstein condensate mapped to real space in time of flight expansion demonstrates the predominant s-wave character of ultracold collisions (See main text for details). (b) The s-wave scattering length can be interpreted as an effective radius of hard spheres possessing the same total scattering cross section. (c) Interpretation of the scattering length in terms of the asymptotic phase shift. The real scattering wavefunction (red curve) for the short-range Born-Oppenheimer potential (black curve) looks like a phase-shifted free wave (dashed green curve) at large internuclear distances. The s-wave scattering length can be understood as the extrapolated innermost node of the phase-shifted wave (indicated by green arrows), which can be either negative (upper panel), corresponding to effective attractive interactions, or repulsive (lower panel, where the potential depth has been increased slightly in order to accomodate a bound state), yielding an effective repulsive interaction, albeit from a binding molecular potential curve.

> particle exchange for bosons or fermions, respectively. More specifically, bosons in the same hyperfine state can only collide in even partial waves, while fermions are restricted to odd partial waves, and thus do not collide at all in the zero-kinetic-energy limit.

From the considerations above, we know that we need to take into account elastic s-wave collisions between two bosons, or between one boson and one fermion. In either case, the outcome of the collision can be described by a single parameter, the collisional phase shift ϕ_0 aquired by the outgoing s-wave, or more conveniently and more commonly, the corresponding s-wave scattering length a, defined in the zero kinetic energy limit by

$$\tfrac{1}{a} = -\lim_{k \to 0} \cot \phi_0, \tag{1.11}$$

where k is the modulus of the incoming wavevector. The physical meaning of the s-wave scattering length a is illustrated in figure 1.15 (c). The collisional cross section is given by

$$\sigma = 4\,\pi\,a^2, \tag{1.12}$$

which gives rise to a nice intuitive notion of the scattering length: We can think of it as the radius of a hard sphere for which the collisional cross section would be the same, i.e. the simplest classical analogon to the range of the interaction potential, see figure 1.15 (b). The s-wave character of interactions can be demonstrated in a simple, yet beautiful collisional experiment. Starting from a BEC at momentum zero, we transfer some fraction of the atoms to momentum $\pm 2\,\hbar\,k$ by means of Bragg diffraction from a pulsed standing wave. After this pulse, the various momentum components propagate freely and separate during some time of flight. However, due to the high initial density, some collisions take place in the center of mass frames moving with velocities $\pm \frac{\hbar\,k}{m}$. Due to the elastic s-wave character of these processes, the relative momenta of the outgoing atoms are distributed isotropically on spheres of radius $\hbar\,k$ respectively. After time of flight, this momentum distribution is converted into a spherical density distribution, as can be observed in figure 1.15 (a).

The Fano-Feshbach resonance mechanism

One of the most striking assets in experiments with ultracold quantum gases is the ability to tune interatomic interactions. This possibility goes back to the Fano-Feshbach resonance mechanism, which shall be outlined very briefly here. More details, both on theoretical and practical aspects, can be found in a detailed review [88]. The basic mechanism behind a Feshbach resonance is depicted in figure 1.16. For a resonance to occur, we need at least two distinct channels in which the collision may take place, which at asymptotic internuclear separations would correspond to two different combinations of atomic quantum numbers. For the alkali atoms of interest, these typically correspond to a different hyperfine state for one of the collision partners. The quantum numbers used for the description of binary molecules with short internuclear separation are different from the atomic ones. As a consequence, the coupling scheme of angular momenta changes with the internuclear distance, and the two atomic channels are coupled at

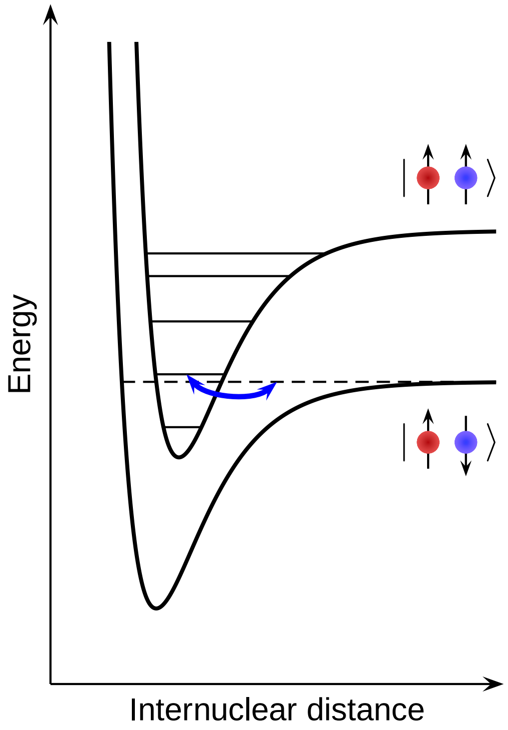

Figure 1.16: Feshbach resonance mechanism. The basic ingredients are two scattering channels with different Born-Oppenheimer potentials, asymptotically connected to different hyperfine states of one of the atoms. At intermediate internuclear distances, the recoupling from atomic to molecular hyperfine structure mixes the channels, leading to a resonant contribution to the scattering phase (and hence the scattering length) in the vicinity of a bound state in the closed channel.

intermediate distance. Therefore, some fraction of the incoming wave in the input channel of the collision may leak into the second channel, where it will pick up a collisional phase different from the one acquired in the input channel. However, the effect of such interchannel coupling will in general be small, unless resonantly enhanced by the appearance of a bound state in the second channel close to the threshold defined by the kinetic energy of the collision, which, for the cases of interest here, can safely be set to zero. In the vicinity of such a resonance, the scattering length will show a pole, going to negative (positive) infinity when approaching the bound state from below (above). Fano-Feshbach resonances have first been observed in collision experiments with nuclear matter, where the kinetic energies are substantial and largely tunable. The appearence of a Feshbach resonance feature in ultracold collisions however would require a bound state in the second channel very close to threshold, which rarely happens in nature. However, the two channels in question often correspond to different magnetic moments, allowing for tuning of the energy offset between the different potential curves exploiting the Zeeman effect. Therefore, it is often possible to continously tune over the resonance feature by applying appropriate magnetic fields. In many situations, a parametrisation of the resonant enhancement of the scattering length of the form

$$a(B) = a_{bg}\left(1 - \frac{\Delta}{B - B_0}\right) \tag{1.13}$$

is possible, with a_{bg} the off-resonant *background* scattering length of the input channel, B_0 the resonance center position, and Δ the resonance width, which is affected both by the strength of the interchannel coupling and the differential Zeeman sensitivity of the two channels. For a resonance to be of interest in the experiment, both the resonance position and the quality factor Δ/B_0 need to fall into practical windows. In order to detect the presence of Feshbach resonances, particle loss rates can be observed for varying magnetic fields. In the vicinity of the resonance, the interchannel coupling opens an additional loss channel due to resonantly enhanced formation of molecules. This technique, known as Feshbach spectroscopy, has been performed for many atomic species and scattering channels, yet, new resonances are still being found on a regular basis, and serve to improve the knowledge about the interatomic potentials.

Heteronuclear Feshbach resonances in the ^{87}Rb^{40}K mixture

A practically useful Feshbach resonance for pure ^{87}Rb gases is known to exist at 1007 G [101], which is beyond the field range which can easily be covered with our apparatus. A very narrow resonance exists at 551.5 G [101], and can be used for calibration purposes. The observation of this high quality factor ($\frac{\Delta}{B_0} \approx 4 \times 10^{-4}$) resonance in the loss of Rubidium $|F = 1, m_F = +1\rangle$ atoms (see figure 1.17) also serves as a benchmark for the magnetic field short term stability and long term reproducibility. However, such extremely narrow resonances are usually not suitable for tuning of interactions. In the context of this thesis, we are primarily interested in tuning the interspecies interaction. Several Feshbach resonances have been predicted and observed for the combination of ^{87}Rb and ^{40}K [140, 76, 86]. The most useful resonance occurs in the absolute ground state channel

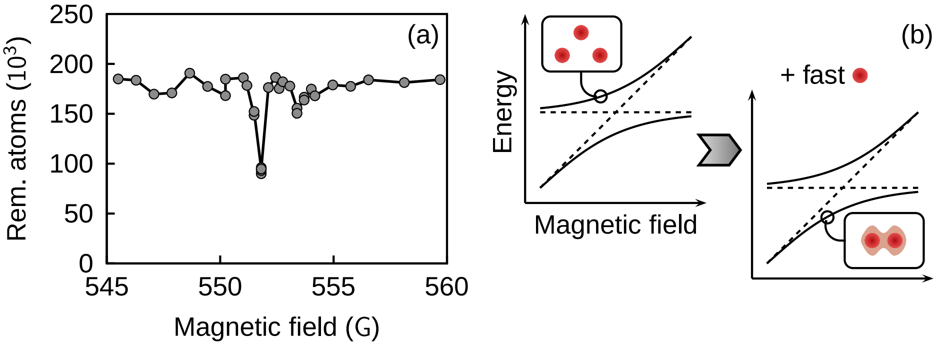

Figure 1.17: Feshbach spectroscopy on a pure bosonic ^{87}Rb quantum gas. (a) Atom loss feature induced by a Feshbach resonance in the ground state $|F=1, m_F=+1\rangle \otimes |F=1, m_F=+1\rangle$ collision channel. The observed width indicates a magnetic field stability better than 50 mG. (b) Resonantly enhanced three-body loss mechanism close to the two-body avoided-crossing. The third atom involved in the collision carries away the excess kinetic energy and is usually lost from the trap.

$|F=1, m_F=+1\rangle \otimes |F=\frac{9}{2}, m_F=-\frac{9}{2}\rangle$ and is located at $B_0 = 546.9$ G with a width of 2.9 G [86]. This resonance has previously been exploited to tune interspecies interactions in bulk [117]. In order to locate the resonance, we perform Feshbach spectroscopy with the mixture in the absolute hyperfine ground state. To this end, we expose the mixture in the dipole trap to a homogeneous magnetic field for 500 ms, and measure the number of remaining atoms after this hold time. The results can be normalized to the atom numbers obtained without the magnetic field present to yield the resonant loss feature, which is shown in figure 1.18. From this measurement, we obtain the resonance position $B_0 = 546.97 \pm 0.09$ G and an experimental width[23] of 2.0 ± 0.2 G, in good agreement with the data from reference [86].

In the course of these investigations, a smaller loss feature could sometimes also be observed, which we attribute to a small admixture of Rubidium atoms in the $|F=1, m_F=0\rangle$ state[24]. Some evidence of a similar

---

[23] The experimentally observed width in loss-based Feshbach-spectroscopy depends on details of the specific experimental situation, such as the particle density or the trap depth, and should therefore not be compared with the theoretical width, which solely depends on the molecular physics of the colliding pair.

[24] This admixture can be caused by Raman transitions driven by the two beams of the dipole trap, the frequency difference between which becomes resonant to the $|F=1, m_F=+1\rangle \rightarrow |F=1, m_F=0\rangle$ Zeeman transition at intermediate magnetic fields

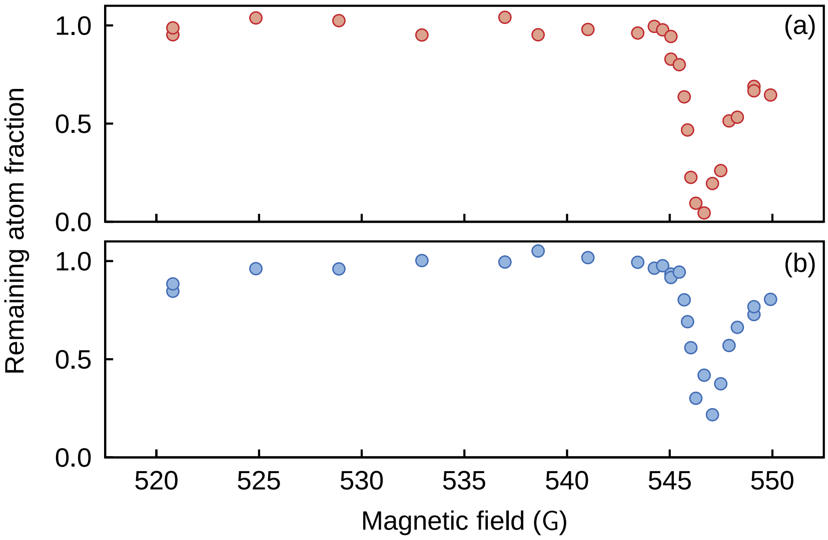

Figure 1.18: Feshbach spectroscopy on mixture of ^{87}Rb and ^{40}K atoms in the collision channel $|F = 1, m_F = +1\rangle \otimes |F = \frac{9}{2}, m_F = -\frac{9}{2}\rangle$ in the crossed dipole trap. The resonance features for fermions (upper panel) and bosons (lower panel) coincide within the experimental resolution. The left-right asymmetry around the resonance is due to losses during the relatively slow ramp through the resonance field region.

feature at the same field can be found in works both by the Hamburg and Florence groups (see e.g. figure 4.8 in [116] and figure 6 in [107]). A Feshbach resonance in the $|F = 1, m_F = 0\rangle \otimes |F = \frac{9}{2}, m_F = -\frac{9}{2}\rangle$ collision channel has been predicted in [140]. However, previous attempts to cleanly demonstrate this feature were hindered by complications in the state preparation [36]. We have been able to prepare a mixture of these states with a purity exceeding 90% of the $m_F = 0$ component. To this end, we have ramped up the magnetic field to approximately 206 G with the atoms still in the fully stretched spin state. After transferring the Rubidium atoms to the $|F = 1, m_F = 1\rangle$ state by means of microwave frequency RAP, we lower the field to 132 G, where we prepare a fifty-fifty mixture of the $m_F = +1$ and $m_F = 0$ state by RF excitation at 91 G, with a pulse duration far beyond the coherence time given by the magnetic field stability. Although this scheme halves the number of available $m_F = 0$ atoms, it is relatively stable, which allows a reasonable signal-to-noise ratio with few measurements. Next, we need to clean away the residual $|F = 1, m_F = +1\rangle$

---

around 28 G in our case.

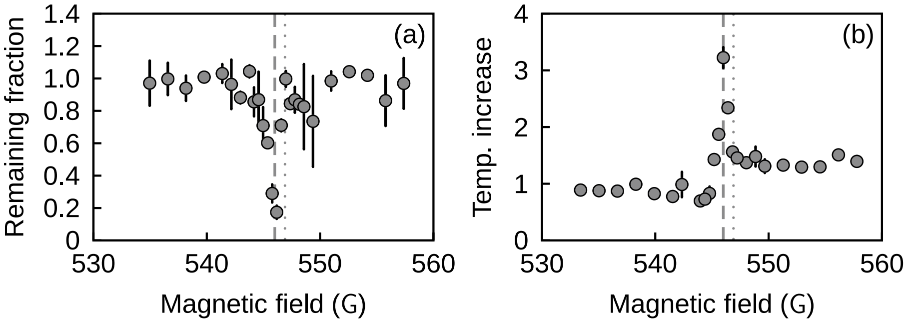

Figure 1.19: Feshbach spectroscopy on mixture of ^{87}Rb and ^{40}K atoms in the $|F=1,m_F=0\rangle\otimes|F=\frac{9}{2},m_F=-\frac{9}{2}\rangle$ collision channel in the crossed dipole trap. (a) The atom loss signature (shown for fermionic component) is obscured by instabilities in the corresponding state preparation sequence. (b) The resonance can be observed more clearly by observing the increased heating in the vicinity of the resonance (shown for the bosonic component). The dashed line indicates the extracted resonance position, while the dotted line represents the closeby resonance in the $|F=1,m_F=+1\rangle\otimes|F=\frac{9}{2},m_F=-\frac{9}{2}\rangle$ channel.

population. In order to do this, we lower the magnetic field to 49 G, which allows us to transfer these atoms into the $|F=2,m_F=+1\rangle$ state by means of microwave frequency RAP. Finally, we lower the field further to approximately 31 G, where we clean away these atoms by a resonant light pulse of approximately 1 ms duration, which leaves the $|F=1,m_F=0\rangle$ population unaffected. Finally, we transfer the Potassium atoms to the $m_F=-\frac{9}{2}$ state by RF RAP and ramp the magnetic field back up. Using this sequence, we were able to observe the Feshbach resonance in the corresponding channel cleanly, as can be seen in figure 1.19. While loss data are still a bit obscured by residual instabilities in the preparation sequence, the resonance can very clearly be observed in the heating rates of the mixture in the dipole trap. The observed resonance position is located at $B_0=546.0\pm0.1$ G. An independent confirmation of this resonance has also been reported soon after this measurement in reference [86].

Feshbach offset field

As outlined above, the Feshbach resonance of practical interest for our experiments is located around $B_0=546.9$ G. Such strong homogeneous magnetic fields are hard to realize in the experiment unless the distance from the current-carrying coils to the trap position is small. The coils of the quadrupole trap are located closest to the atoms, they provide a good approximation of an anti-Helmholtz-field configuration. Therefore, the straightforward approach here is to invert the current in one of these coils[25]. Using this configuration, the interspecies Feshbach resonance can be addressed using currents as low as 35 A, which is a big advantage in terms of power dissipation and thermal stability. Also, the corresponding currents can be switched using power MOSFETs. The current is derived from a regulated power supply[26]. We have set up an external feedback loop controlling the voltage programming port of the power supply. The error signal is derived from a current measurement using a high-sensitivity compensating inductive current sensor[27]. Additionally, the current programming port is used to limit the step response of the power supply during ramp-up of the magnetic field, thus preventing overshoots, ringing and oscillations which may occur due to the complex interplay between coil and wire inductance, output capacitance of the power supply, and the phase reserve of the power supply's internal feedback loop.

Calibration of magnetic fields and precision of Feshbach control

In principle, magnetic fields can be calibrated very sensitively via microwave spectroscopy on the $F = 1 \rightarrow F = 2$ hyperfine transitions of ^{87}Rb. Atoms transferred to the $F = 2$ manifold are detected state-selectively by imaging without repumping light. This approach is however technically limited to fields of up to approximately 200 G, due to the finite bandwidth of our microwave power amplifier. Above this value, we remove the Rubidium atoms from the trap and perform radio frequency spectroscopy on the $|F = \frac{9}{2}, m_F = -\frac{9}{2}\rangle \rightarrow |F = \frac{9}{2}, m_F = -\frac{7}{2}\rangle$ transition in Potassium. A Stern-Gerlach detection scheme is then applied in order to determine the transfer into the $m_F = -\frac{7}{2}$ state as a function of the applied radiofrequency. A typical calibration spectrum, taken with 100 ms square pulses with a power level of -5 dBm is shown in figure 1.20. The line center position of 80.5563 ± 0.0002 MHz corresponds to a magnetic field of 553.907 ± 0.005 G. From the linewidth of 3.7 ± 0.3 kHz, we deduce a magnetic field stability over 100 ms of ≈ 55 mG at these high fields, corresponding to a noise level of 1×10^{-4}.

---

[25] This can be accomplished using MOSFETs as multiplexing elements in combination with an external break-before-make logic.

[26] FUG NLN750M15, with a current rating of 50 A and a noise level below 5×10^{-4}.

[27] Danphysik Ultrastab 860R

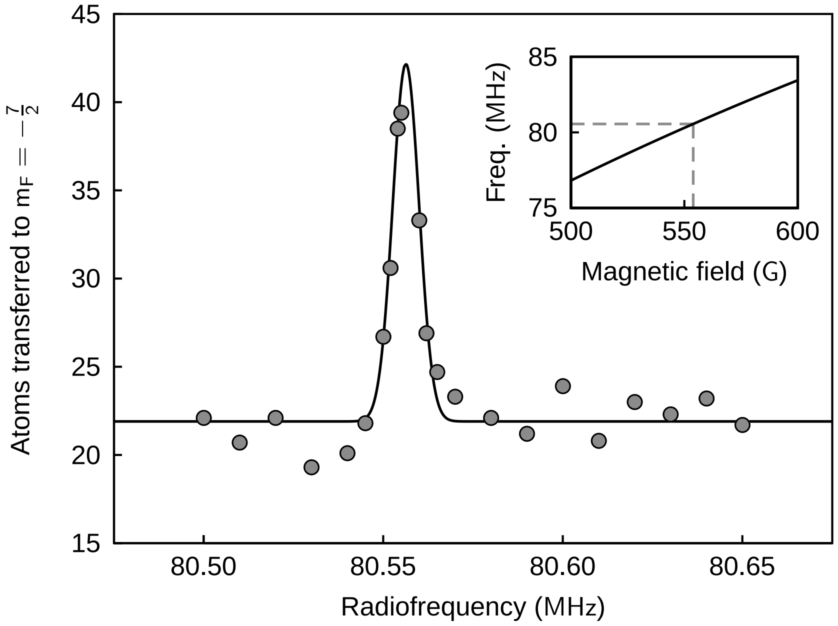

Figure 1.20: Radiofrequency spectrum of ^{40}K $|F = \frac{9}{2}, m_F = -\frac{9}{2}|F = \frac{9}{2}, m_F = -\frac{7}{2}\rangle$ transition at high magnetic field. The solid line is the result of a Gaussian fit, displaying a linewidth of $3.7 \pm 0.3\,$kHz. The finite off-resonant background is due to both imperfect initial-state preparation and signal-to-noise issues in the absorption images. The inset shows the magnetic field sensitivity of the transition, given by the Breit-Rabi formula.

The day-to-day reproducibility is beyond our measurement resolution. An additional calibration point in the direct vicinity of the resonance position of interest is obtained by the homonuclear Rubidium Feshbach resonance in the $|F = 1, mF = 1\rangle + |F = 1, mF = 1\rangle$ channel mentioned above. By comparison of the resonance position reported in reference [101] with our data, we can estimate the absolute accuracy of our calibration to be better than 50 mG. With these values, and using the parametrization of the interspecies Feshbach resonance from reference [86], we expect a noise-limited programming resolution and an accuracy both on the order of $3\,\mathrm{a}_0$ around the zero-crossing of the interspecies scattering length. For repulsive interactions, the precision is slightly worse. We therefore believe that the largest uncertainty in determining the scattering length for our experiment is in fact given by the limited precision of the parametrization.

1.6 Raman interaction switching

Raman switching of interspecies interactions

For many experiments, it is crucial to be able to change the interspecies interaction abruptly. While a Feshbach resonance does allow for tunability, a fast change of the scattering length requires fast changes of the magnetic field, which can be hard to achieve due to induction effects in the coils providing the field. Also, power supplies connected to a non-ohmic load tend to start oscillating upon fast changes of the programming value. These effects limit the timescale on which the interaction strength can be changed deterministically in our experiment to about ten milliseconds, which is clearly not fast enough in some circumstances. An alternative approach for switching the interaction strength makes use of the fact that the interspecies s-wave scattering length is in general dependent on the hyperfine and Zeeman state of the atoms. This effect can be largely enhanced if one of the states features a closeby Feshbach resonance. In this case, switching between an almost arbitrary scattering length in the resonant channel and the background scattering length in the other channel becomes possible, if a hyperfine or Zeeman transition is driven at a suitable magnetic field. In our experimental situation, the tunable state is the $|F = \frac{9}{2}, m_F = -\frac{9}{2}\rangle$ state, which can be coupled to the $|F = \frac{9}{2}, m_F = -\frac{7}{2}\rangle$ state. While it is possible to directly drive the magnetic dipole transition between these two states via radio-frequency, far stronger couplings (and thus faster interaction switching) can be achieved with a stimulated optical Raman transition close to the D2 transition. In the vicinity of the Feshbach resonance of interest, this transition needs a two-photon detuning in the range of 78 MHz to 81 MHz. It is therefore possible to derive both light fields from a single diode laser, using acousto-optic modulators to imprint the frequency difference [28]. The frequency of the diode laser itself is referenced to a cavity using a Pound-Drever-Hall locking scheme[41]. In order to eliminate frequency drifts caused by thermal fluctuations of the cavity length, the cavity is temperature-stabilized on the 10^{-2} K level. Both the absolute detuning with respect to the D2 line and its stability over time is monitored using

---

[28] Both AOM drivers are fed by analog synthesizers, both referenced to a common 10 MHz master clock, in order to stabilize the difference frequency. An alternative scheme using phase-locked voltage-controlled oscillators (VCOs) also works, but at the prize of relatively poor tunability. Two independent VCOs show an instantaneous linewidth of the beat note of ≈ 1 kHz, with a drift of up to 10 kHz/min, prohibitive to use in the experiment.

a high-resolution wavemeter[29]. Both Raman beams are recombined with orthogonal polarization into a single-mode polarization-maintaining optical fibre. It is then possible to measure the beat note between the two Raman beams by inserting a polarizer turned by 45° into the beam path after the fiber. To this end, a fast amplified photodiode[30] is connected to a spectrum analyzer. The result of this measurement can be seen in figure 1.21. The instantaneous linewidth is below the 3 Hz resolution limit of the spectrum analyzer used, with no observable drift. Still, the spectrum of the beat note shows non-negligible components at even multiples of the 50 Hz power line frequency. These could be due to fluctuations of the RF power in the AOMs caused by the typically poor supply rejection of broadband RF amplifiers. While these frequency components are irrelevant in the context of the experiments in this thesis, where the spectrum is effectively Fourier-limited, they could become an issue in high-resolution spectroscopy. The total power level (i.e. the sum of the two beam intensities) is stabilized using a pick-up photodiode after the fiber output and feedback via a common AOM in front of the initial beam splitter, allowing both the compensation of shot-to-shot variations and the temporal shaping of pulses on a few-microsecond scale[31]. After the fiber, the beams propagate towards the atoms on the y-axis, under a small angle with both the dipole trap beam and the lattice beam to be discussed in the next chapter, and orthogonal to the direction of the Feshbach magnetic field. The chosen beam waist of $w_0 = 160\ \mu$m is large enough to provide an essentially homogeneous intensity profile over the extent of the atomic cloud, while still delivering the necessary intensity needed for a strong coupling. The detuning with respect to the D2 transition can be found by scanning the Raman reference cavity length using a piezo actuator on one of the cavity mirrors. We then monitor the atom loss caused by shining in the Raman beams on a pure Potassium cloud in the dipole trap for a fixed time. The corresponding spectrum can be seen in figure 1.22. Three resonances are clearly visible. The relative strength of these resonances can be manipulated by turning the polarization of both

---

29) HighFinesse Angstrom, with a nominal resolution of 100 MHz

30) Hamamatsu PD on Kuhne broadband amplifier

31) This setup can not compensate the aforementioned power-line-induced fluctuations, as it stabilizes the sum of the individual intensities, while the physically more relevant quantity would be their product. Therefore, the stabilization crucially relies on the fact that fluctuations in both beams preserve their power ratio. Individual stabilization of the two beams on the level required to eliminate the residual power line components seems challenging in the present configuration. However, it would be straightforward if a different (e.g. counterpropagating) beam geometry was used.

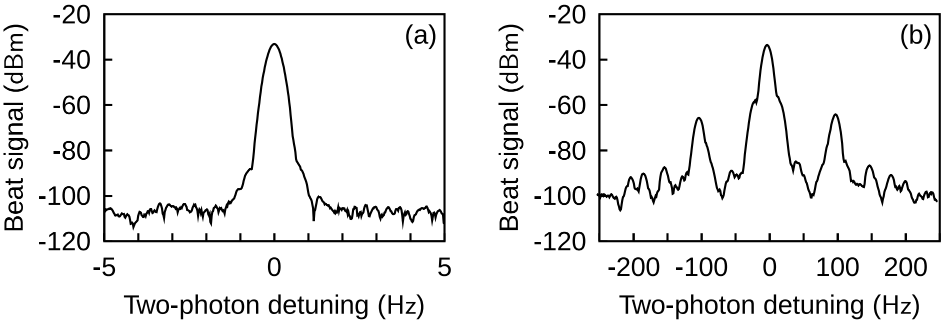

Figure 1.21: Beat note of the two Raman beams after the optical fiber. recorded with (a) 300 Hz and (b) 3 Hz resolution bandwidth, averaged over ten sequential sweeps. Apart from the very narrow resolution-limited central peak, a progression of sidebands at even multiples of the powerline frequency is visible, at a suppression of approximately 30 dB.

Raman beams simultaneously using a $\lambda/2$-waveplate. To understand the triple resonance structure, it is important to note that while the hyperfine ground state as a stretched state experiences a linear Zeeman effect at all magnetic fields, the excited $5P_{3/2}$ state has a hyperfine splitting of only few MHz. Therefore, it is already deeply in the Paschen-Back regime at the magnetic fields of interest and has to be analyzed in a decoupled $|J, m_J, I, m_I\rangle$ basis. The D2 transition connects $J = \frac{1}{2} \to J' = \frac{3}{2}$ as always. Being a stretched state, the initial state has maximum allowed projection quantum numbers $m_J = -\frac{1}{2}$, $m_I = -4$. Recalling that electric dipole transitions do not change the nuclear spin, we therefore obtain three allowed transitions, namely

$$\begin{aligned} \sigma^- : \quad & m_J = -\tfrac{1}{2} && \longrightarrow && m'_J = -\tfrac{3}{2}, \\ \pi : \quad & m_J = -\tfrac{1}{2} && \longrightarrow && m'_J = -\tfrac{1}{2}, \\ \sigma^+ : \quad & m_J = -\tfrac{1}{2} && \longrightarrow && m'_J = +\tfrac{1}{2}, \end{aligned}$$

giving rise to the observed resonance structure. While all of the above-mentioned transitions may account for spontaneous scattering of a single photon and therefore necessitate a sufficient detuning, only two of them are actually contributing to the Raman process, as the conservation of nuclear spin projection quantum number allows coupling only to the $m''_J = +\frac{1}{2}, m''_I = -4$ component of the $m_F = -\frac{7}{2}$ state, thereby suppressing contributions from the above-listed σ^- transition[32]. The two possible

---

[32] Clearly, the same reasoning applies if the two-photon transition is analyzed in the coupled basis.

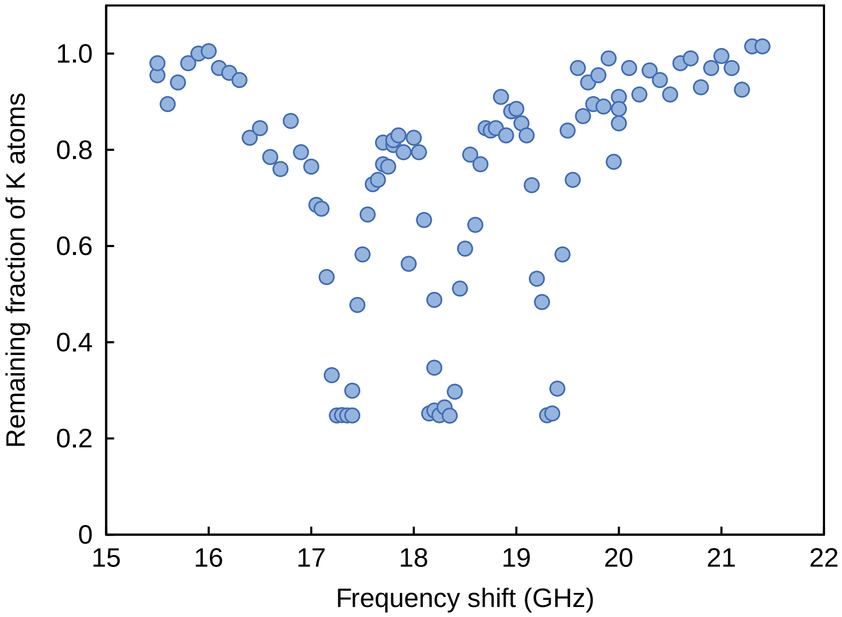

Figure 1.22: Single-photon spectrum of Potassium atoms in their hyperfine ground state at a magnetic field of 525.90 G. The atomic cloud was illuminated for 100 μs with the full available power. The triplet structure of the resonance can be traced back to the Paschen-Back effect of the excited state.

two-photon pathways are thus

$$\begin{aligned}\uparrow\searrow: &\quad m_J = -\tfrac{1}{2} &\longrightarrow&\quad m'_J = -\tfrac{3}{2} &\longrightarrow&\quad m''_J = +\tfrac{1}{2},\\ \nearrow\downarrow: &\quad m_J = -\tfrac{1}{2} &\longrightarrow&\quad m'_J = +\tfrac{1}{2} &\longrightarrow&\quad m''_J = +\tfrac{1}{2},\end{aligned}$$

In our setup, the orthogonal polarization of the two beams emanating from the fiber yields the combination of one σ^+- and one π-photon required by the selection rules, as the propagation direction of the Raman beam is orthogonal to the magnetic field. It should however be noted that half of the power of the light which is linearly polarized in the direction orthogonal to the magnetic field is wasted, as it could only drive the σ^- transition. In order to obtain optimal two-photon coupling at the given laser power, the intensity balance between the two Raman beams has been adapted to compensate for this effect. Next, we analyze the resulting Raman coupling. At a given intermediate-state detuning, we can induce Rabi flopping between the two coupled ground states for some time, and subsequently measure the fraction of atoms in either of the two states using Stern-Gerlach detection. Figure 1.23 shows Rabi oscillations recorded this way at an intermediate state detuning of approximately 400 MHz. The observed Rabi frequency is 48 kHz. The amplitude is only slightly above 70% of the theoretical value, which is mostly due to a finite initial population in the $m_F = -\frac{7}{2}$ state of about 5% and unequal detection probabilities for the two Zeeman states. Correcting for these systematic errors, we can infer a two-photon detuning of about 10 kHz for the trace in question, leaving us with a bare (resonant) Rabi frequency of 46 kHz, corresponding to a π-pulse duration of 11 μs. Although the signal to noise ratio of these oscillations is rather good, we still decided to use a RAP sequence instead of a π-pulse for practical interaction switching in the experiments, in order to avoid complications with possibly inhomogeneous interaction shifts of the transition frequencies. To this end, we scan one of the AOM-frequencies in a linear ramp over 500 kHz, thereby changing the two-photon detuning, while keeping the intermediate state detuning essentially fixed. We find that efficient transfer can be achieved for RAP durations as short as 50 μs.

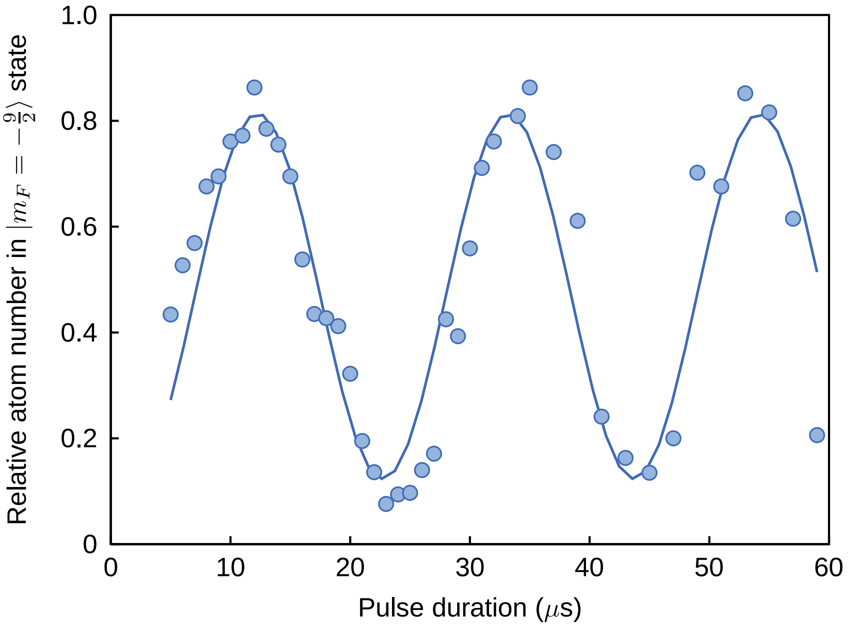

Figure 1.23: Raman Rabi oscillation between the $m_F = -\frac{9}{2}$ and $m_F = -\frac{7}{2}$ states, at an intermediate-state detuning of approximately 400 MHz.

1.7 Absorption imaging

Information on ultracold quantum gases is almost exclusively obtained by optical imaging techniques[33]. The most common imaging method, which was also used for all the work presented in this thesis[34], is based on the absorption of resonant light by the atomic cloud. To this end, the atoms are illuminated by a resonant laser beam, with a beam waist large compared to the extension of the atomic cloud. The shadow cast by the atoms due to resonant absorption is then recorded on a CCD[35] camera, resulting in a signal image $\rho_s(x, y)$, where (x, y) denote the pixel coordinates (not to be confused with the physical x and y directions), which is related to the atomic density integrated along the line of sight (so-called column density) via the law of Lambert and Beer

$$\rho_s(x, y) = \mathcal{I}_0(x, y)\, e^{-\sigma \int n(x,y,z)\, dz}\,, \tag{1.14}$$

where σ is the resonant absorption cross section. A reference image $\rho_r(x, y)$ is taken after the atoms are out of sight, recording the bare intensity distribution $\mathcal{I}_0(x, y)$. Finally, a darkground image $\rho_d(x, y)$ is recorded without any illumination, in order to cancel the CCD background, and the integrated atomic density is calculated as

$$\int n(x, y, z)\, dz = -\frac{1}{\sigma} \log \frac{\rho_s(x, y) - \rho_d(x, y)}{\rho_r(x, y) - \rho_d(x, y)}. \tag{1.15}$$

For sufficiently long time of flight, the initial cloud size in the trap can be neglected, and the resulting atomic density after time of flight directly represents the momentum distribution at the moment of release. By virtue of the Fourier-transform pair relationship between momentum and position, small spatial structures in the trapped system translate into a large-scale pattern during TOF, while large-scale structures give rise to sharp features. The smallest structure which can be resolved in the TOF-expanded absorption images is limited both by the bare optical resolution, given by the numerical aperture of the imaging system, and the recoil-induced momentum diffusion which tends to smear out the atomic density distribution during the finite

---

[33] For interesting alternative approaches, see e.g. references [16, 23, 28, 54].

[34] The experimental apparatus presented in this work is also equipped with a phase-contrast imaging system suitable mainly for potassium atoms, which has been crucial in recent work on fermionic spin mixtures [138, 64], but which will not be discussed here. See [137, 155] for details.

[35] CCD = Charge coupled device

exposure time. These limitations will be of particular interest in section 2.4, where we consider the extraction of correlation information from the atomic shot noise in the TOF images.

Two

Noninteracting ultracold atoms in optical lattices

This chapter reviews the essential concepts of optical lattice potentials as far as necessary for the experiments presented in this thesis. We calculate the relevant experimental parameters and motivate the choices taken in the design of the experimental apparatus. We also demonstrate the central properties of noninteracting Bosons and Fermions in the optical lattice. Among these are the anticorrelations that have been observed in the density of a single-species Fermi gas, a result which has been published in reference [131].

2.1 Blue-detuned optical lattices

Standing wave optical lattices

Once we have prepared an ultracold ensemble in the dipole trap, we can impose a threedimensional (3d) optical lattice on the atoms. An optical lattice is a periodic dipole potential. It is usually created by overlapping two or more coherent laser beams, which then form a standing wave intensity pattern. The simplest configuration of an optical lattice can be obtained by retro-reflecting a laser beam from a high-quality mirror, leading to a standing wave along the optical axis. This results in a potential

$$V_L(x) = V_0 \cdot \sin^2(k_L\, x), \tag{2.1}$$

where $k_L = 2\,\pi/\lambda_L$ is the wavenumber of the light field of wavelength λ_L. Obviously, the resulting potential is periodic with a period of $\lambda_L/2$. A variety of geometries is conceivable for higher-dimensional optical lattices, most

3d optical lattice experiments however work with a simple cubic lattice geometry, made up of three independent and pairwise orthogonal standing waves, mainly due to the relative simplicity of this setup. The same configuration was chosen in the present experiment.

Lattice wavelength

The second important choice in constructing an optical lattice experiment is the wavelength of the lattice light. For a mixture experiment, this is a relatively subtle question, in contrast to the case of a single atomic species, where usually the availability of a suitable laser source is the main criterion[1]. In the mixture case, however, both species will in general have a different AC polarizability $\alpha(\omega)$. However, as the D-lines of Potassium and Rubidium atoms are relatively close to one another, we can hope for a wavelength which produces a sizeable AC Stark shift in both species, such that optical lattices of comparable strength can be tailored. On the other hand, this close proximity renders species-specific optical lattice schemes, as described e.g. in reference [93], rather unfavourable. Figure 2.1 shows the polarizability of both species over the interesting wavelength range, normalized by the respective recoil energy

$$E_r = \frac{\hbar^2 k^2}{2\,m}, \tag{2.2}$$

where $k = \frac{2\pi}{\lambda}$ is the wavenumber of the lattice light. This normalized quantity is directly proportional to the dimensionless lattice depth

$$\tilde{V}_0 = \frac{V_0}{E_r}. \tag{2.3}$$

In principle, both the wavelength range above the Rubidium D1 line at 795.0 nm and below the Potassium D2 line at 766.7 nm can be used. While the former range has been used for many previous experiments on Rubidium atoms in optical lattices, it clearly offers very limited tunability of the lattice depth ratio between the two species, i.e. the relative mobility, as the optical lattice experienced by the Rubidium atoms is always deeper than the Potassium lattice (by a factor between 3.3 and 2.2 for realistic detunings[2]). The latter blue-detuned wavelength range is more favorable in terms of tunability, as it features a *magic* wavelength at approximately 755.5 nm,

---

[1] Another important trade-off might be between finite tunneling timescales and sufficiently large spacing to optically resolve individual lattice sites.

[2] At very large detuning, such as can be realized using YAG or fiber lasers, the ratio tends towards the mass ratio $m_b/m_f \approx 2.2$.

where both species experience the same optical lattice. Around this point, it is possible to realize lattice depth ratios between approximately 0.7 and 1.6. Furthermore, this whole tuning range lies within the operating window of a standard CW TiSa laser. At this point, it is important to note that in a standing wave optical lattice, the relatively small detuning with respect to the Potassium D2 resonance is not a serious issue, as the atoms are effectively pushed into the antinodes of the light field and thus see a significantly reduced light intensity[3]. An additional interesting effect of the blue-detuned optical lattice is the global anticonfinement, which we will discuss later in this section. First, however, we shall have a look at the actual optics setup for the optical lattice.

Optical setup

We shall shortly discuss the optics arrangement used in the experiments. A schematic representation can be found in appendix C. The laser beams for all individual lattice axes are derived from a single tunable laser[4]. The light is divided between the different axes via polarization optics. Each axis uses its own acousto-optical modulator both for intensity regulation and frequency shifting. By running the modulators at different driving frequencies and making use of both first positive and negative diffraction orders, frequency offsets between the different axes of a least 20 MHz can be achieved, effectively averaging out interference between the axes on sub-microsecond timescale. Additionally, the polarization is chosen orthogonally for the different axes. The light is delivered to the experiment via single mode polarization maintaining optical fibers, followed by a Faraday isolator in order to prevent backreflection of the retro beam from the fiber facet. The beam waist and longitudinal focus position on the atoms are ensured by two sequential telescopes, with the atomic cloud situated roughly in the focus of the second telescope. On both horizontal axes, dichroic mirrors are used to separate the lattice light from the dipole beams, while the imaging light is separated via the polarization degree of freedom. An additional lens of short focal length is used to build a cat's eye configuration retro mirror. This ensures good matching of the beam waist of the incoming and retroreflected beams at the position of the atoms. Finally, pickup photodiodes are used to regulate the lattice intensity on a 10^{-4} stability level. To this end,

---

[3] Interestingly, spontaneous scattering rates can actually be suppressed when the intensity of the lattice beams is increased, due to the localization in the antinodes.

[4] Coherent MBR Ti:Sa system, pumped by Verdi V18

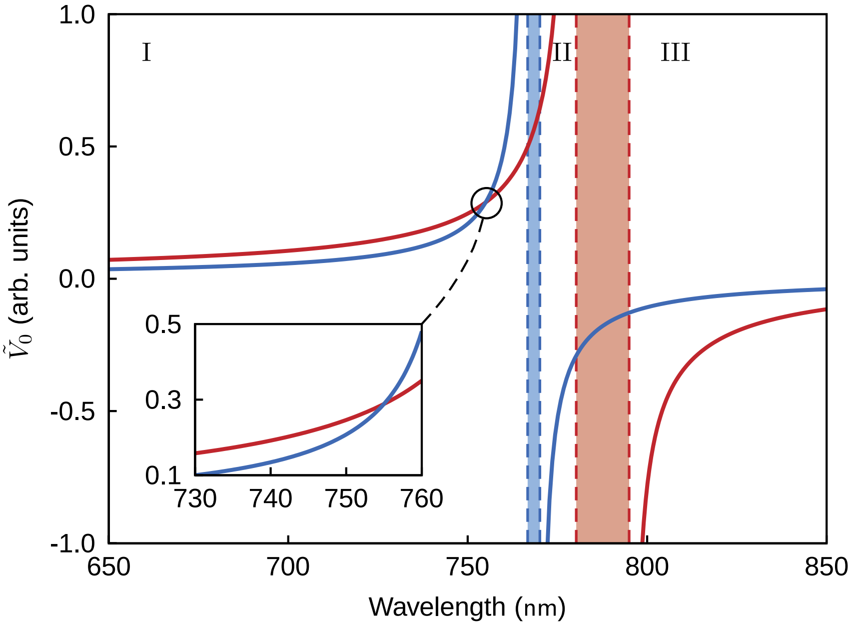

Figure 2.1: Optical lattice depth in units of the recoil energy, for Rubidium (red curve) and Potassium (blue curve), as a function of lattice wavelength. The dashed lines indicate the positions of the D2 and D1 resonances of the two species. The shaded areas in between the respective D2 and D1 line give rise to spin-dependent optical lattices and are of no practical use in the context of this work. The remaining wavelength ranges fall into three intervals, labelled by I, II and III. Intervals I and III correspond to blue- and red-detuned optical lattices. Interval II is red-detuned with respect to Potassium, but blue-detuned with respect to Rubidium, and is also not useful in this context. The region around the magic wavelength at 755.5 nm, which allows to tune the relative mobility of the two species, is shown with higher resolution in the inset.

feedback is given onto the driver providing the RF power for the AOM in front of the optical fiber.

(Anti-)confinement

Most optical lattice experiments to date have been working with red-detuned optical lattices, in which atoms are attracted to the intensity maxima, and the standing wave is truly trapping the atoms, i.e. the intensity maxima constitute the global minima of potential energy. In contrast, for a blue-detuned optical lattice, the atoms are attracted to the intensity nodes, the potential energy of which is equal to the asymptotic value for an atom *far out* of the Gaussian beam, if the standing wave pattern is maximally modulated. However, in the real experimental situation, perfect modulation can never be achieved, because of intensity losses of the retro-reflected beam, as well as slight mismatches of the polarization, beam waist, or focal point, between the incoming and reflected beam. Therefore, we always have some travelling-wave component present, which energetically lifts the intensity minima above the asymptotic potential energy value. Thereby, atoms can no longer truly be trapped in the lattice beam, although, depending on the height of the potential barriers, they can still remain in a kind of metastable trapping state for considerable time. The potential energy of the individual lattice sites follows an *anticonfining* Gaussian shape transversely to the beam. Besides this technical limitation, there is a second, more fundamental reason for transversal anticonfinement from a blue-detuned lattice, which can be associated with kinetic rather than potential energy. The appearance of the standing wave potential leads to the formation of band structure, as will be detailed in the following section. As a consequence, the lowest bound state in the standing wave potential is elevated above the bottom of the potential by a zero point energy ϵ_0. However, the depth of the periodic potential varies transversally across the beam. The zero point energy varies correspondingly, being largest in the beam center. For sufficiently deep periodic potentials, a scaling $\epsilon_0 \sim \sqrt{V(r)}$ can reasonably be assumed, where $V(r)$ is the standing wave (intensity) amplitude, which varies with the transversal coordinate as

$$V(r) = V_0\, e^{-2\,r^2/w^2} \tag{2.4}$$

for a beam waist w. Usually, a combination of both effects will be present, making quantitative estimates of the anticonfining potential $V_a(r)$ relatively difficult. Close to the center of the beam, where the anticonfining potential can be approximated harmonically, it can be characterized by an *antitrap-*

ping frequency ω_a, given by

$$V_a(r) = -\tfrac{1}{2}\, m\, \omega_a^2\, r^2 + \mathcal{O}(r^4), \tag{2.5}$$

and scaling as

$$\omega_a \sim V_0^\beta \quad \text{where} \quad \beta = \begin{cases} \frac{1}{2} & \text{for the bare pot. energy effect,} \\ \frac{1}{4} & \text{for the bare kin. energy effect at large } V_0 \end{cases}$$

In the presence of an external confinement, e.g. the optical dipole trap, which can be approximated by a harmonic potential of trapping frequency ω_0, the total confinement is reduced to

$$\omega_{\text{eff}} = \sqrt{\omega_0^2 - \omega_a^2} \quad \text{for} \quad \omega_0 > \omega_a. \tag{2.6}$$

For weak dipole traps, even a fully anticonfining potential is possible. In the presence of a higher-dimensional optical lattice, the same reasoning applies, and the antitrapping frequencies have to be added up quadratically for all lattice axes transversal to a given direction. Experimentally, we can measure the anticonfining frequencies indirectly as a reduction of the trapping frequencies in the presence of a transversal optical lattice according to equation 2.6, and find scaling exponents on the order of $\beta \approx 0.3$. However, these values should be taken *cum grano salis*, as they are expected to depend extremely sensitively on the optical alignment.

2.2 Band structure

Periodic potentials and Bloch's theorem

The threedimensional lattice geometry realized in our experiment is of simple cubic type. Therefore, the quantum-mechanical problem of determining the eigenstates of the atoms in the lattice is fully separable, and we can restrict our discussion to the one-dimensional case. According to Bloch's theorem [84], the periodic potential given by equation 2.1 supports eigenstates of the form

$$u_{i,q}(x) = e^{iqx} \cdot \phi_i(x) \tag{2.7}$$

labelled by the positive integer band index i and the quasi-momentum $q \in [-\hbar\, k, +\hbar\, k]$, where $k = \frac{\pi}{\lambda/2}$ is the primitive vector of the reciprocal lattice, and ϕ is periodic with

$$\phi_i(x + \tfrac{\lambda}{2}) = \phi_i(x). \tag{2.8}$$

The details of a specific situation will only manifest themselves in the shape of the functions ϕ_i. These can easily be calculated by the following procedure: We take the Hamiltonian

$$H_L = \frac{p^2}{2m} + V_L(x) = \frac{p^2}{2m} + V_0 \sin^2 \frac{2\pi x}{\lambda} \tag{2.9}$$

for a single particle in the periodic potential and decompose the corresponding stationary Schrödinger equation

$$H_L u_{i,q} = \epsilon_{i,q} u_{i,q} \tag{2.10}$$

into Fourier components. For a generic periodic potential, this would lead to an infinite set of equations

$$\frac{\hbar^2\, q^2}{2\, m}\, c(q) + \sum_{\nu=-\infty}^{+\infty} V_{\nu k}\, c(q - \nu k) = \epsilon_q c(q) \tag{2.11}$$

for every given quasi-momentum q, where the $V_{\nu k}$ denote the coefficients in the discrete Fourier series

$$V_L(x) = \sum_{\nu=-\infty}^{+\infty} V_{\nu k}\, e^{i\,\nu\,k\,x}. \tag{2.12}$$

The problem thereby corresponds to finding the eigensystem of an infinite symmetric matrix. In the case of optical lattices, which we will restrict ourselves to in the following, the potential is perfectly sinusoidal, thus, it's Fourier series only consists of a constant offset $\frac{V_0}{2}$ and the only nonzero off-diagonal components $V_{+2\,k} = V_{-2\,k} = \frac{V_0}{4}$. The matrix thus takes the tridiagonal form:

$$\frac{E_r}{2} \cdot \begin{pmatrix} \ddots & & & & & & \\ & T_{q-2\kappa} + \tilde{V}_0 & \tilde{V}_0/2 & 0 & 0 & 0 & \\ & \tilde{V}_0/2 & T_{q-\kappa} + \tilde{V}_0 & \tilde{V}_0/2 & 0 & 0 & \\ & 0 & \tilde{V}_0/2 & T_q + \tilde{V}_0 & \tilde{V}_0/2 & 0 & \\ & 0 & 0 & \tilde{V}_0/2 & T_{q+\kappa} + \tilde{V}_0 & \tilde{V}_0/2 & \\ & 0 & 0 & 0 & \tilde{V}_0/2 & T_{q+2\kappa} + \tilde{V}_0 & \\ & & & & & & \ddots \end{pmatrix}$$

where for compactness, we have introduced $\kappa = 2\,\hbar\,k$, and the dimensionless quantities $T_{q\pm\nu\kappa} = 2\,(\tilde{q} \pm 2\,\nu)^2$ and $\tilde{q} = q/\hbar\,k$.

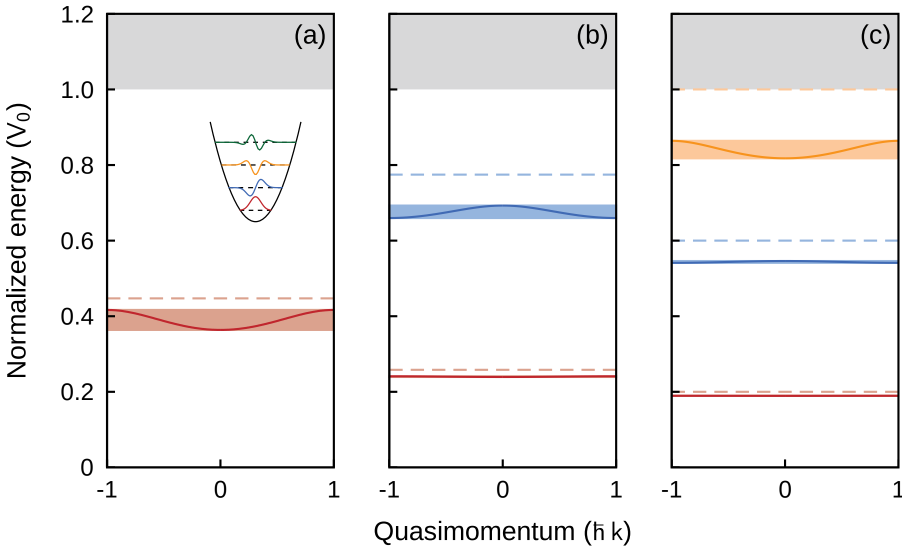

Figure 2.2: Dispersion relation for a particle in a sinusoidal potential, restricted to the first Brillouin zone, for lattice depths of (a) 5 $\mathrm{E_r}$, (b) 15 $\mathrm{E_r}$ and (c) 25 $\mathrm{E_r}$. As the potential depth increases, more and more bands are bound in the lattice potential, i.e. their energy falls below the continuum (shaded in grey), and the lower-lying bands become increasingly flat. The forbidden regions in between the bands tend towards equidistand separation of bound states, which is characteristic for the limiting case of a simple harmonic oscillator on each site, as depicted in the inset of (a).

Band structure

We can solve the above eigenvalue problem for a suitably truncated matrix for any given value $-2 < \tilde{q} < +2$ and end up with the dispersion relation $\epsilon_n(q)$, where the band index n counts the possible eigenvalues in ascending order. This dispersion relation is also known as the *band structure* of the optical lattice potential. The name reflects the central feature, which can be seen in figure 2.2. The possible eigenenergies form a band, the width of which is

$$D = |\epsilon(\hbar\, k) - \epsilon(0)| \tag{2.13}$$

and monotonically decreases as the depth of the potential increases. For suitably deep potentials, the bands can be considered essentially flat. This effect is known as *quenching* of kinetic energy. The forbidden regions in between the bands are termed band gaps. Their width

$$\Delta_q = \epsilon_{n+1}(q) - \epsilon_n(q) \tag{2.14}$$

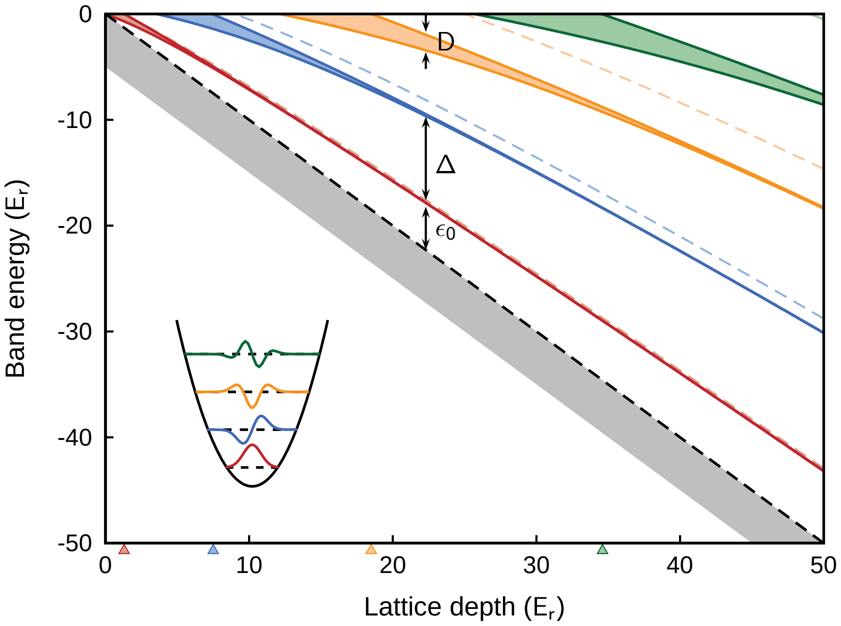

Figure 2.3: Bound states in the periodic potential of an optical lattice. As the lattice depth is increased, more bound Bloch bands (red, blue, orange and green shaded areas) appear at the positions indicated by the triangles on the abszissa. The quenching of kinetic energy is also clearly visible, especially for the lowest band. The black dashed line indicates the bottom of the potential. By ϵ_0, Δ and D, we denote the zero point energy, band gap, and band width respectively, as defined in the main text. The dashed colored lines indicate the corresponding eigenstates of the approximative harmonic well potential, as depicted in the inset.

increases for deeper potentials, and the dependence on q becomes negligible due to kinetic energy quenching. We shall therefore only refer to the band gap Δ in the following, neglecting the q dependence altogether[5].

---

[5] In more complicated potentials, such as arising in real material crystals, overlapping bands may exist, as well as a strong dependence on q, making band gaps a much more complex matter.

]

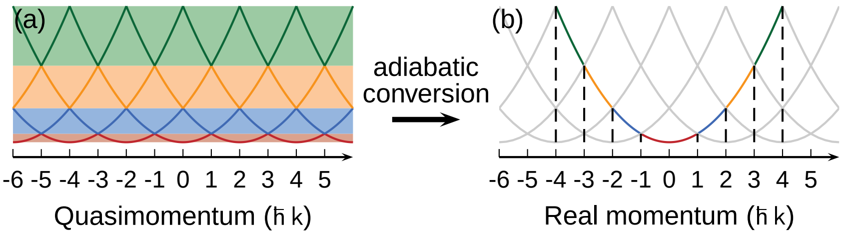

Figure 2.4: Illustration of the band-mapping technique used for the visualization of Fermi surfaces. For vanishing lattice depth, the quasi-momentum associated with the Bloch states forming the bands (a) is adiabatically converted into real momentum (b), allowing the identification of the various band contributions in TOF images.

2.3 Non-interacting quantum gases in optical lattices

Fermionic band insulator in optical lattices

When we fill the states in an optical lattice with spin-polarized Fermions one after another, and the total number of Fermions is lower than the number of states within the first Bloch band[6], we will start at the center of the first Brillouin zone (i.e. $q = 0$) and then fill up states more towards the border. The surface defined by the outermost occupied states is usually referred to as the Fermi surface.

Probing Fermi surfaces in time of flight

It is indeed possible to make these Fermi surfaces visible in the experiment, which has first been acccomplished in [87]. To illustrate the procedure, we consider now a switchoff of the optical lattice potential which is adiabatic (with respect to the band gap) instead of instantaneous. This way, the quasimomentum q is adiabatically converted into real momentum p while the band structure is morphed into the familiar free-space dispersion parabola. After sufficient time of flight, the original quasimomentum is then encoded in the particle positions. This technique, known as *Brillouin zone mapping*, is illustrated in figure 2.4. Experimentally, this method allows to estimate the filling factor of a noninteracting degenerate Fermi gas

---

[6] In a solid, the number of states is usually considered to be countably infinite, corresponding to infinite extension of the potential. This assumption is certainly invalid for optical lattices.

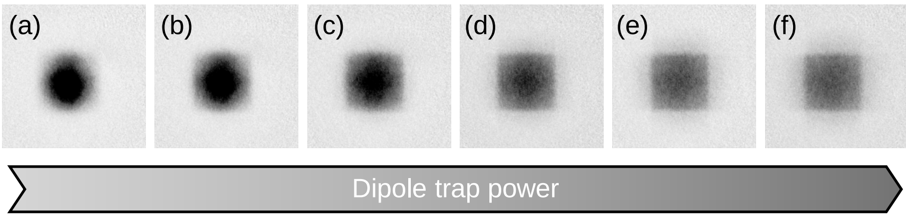

Figure 2.5: Fermi surface for atoms in a 3d optical lattice, with varying filling, visualized using the band-mapping technique. As the dipole trapped is compressed, the system evolves from a metallic state characterized by a partly filled first Brillouin zone (a)-(c) towards a band insulator (d). For stronger compression (e), the first Brillouin zone is populated perfectly homogeneously, but the higher bands also start to get populated. For very strong compression, (f), many bands are populated.

in an optical lattice. Figure 2.5 shows images of the Fermi surface for a fixed number of Fermions, but varying compression of the dipole trap potential, corresponding to a reduction of the effective system size and thereby a decrease in the number of available states. A quantitative evaluation of the corresponding TOF images is shown in figure 2.6. We evaluate the atomic density at different positions in the Brillouin zone. As the gas is compressed, the density in the center decreases, while the edge and corner of the first Brillouin zone see an increase in density. Upon formation of the band insulator, the density saturates at all positions within the first Brillouin zone, albeit not to a constant value. The resulting pattern can be understood if the true dispersion relation of the fermion system, including both the lattice and the dipole trap, is taken into account [137]. In this case, the quasimomentum is no longer the correct quantum number to label the eigenstates of the system, and the sharp zone edges are softened.

2.4 A Hanbury-Brown Twiss experiment with free Fermions

Hanbury-Brown Twiss effect for fermions

The image of a Fermi surface which reaches out to the band edge is by no means sufficient to verify the existence of a fermionic band insulator[7].

---

[7] In fact, similar pictures could arise for a thermal gas, with $D \ll k_B T \ll \Delta$ in a deep optical lattice, the only difference being that the filling factor in this situation would

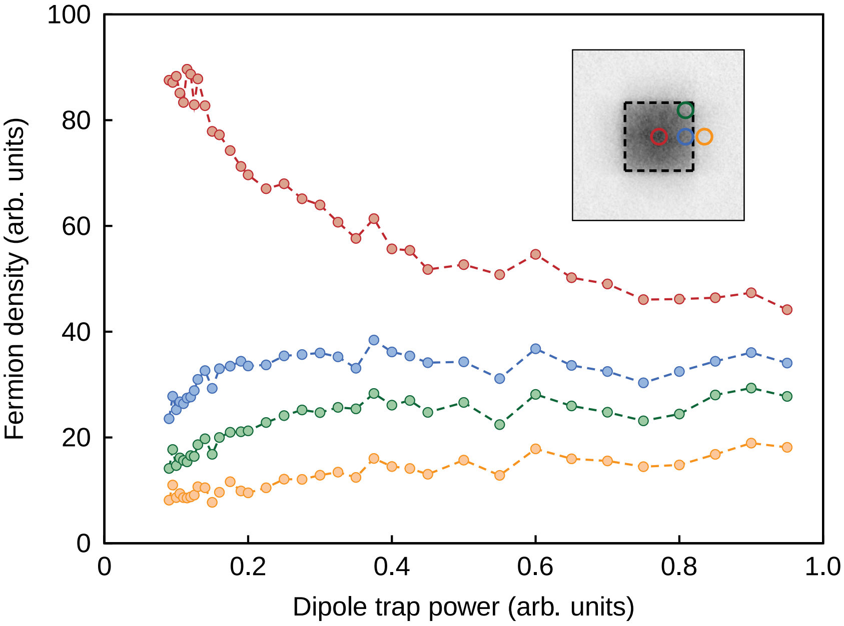

Figure 2.6: Formation of the band-insulating state in the combined optical lattice and external confining potential, measured using a Brillouin zone mapping technique. As the dipole trap is compressed, the center of the first Brillouin zone is depleted (red circles), while the density at the edges and in the corners of the first Brillouin zone increases (blue and green circles, respectively). Saturation occurs at around 45% of the maximum dipole power, indicating the formation of the band insulator. The density in higher Brillouin zones (orange circles) increases smoothly over the whole range of compressions. The inset shows a typical BZM imaging, where the dashed line indicates the extension of the first Brillouin zone. The circles indicate the regions where the individual contributions have been measured.

Instead, it would be desirable to demonstrate the action of Pauli's exclusion principle more directly. If the temperature is low enough that atoms only occupy the lowest band, this amounts to showing that two particles can not have the same quasimomentum. To address this problem, we ask for the probability to detect two fermions at positions x_1 and x_2 in the time-of-flight image. As our images do not show individual particles, but particle densities, this leads us to consider the density-density correlation function

$$G^{(2)}(x_1, x_2) = \langle n(x_1)\, n(x_2)\rangle, \tag{2.15}$$

---

be significantly smaller than 0.5.

or its normalized counterpart

$$g^{(2)}(x_1, x_2) = \frac{\langle n(x_1)\, n(x_2) \rangle}{\langle n(x_1) \rangle \cdot \langle n(x_2) \rangle}. \tag{2.16}$$

For photons, i.e. bosonic particles, this kind of correlation function has been probed in the spectacular Hanbury-Brown and Twiss (HBT) experiment [66, 67, 68]. The probability to find two bosons in coincidence is found to be strongly enhanced at small detector separations. The technique has recently been extended to massive particles, i.e. bosonic atoms [3, 48, 136, 119]. Besides the fundamental interest in the demonstration of this intriguing quantum interference effect, a broad range of applications for the detection of nontrivial quantum many-body states has been suggested in references [3, 102, 124] and many others since. For fermionic particles, one expects to find anticorrelated behaviour in a HBT type experiment, due to Pauli blocking. This is especially intriguing as such anticorrelations can not be explained in a classical theory ($g^{(2)}(x_1 - x_2 = 0) \geq 1$ for any classical field), thus the observation of *antibunching* ($g^{(2)}(x_1 - x_2 = 0) < 1$) is a clear signature of quantum physics at work. However, the effect has been rather elusive so far, mainly due to the fact that most fermionic particles occuring in nature are electrically charged and thus show strong long-range interactions which complicate the observation [70]. Only very recently, evidence for antibunching of free fermions has been found in experiments with thermal neutrons [75]. Starting from an optical lattice, we expect antibunching of particles not only at $x_1 - x_2 = 0$, but also at all distances

$$x_1 - x_2 = \nu\ell \quad \text{with} \quad \ell = \tfrac{2\hbar k}{m}\, t_{\mathrm{TOF}}, \tag{2.17}$$

where ν is an integer number, k is the reciprocal lattice vector and t_{TOF} the time of free flight after release from the lattice potential. This can easily be understood from Pauli's exclusion principle, as all of these positions can be reached by a particle starting from the same Bloch state in the optical lattice. As the Bloch state can only be singly occupied, the detection of a particle at a given position x_1 suppresses the possibility of detecting a second particle at any position $x_2 = x_1 \pm \nu\ell$. This scenario is illustrated in figure 2.7 (c). The detailed behaviour of the density-density correlation function in between the dips predicted by the above argument will depend sensitively on the many-body quantum state in question. This dependence is expected to enable the detection of exotic quantum phases such as an antiferromagnetic [154] or supersolid state [135], although some complications have recently been pointed out [58]. In a first proof of principle experiment, an artificially engineered density wave of bosonic atoms in an optical lattice

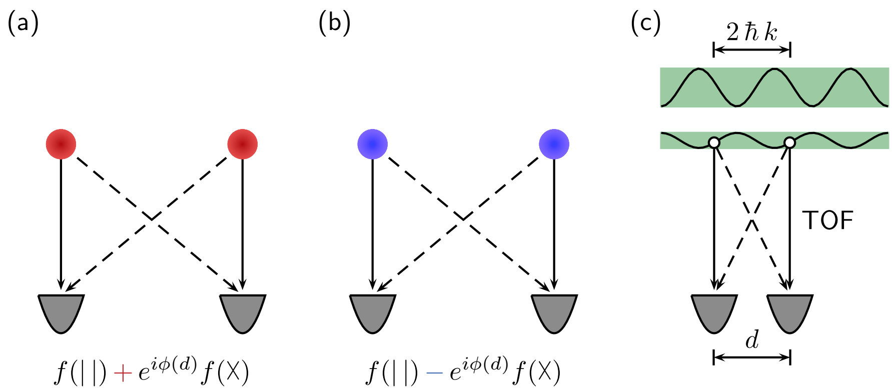

Figure 2.7: Principle of Hanbury-Brown Twiss type experiment. Basic HBT configuration for bosons (a) and fermions (b). The two different pathways to coincident detection are related by the particle exchange operator, leading to an additional minus sign in the case of fermions. (c) HBT experiment starting from an optical lattice. During time of flight, initially different momenta (depicted in the extended zone scheme of the lowest Bloch band of the optical lattice) are converted into spatial distances in real space. This leads us to expect bunching (for bosons) or antibunching (for fermions) at position distances corresponding to integer multiples of $\frac{2\hbar k}{m}\, t_{\mathrm{TOF}}$.

has successfully been detected in a Hanbury-Brown Twiss type correlation analysis experiment [47].

Shot noise correlation analysis

In order to detect the above-mentioned anticorrelations in the experiment, it is important to understand that these occur on the basis of individual detection events and will be washed out for repeated detection events, as the decisions which detector will actually detect the particles, can be considered statistically independent. In the experiment, the detection of an atom is equivalent to the detection of photon scattering by this atom out of the detection laser beam on a CCD camera, provided that photon shot noise can be neglected. The individual pixels of the CCD chip take the role of the detector units in the above discussion. Under typical conditions, each pixel will record on the order of 100 atoms. While the expectation value for the atom number on each pixel can be traced back to the momentum expectation value in the initial trapped state after sufficiently long expansion time[8], the interesting (anti-)correlations are to be searched in the atomic shot noise fluctuations. It is thus clear that there exists a distinct window in which a signal can be detected: On the one hand, the atomic signal must be strong enough to overcome the technical noise level of the camera. On the other hand, if the atom number per pixel becomes too large, the atomic shot noise vanishes within the finite dynamic range of the pixels. Luckily, typical quantum gas experiments are *mesoscopic* just to the right degree to fall into the detection window.

In order to obtain the density-density correlation function from the images, we need to calculate for each TOF image the correlator

$$\begin{aligned} C_\rho(d_x, d_y) &= \langle \rho(x,y) \cdot \rho(x+d_x, y+d_y) \rangle & (2.18) \\ &= \sum_{x,y} n(x,y) \cdot n(x+d_x, y+d_y) & (2.19) \end{aligned}$$

for all distance steps d_x, d_y, where x, y are the row and column index of the CCD camera and $\rho(x,y)$ is the observed optical density signal. Although the above calculation looks straightforward, it is in practice a tedious task, with a computational effort of order $\mathcal{O}(L^4)$, where L is the extension of the image (or the region of interest within it). Fortunately, the correlator can be related to the Fourier power spectrum of the image by means of the Wiener-Khintchine theorem [104], leading to

$$C_\rho(d_x, d_y) = \mathcal{F}^{-1} \left(|\mathcal{F}\left(\rho(x,y)\right)|^2 \right) \tag{2.20}$$

which in turn can be calculated using *Fast Fourier Transform* with effort $\mathcal{O}(L \cdot \log L)$. Finally, the normalization can be obtained from an average over multiple images taken under the same experimental conditions, leading to

$$\tilde{C}_\rho(d_x, d_y) = \frac{\langle C_{\rho_i}(d_x, d_y) \rangle_i}{C_{\langle \rho \rangle_i}(d_x, d_y)}, \tag{2.21}$$

where ρ_i is the optical density of the i-th image, and $\langle \cdot \rangle_i$ denotes the average over all images.

Experimental observation

As the initial state, we prepare a band insulator of fermionic atoms. To this end, we remove all bosonic atoms from the trap at the end of the sympathetic cooling procedure in the dipole trap. The resulting fermion cloud in

---

[8] We assume here that collisions within the sample occuring during time of flight can be neglected, which for a single-component degenerate fermi gas is trivially fulfilled.

these experiments contains around 2.8×10^5 ^{40}K atoms and reaches temperatures down to $T/T_F \approx 0.2$. The band insulator condition can be fulfilled by tuning the compression of the dipole trap, while the atom number is maximized in order to achieve a reasonable signal-to-noise ratio with respect to technical noise sources[9]. The atoms are then adiabatically loaded into a threedimensional optical lattice. The horizontal lattice depth is increased further in order to squeeze the Wannier function, leading to a broader envelope in the time of flight image. The cloud is then released from the optical lattice and imaged along the vertical axis after 10 ms of free expansion. Typically, 200 individual images are recorded for a given set of experimental parameters. After rejection of shots suffering from technical artefacts[10], we are usually left with approximately 70% of the images, which are then subjected to the evaluation procedure outlined above. A typical result of such a measurement is displayed in figure 2.8. At $d_x = d_y = 0$, we find the autocorrelation peak, the width of which gives an estimate of the point spread function of our imaging system [48]. Due to the finite imaging resolution, which in our case is limited both by the numerical aperture of the imaging system and a blurring due to momentum diffusion arising from the recoil momentum of the scattered photons, we can not expect to observe any features narrower than approximately 5.6 μm, corresponding to approximately 1.6 pixels on our CCD chip. The eight dips, which can be observed in a perfectly regular structure centered around the autocorrelation feature, are therefore also broadened far beyond their natural width, due to convolution with the point spread function. Nevertheless, the observed correlation signals $\tilde{C}(d_x, d_y) < 1$ are a clear and unmistakable signature of fermionic antibunching. From the correlator $\tilde{C}(d_x, d_y)$, we can extract the correlation signal strength. To this end, we fit the neighbourhood of the peaks by inverted two-dimensional Gaussians, on top of a linear slope, which locally accounts for the additional structure in the correlator. In a first step, we evaluate three correlators taken at $T/T_F = 0.23(3)$, from which we determine the width and positions of the dip features. Subsequently, all features were fitted fixing these width and position values. The correlation signal amplitude is then given as the average over the four dips corresponding to the principal reciprocal lattice vectors in the horizontal plane. Using this procedure, we can characterize the signal-to-noise ratio as a function of the number of images used in the correlation analysis. In

---

[9] Important noise sources in this context are inhomogenieties and interference fringes in the imaging laser beam, background light and dark counts of the CCD camera.

[10] e. g. interference fringes on the imaging beam, mostly due to intensity or frequency fluctuations in between the signal and reference frame.

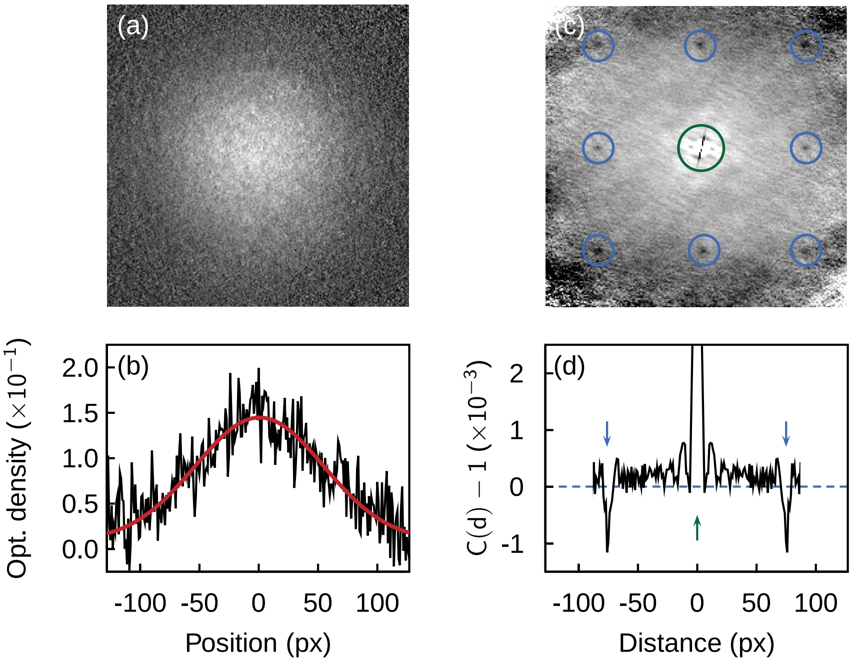

Figure 2.8: Free fermion antibunching. (a) Single absorption image of ^{40}K cloud of about 2.8×10^5 atoms after 10 ms of free expansion, released from a $V_x = 19\,E_r$,$V_y = 21\,E_r$,$V_z = 10\,E_r$ deep lattice. (b) One-dimensional profile through the same picture (black) together with a Gaussian fit (red). (c) Spatial noise correlations obtained from an analysis of 158 independent images, showing an array of eight dips, at the positions corresponding to the reciprocal lattice vectors (marked by blue circles). The additional structures close to the central autocorrelation peak (marked by green circle) are technical artefacts caused by e. g. readout crosstalk of the CCD chip. (d) Horizontal profile through the correlation image. The profile has been high-pass filtered to suppress a broad Gaussian background that we attribute to shot to shot fluctuations in the atom number. Image adapted from reference [131].

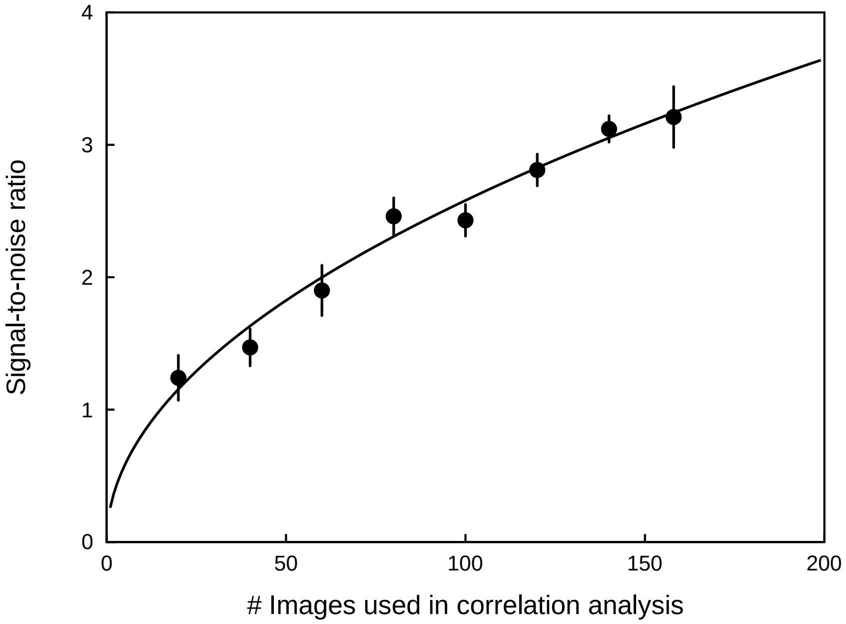

Figure 2.9: Signal-to-noise ratio of the anticorrelation signal, as the number of individual images contributing to the analysis of the correlation function is increased. The line marks the expected square-root behaviour.

figure 2.9, we show the ratio of the fitted correlation signal amplitude to the root-mean-square (RMS) level of the background noise in the vicinity of the dip features. The observed increase of the signal-to-noise ratio with the number of images is consistent with a $1/\sqrt{\#\,\text{images}}$ scaling of the RMS noise under the assumption that the signal amplitude stays constant. We conclude that on the order of 50 images are needed for a reliable fit of the correlations dips, if width, position and amplitude of the features are free parameters.

Temperature dependence of the anticorrelation dips

So far, our arguments have built upon a zero-temperature analysis of the system. However, especially in the case of Fermions, it is of great importance to also consider the influence of finite temperature (and hence finite entropy). For simplicity, we will only consider a one-dimensional model system here, but the basic results can easily be generalized to three dimensions. Our system consists of a finite number N_f of fermionic atoms, which, in addition to the periodic potential by the optical lattice, are subjected to a harmonic confining potential $V_i = \frac{m}{2}\omega^2(\lambda_L/2)^2 i^2$, where the index i

labels individual lattice sites. Furthermore, we assume that both tunneling and the population of higher bands can be neglected. In that case, every lattice site can accomodate at most one atom, and the occupation statistics is described by a Fermi-Dirac distribution of the form

$$f_i(\mu, T) = \frac{1}{1 + \exp\left(\left(\frac{m}{2}\,\omega^2(\lambda_L/2)^2\, i^2 - \mu\right)/k_B T\right)}, \tag{2.22}$$

where μ is the chemical potential, fixed by the implicit condition

$$\sum_i f_i(\mu, T) = N_f. \tag{2.23}$$

Under these assumptions, the system constitutes a *real-space Fermi sea*, which can be characterized by its zero-temperature extension. In analogy to the the Fermi momentum in the case of the usual momentum-space Fermi sea, we define the Fermi radius

$$R_F = \tfrac{1}{2}\, N_f\, \tfrac{\lambda_L}{2}. \tag{2.24}$$

The Fermi radius can be connected to the Fermi temperature in the optical lattice via

$$k_B T_F = \tfrac{m}{2}\,\omega^2 R_F^2. \tag{2.25}$$

At finite temperature, the effective system radius will be larger than R_F, because entropy can only be accomodated by introducing holes in the Fermi sea, while at the same time promoting atoms to energies (and thus positions) outside the zero-temperature Fermi sea, again, in full analogy to the finite temperature softening of band edges in the case of a momentum-space Fermi sea. It should first be pointed out that the quantum-statistical anticorrelations which we expect to see at integer multiples of the distance ℓ should theoretically remain completely unaffected by any change in the system temperature. However, this is not true at distances away from ℓ, and the detailed peak shape will indeed depend on the system size. The finite system size R will reflect itself in oscillations of the momentum correlation which scales as R^{-1}. This oscillatory behaviour is again known from momentum space Fermi seas, where it is also known as *Friedel oscillations* [45]. It can be understood as an instance of *Gibb's phenomenon*[11]. As temperature increases, so will the effective system radius. Therefore, the periodicity

---

[11] Gibb's phenomenon denotes the fact that the Fourier transform of a function which changes non-smoothly at some point, will not converge uniformly, but display a characteristic ripple structure. In our case, the zero-temperature distribution function can be understood as a box-function of dimension $2\,R_F$. It is therefore not surprising that the theoretical shape of the momentum correlation, and thus of our correlation function, should take the form of a sinc function, the periodicity of which scales as R_F^{-1}.

of the real-space Friedel oscillations is expected to decrease, and, most importantly, the central feature will become more narrow. Unfortunately, however, the detailed shape of the correlation signal can not be observed under realistic experimental conditions to date, but is obscured by convolution with the point spread function of the imaging system [47]. Still, this convolution process preserves the signal volume. Therefore, although the theoretical correlation function preserves its amplitude and narrows down its width, the experimentally observable signal will predominantly decrease in amplitude as the temperature increases, the width of the dips staying essentially constant as they are dominated by the finite optical resolution.

In order to observe this temperature dependence, we have prepared the Fermi gas in the dipole trap at different temperatures by varying the end point of the evaporation ramp in the dipole trap. We subsequently ramp the dipole trap back up to the same high compression for all temperatures of the gas. The optical lattices are then ramped up as described before. As the variation of the evaporation ramp causes only little change in the fermion number, the temperature (and thus the entropy carried in the sample) will define the effective width of the cloud in the combined dipole trap and lattice. We take a series of absorption images at each temperature and subsequently perform the correlation analysis. Indeed, we find a decrease of the correlation amplitude with increasing initial temperature, as can be seen in figure 2.10. We currently have no means of independently determining the temperature of the fermions in the optical lattice, therefore all quoted temperatures are measured without the lattice present, by the usual fit of a Fermi-Dirac distribution to the TOF images after release from the dipole trap. We would like to point out that this might give rise to systematic errors, e. g. due to nonadiabaticity of the lattice loading, or a systematic over-estimation of the temperature of the fermionic cloud in the degenerate regime. In particular, these effects might account for the systematic deviation towards stronger signals on the low-temperature side of figure 2.10.

After the completion of this work, antibunching of free ultracold neutral ^{3}He atoms has also been demonstrated with a bulk sample, using a position- and time-sensitive highly efficient single-particle detector based on a microchannel plate [78].

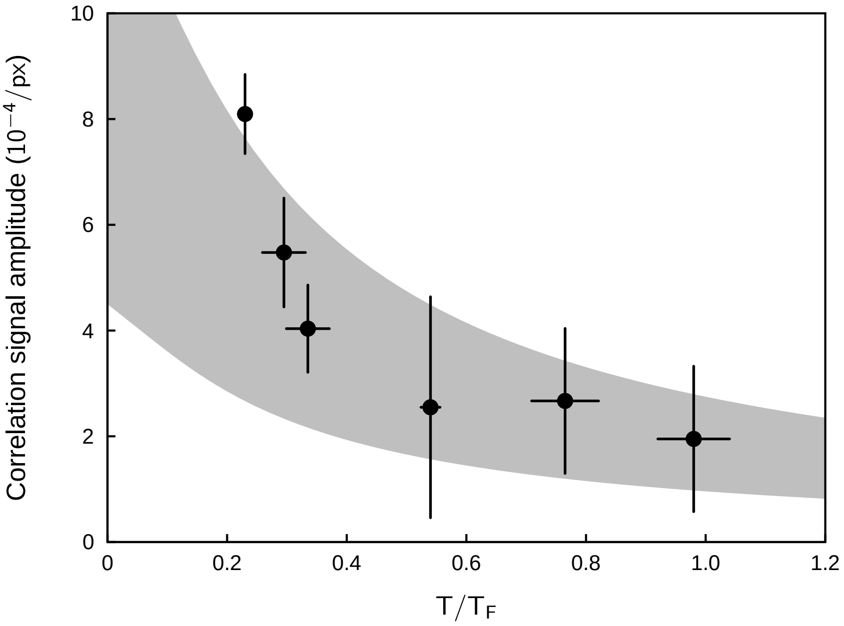

Figure 2.10: Dependence of the HBT antibunching signal strength on the temperature of the fermionic cloud prior to lattice loading. The error bars denote statistical errors of typically four experimental runs, each evaluated independently. The shaded area denotes the theoretical prediction, with the uncertainty stemming mainly from the atom number calibration.

2.5 Heteronuclear long-range molecules

Why molecules in a lattice

In recent years, ultracold molecules have raised increasing interest (see e. g. [88, 80]. *Heteronuclear molecules* made of different atomic species are particularly interesting because their rovibronic ground state features a large permanent electric dipole moment. Polar molecules are useful candidates for precision experiments (see e. g. [90, 74]) and universal quantum computing [34]. If polar molecules can be produced at significant phase space densities, they can form dipolar quantum gases[12]. These dipolar ensembles have properties fundamentally different from usual quantum gases, due to both the relatively long range and the anisotropy of their interactions. The most

---

[12] The only dipolar quantum gases realized so far are made from Chromium atoms, whose high magnetic moment yields an appreciable dipole-dipole coupling, especially when s-wave interactions can be Feshbach-tuned to zero. See reference [91] and references therein for details.

promising scenario for the production of heteronuclear ultracold molecules to date is the controlled association from a binary quantum gas mixture. The stimulated association of heteronuclear molecules from a quantum gas mixture of bosonic Rubidium and fermionic Potassium atoms in the vicinity of a Feshbach resonance has recently been demonstrated in an optical lattice [115] and in a bulk sample [162]. In the latter experiment, vibrational de-excitation of the molecules has been achieved [118, 112]. However, neither of these experiments was able to reach sufficiently high phase space densities to produce a degenerate dipolar gas. Theoretical modelling of the experiments in reference [115] has led to the conclusion that the main limitation in this respect is the initial phase space overlap, while the association process itself, where it takes place, has essentially unit efficiency at sufficiently small molecular binding energies [37]. Conceptually, the formation of heteronuclear molecules in an optical lattice is more promising than in the bulk sample, as it suppresses collisions with residual atoms, which are the major limitation to molecular lifetimes in the existing experiments [161]. Very high conversion efficiencies have been achieved for the formation and de-excitation of *homonuclear* molecules from single-component quantum gases in optical lattices [130, 153, 158]. Motivated by these results, we have conducted some experiments to investigate the formation of heteronuclear molecules in our optical lattice along the lines of the work presented in reference [115], which shall be summarized in the following.

Radio-frequency association near a Feshbach resonance

The method of choice to make heteronuclear molecules near a Feshbach resonance is radio-frequency association, which has been developed in reference [115]. To understand the concept, we need to come back to the *avoided crossing* picture of the Feshbach resonance. The resonance of interest for us occurs between atoms in the hyperfine states $|F = 1, m_F = +1\rangle$ and $|\downarrow\rangle = |F = \frac{9}{2}, m_F = -\frac{9}{2}\rangle$, respectively. Assume that we start with the Potassium atom in the $|\uparrow\rangle = |F = \frac{9}{2}, m_F = -\frac{7}{2}\rangle$ state. In the absence of a Rubidium atom, we can flip the spin of the Potassium atom into the $|\downarrow\rangle$ state by a radio-frequency photon, the energy of which is equal to the Zeeman splitting between the two states. This splitting can be obtained from the Breit-Rabi formula, and corresponds to approximately 80 MHz in the vicinity of our Feshbach resonance. In the presence of the Rubidium atom, the same transition would simply be shifted by the differential interaction energy between the two atoms, if we are far away from any Feshbach resonance. This feature has been extensively used for both fermionic and bosonic atoms in optical lattices (see e. g. [22, 81] in order to detect the presence of more than one atom on a lattice site. If we go closer to the Feshbach resonance, we need to take into consideration the avoided crossing between the closed and the open collisional channel. As a result, it is possible to flip the atomic spin to end up in a state which adiabatically connects to a molecular bound state. For the sake of energy conservation, we now need a blue-shifted radio-frequency photon in order to accomodate the binding energy. It is thus possible to create a long-range molecule from a Rubidium and a Potassium atom by driving the spin flip transition with the correct blue-detuning in the vicinity of the Feshbach-resonance. By recording the transition frequency versus the magnetic field, it is thus possible to map out the eigen-energies of the strongly interacting two-particle system in the optical lattice [115], and confirm the avoided crossing structure. In order to associate molecules in our experiment, we prepare the atoms in a threedimensional optical lattice. It is favourable to work in deep optical lattices in order to protect the resulting molecules from collisions with remaining atoms. The magnetic field is set to a point slightly above the Feshbach resonance[13]. We then use a pulse of radio-frequency radiation to drive the spin-flip transition. By scanning the radio-frequency, we can observe the resonance frequency both for single Potassium atoms and for Potassium atoms sitting together with a Rubidium atom. The results of such an experiment can be seen in figure 2.11, for lattice depths of $V_0 = 30\,\mathrm{E_r}$ and $V_0 = 20\,\mathrm{E_r}$, respectively. The spectra show a clear signature of radio-frequency association of heteronuclear molecules from onsite atom pairs. However, the signal is relatively weak, a fact that can not be fully accounted for by a suppression of coupling (see footnote), which should not yet be very important for the magnetic field chosen. Instead, it is most probably due to a lack of pair sites in the optical lattice in the first place. This is consistent with the strength of the single-atom peak, which still contains the majority of Potassium atoms in the sample. It should be noted that in principle, radio-frequency association should also occur on lattice sites containing a fermion and two or more bosons, albeit at a different

---

[13] It should be noted that while the final state becomes more and more *molecule-like* as one approaches and eventually crosses the free-particle Feshbach resonance, the coupling of the radio-frequency radiation to the transition is continuously suppressed, therefore the efficiency of the process (related to the strength of the spectroscopic signal) is gradually lost [85]. This is mainly due to the recoupling from the atomic to the molecular hyperfine structure. The pathway towards making tightly-bound molecules therefore would include an additional adiabatic magnetic field sweep away from the resonance, once the RF-induced transition to the bound state has taken place.

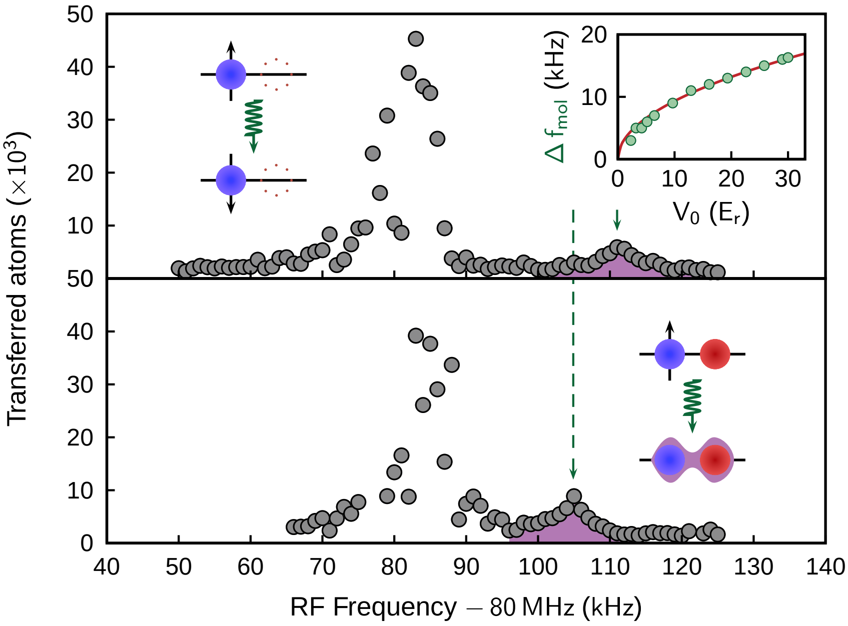

Figure 2.11: Radio-frequency association of molecules at a magnetic field of 546.75 G in a threedimensional optical lattice. Association spectra for lattice depths of $V_0 = 30\,\mathrm{E_r}$ (upper panel) and $V_0 = 20\,\mathrm{E_r}$ (lower panel). The left and right peak correspond to the atomic and molecular signal, respectively. The inset shows the shift of the molecular resonance with increasing depth of the optical lattice (in atomic recoil units), relative to the position observed for vanishing lattice depth. The square root behaviour (red line) can be explained by the differential zero-point energy, as explained in the main text.

detuning, due to the additional interaction energy contributions. We do not expect to observe these processes in the experiment however, due to the expected very short lifetime of these molecules [161]. A second point of interest lies in the clear blue-shift of the observed transition frequency with increasing lattice depth. Experimentally, the shift Δf is found to scale with the lattice depth in recoil units $\tilde{V}_0$ as

$$\Delta f \propto \sqrt{\tilde{V}_0} \tag{2.26}$$

to very high precision, especially for deep lattices. If we assume that in this regime, a harmonic approximation of the lattice wells is valid, this scaling corresponds to a linear increase with the trap frequency. We would like to point out that quite generally for a weakly bound long-range molecule, the molecular AC polarizability is close to the sum of the individual polarizabilities of the atomic constituents. Therefore, we expect the molecules to see an optical lattice of depth $V_0^{(mol)} = V_0^{(1)} + V_0^{(2)}$, where $V_0^{(1,2)}$ are the potential depths experienced by the two atomic species. The trap frequency corresponding to this lattice is given by

$$(\hbar\,\omega_{mol})^2 = 4\,V_0^{(mol)}\,\frac{(\hbar\,k)^2}{2\,M} \tag{2.27}$$

where $M = m_1 + m_2$ is the molecular mass, and the second term is simply the molecular recoil energy. In the case of homonuclear molecules, this leads to $\omega_{mol} = \omega_{atom}$, which has been verified experimentally [130]. In the generic scenario however, we have that $m_{mol} = (1+\beta)\,m_1$, where $\beta = \frac{m_1}{m_2}$ is the mass ratio. Without loss of generality, we assume $m_1 \leq m_2$, and thus $\beta \leq 1$. The magic wavelength condition $\tilde{V}_0^{(1)} = \tilde{V}_0^{(2)} = \tilde{V}_0^{(atoms)}$, can be expressed as $\alpha_1(\lambda^{(*)})\,m_1 = \alpha_2(\lambda^{(*)})\,m_2$, where $\alpha_{1,2}(\lambda^{(*)})$ are the respective AC polarizabilities, and $\lambda^{(*)}$ is the magic wavelength. This yields a molecular potential depth

$$V_0^{(mol)} \propto \alpha_1 + \alpha_2 = \alpha_1\,\cdot(1+\beta) = (1+\beta)\,V_0^{(1)}, \tag{2.28}$$

and, by normalizing to recoil units

$$\tilde{V}_0^{(mol)} \propto M\,(1+\beta)\,\tilde{V}_0^{(atoms)}. \tag{2.29}$$

Comparing to the atomic case, we find

$$\tilde{V}_0^{(mol)} = \frac{M}{\mu}\,\tilde{V}_0^{(1)} = \frac{M}{\mu}\,\tilde{V}_0^{(2)}, \tag{2.30}$$

where μ is the reduced mass of the pair. For the case of interest here, $\frac{M}{\mu} \approx 4.6$, which means that the molecule sees a significantly deeper potential than the individual atoms, and for all practical purposes, can always be considered immobile. Evaluation of equation 2.28 yields that the trap frequencies of molecules and atoms are related by

$$\omega_{mol} = \sqrt{1+\beta}\,\omega_{(1)} = \sqrt{1+\tfrac{1}{\beta}}\,\omega_{(2)}. \tag{2.31}$$

The zero point energy of two atoms is given approximately by $\frac{\hbar}{2}\,(\omega_{(1)} + \omega_{(2)})$. We therefore find a differential zero point energy between atoms and molecules of

$$\Delta\,\epsilon_0 = \tfrac{\hbar}{2}\,\omega_{(1)}\,\underbrace{(1+\sqrt{\beta}-\sqrt{1+\beta})}_{\gamma}, \tag{2.32}$$

with the numerical factor $\gamma \approx 0.47$ for our mixture, comparing to an experimentally observed value of $\gamma \approx 0.50$. We therefore interpret the shift displayed in the inset of figure 2.11 as the differential zero point energy between atoms and molecules. The residual discrepancy with the experimentally observed scaling of the binding energies will be partly due to inaccuracies of the approximations underlying our simple model, but mostly to the neglect of interactions in the initial two-particle state and the shifting of the Feshbach-resonance position in the optical lattice. The good overall agreement with our model confirms that the molecules are in fact produced in the lowest band of a deep optical lattice.

Molecule lifetime

We have also investigated the lifetime of the heteronuclear molecules formed via radio-frequency association. To this end, we include an additional hold-time in between the association pulse and the detection. During this time, the molecules can decay, both radiatively via the absorption of photons from the lattice or dipole trap beams, or via collisions with remaining atoms or other molecules. In bulk experiments, collisions with residual atoms have been identified as the most important loss channel [161]. Previous experiments in optical lattices observed molecular lifetimes on the order of few milliseconds, which was significantly reduced as the molecules were produced with increasing binding energies [115]. Our lifetime measurements on even more strongly bound molecules, which are displayed in figure 2.12, are consistent with these findings. The order of magnitude of the observed lifetimes is consistent with the residual tunneling rates for atoms at the given lattice depth ($1/(6\,J_f) \approx 2.6\,\mathrm{ms}$ and $1/(6\,J_b) \approx 5.6\,\mathrm{ms}$). We have compared lifetimes with and without the presence of the dipole trap and found no significant difference. We therefore conclude that far off-resonant radiative stimulation is not an important decay channel, in agreement with previous observations. We currently have no means to directly measure the influence of lattice light on the lifetime; still, there is strong evidence that collisions with remaining atoms can account for most of the loss processes.

Efficiency considerations

To date, most experiments on ultracold heteronuclear molecules are severely limited by the production efficiency of the molecules. Unlike in the case of homonuclear molecules made from bosonic atoms, where in a 3D optical lattice, the initial state can relatively easily be tailored such that most lattice sites are occupied by exactly two atoms and the molecule production efficiency solely depends on the adiabaticity of the actual association pro-

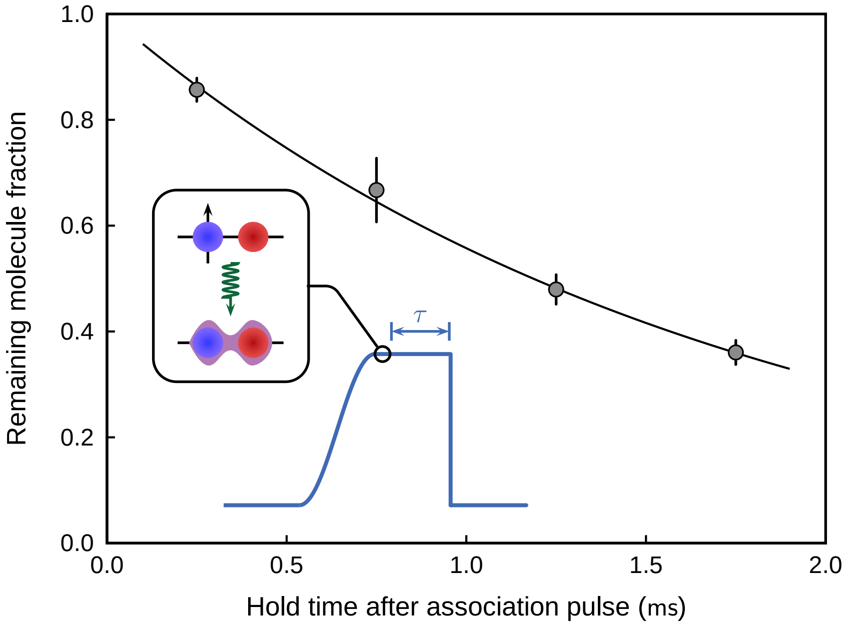

Figure 2.12: Lifetime of heteronuclear molecules in a deep ($V_0 = 30\,\mathrm{E_r}$) optical lattice, without removal of remaining atoms. The inset shows the experimental sequence used for this measurement.

cess (see e. g. [130, 42]), the efficient production of heteronuclear molecules also requires a procedure to prepare the non-trivial initial state with one atom per species on each lattice site. As we do not have a handle in the experiment to manipulate the atom numbers on individual sites, the easiest way to influence the production efficiency of molecules is via the mean filling of lattice sites. One obvious way to influence this builds upon compression of the dipole trap before loading the atoms into the optical lattice. The experimental result, which is shown in figure 2.13 (a), displays an optimum compression, presumably coinciding with a maximum amount of pair sites. We have also investigated the dependence on the rampup timescale for the 3D optical lattice. As can be seen in figure 2.13 (b), there again exists an optimum, which clearly corresponds to slightly non-adiabatic loading. This might be due to the fact that the relatively strong background interspecies attraction in the initial state during the lattice loading gives rise to higher boson numbers on lattice sites occupied by fermions, i. e. occupation by two or more bosons, such that the radio-frequency association process is no longer resonant, or the lifetime of the resulting molecule vanishes due to the presence of an additional particle on the same lattice site. In conclusion, the experiments reported in this section indicate that albeit possible, radio-

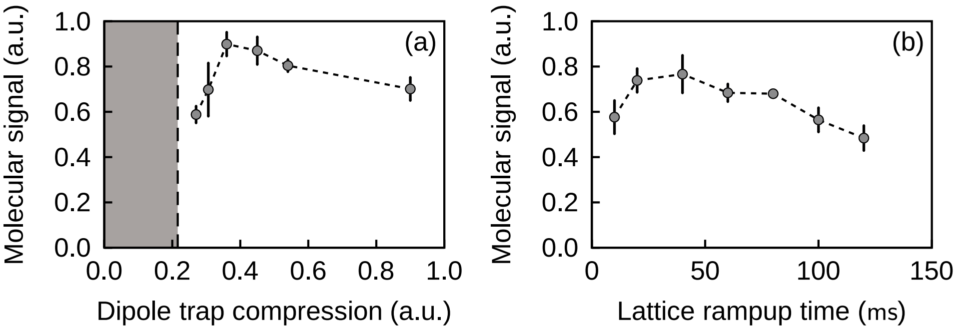

Figure 2.13: Efficiency of radiofrequency association in an optical lattice. (a) Amplitude of molecular signal versus compression of the dipole trap. The shaded area on the left hand side indicates the regime where the dipole trap is not strong enough to hold both species against gravity. The dashed vertical line indicates the point at which ^{87}Rb atoms are lost from the trap. (b) Amplitude of molecular signal versus time scale for the rampup of the optical lattice potential. The optimum efficiency clearly corresponds to non-adiabatic lattice loading.

frequency association in our optical lattice setup is not efficient enough to allow for further experiments on the heteronuclear molecules. This lack of efficiency is probably due to the number statistics inside the optical lattice, and can in principle be dealt with by tailoring of the initial state. However, the possible gain observed so far using straightforward manipulation techniques is relatively poor.

Three

Physics of Bose-Fermi Hubbard systems

In this chapter, we present the Hubbard model for interacting quantum gases in optical lattices. We discuss the self-consistency condition on the onsite wavefunctions and the consequences in terms of renormalization of the effective Hubbard model. Finally, we give an overview of existing theoretical approaches and their predictions for the many-body physics of the Bose-Fermi Hubbard model.

3.1 The Wannier picture and Hubbard's model

Tight binding and the Wannier picture

In situations, where local effects are to be described, Bloch waves are not very convenient to work with. A more natural description arises when we consider the periodic potential as a regular array of micro-wells, each of which can support a progression of bound states. These so-called Wannier states are spatially localized on individual lattice sites and thus naturally lend themselves to describing local physics. They are related to the Bloch states considered earlier via the Fourier transform:

$$w(x - x_i) = \sum_q e^{i\,q\,x_i} \cdot u_q(x) \tag{3.1}$$

where x_i denotes the position of the specific potential well, and we have restricted ourselves to the first Bloch band for simplicity. Figure 3.1 (a) shows Wannier functions obtained from the single-particle band structure, for increasingly deep optical lattices. It should be noted that as the potential depth is increased, the individual potential wells can be approximated with increasing accuracy by a harmonic potential. Therefore, the Wannier functions tend towards a Gaussian shape. However, it should be noted that the numerical accuracy of this description is poor apart from the case of extremely deep lattices, especially in the wings of the density profile. Figure 3.1 (b) compares the width of the harmonically approximated wave functions with the width of the real Wannier functions[1]. We have also included measurements of the envelope of the time of flight pattern, which, if rescaled accordingly, correspond surprisingly well to the inverse of the Wannier widths.

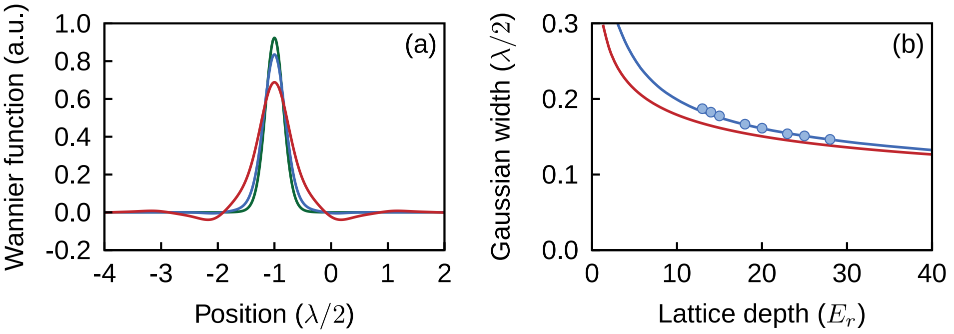

Figure 3.1: Wannier functions. (a) Theoretical single-particle Wannier functions for lattice depth of 3 (red), 10 (blue) and 20 E_r (green curve), showing the trend to an asymptotic Gaussian as $\tilde{V}_0 \to \infty$. (b) Width of Wannier functions, in units of the lattice period. The red curve denotes the oscillator length of the Gaussian ground state in the harmonic approximation. This can be compared to Gaussian fits to the real single-particle Wannier functions (blue curve), which agree with measured data of $\gamma\,\sigma^{-1}$ (blue points), where σ is the envelope width after TOF and γ is a prefactor accounting for the time of flight expansion.

Hubbard's model

In 1963, Hubbard [73] came up with a conceptually very simple model for the behaviour of electrons in the conduction band of transition metal oxide crystals, building on ideas by Mott [110]. Empirically, it had been discovered [33] that these materials were rather good insulators, although their

---

[1] The Wannier width was extracted using Gaussian fits.

band structure had led people to expect a conductor. The basic idea behind Hubbard's model, is that the electrons in these materials could best be described in a Wannier basis of orbitals well localized at the positions of the individual ions. Within each orbital, the strong repulsive interaction between electrons of opposite spin needs to be taken into account[2]. Electrons within the material can propagate by hopping from one ion to the next, however, this process can be strongly suppressed if the destination site is already occupied by another electron of opposite spin. This way, the mobility of electrons vanishes at half filling of the band, giving rise to insulating behaviour of the material, whereas a normal band insulator would only be formed at filling one. Hubbard's model has received a lot of attention over the years, and can be considered a *generic* model for strongly correlated interacting many-particle systems. Formally, the model Hamiltonian is given by:

$$H = -J \sum_{\langle i,j \rangle,\sigma} a^{\dagger}_{i,\sigma} a_{j,\sigma} + U \sum_{i} n_{i,\uparrow} n_{i,\downarrow} \tag{3.2}$$

where $a^{\dagger}_{i,\sigma}$ ($a_{i,\sigma}$) is the operator for creating (annihilating) an electron of spin $\sigma = \uparrow, \downarrow$ at site i, and $n_{i,\sigma}$ are the corresponding number operators, J is the amplitude for hopping between adjacent sites, U is the on-site interaction energy between two electrons, and the summation index $\langle i, j \rangle$ is assumed to run over all next-neighbour sites.

In 1989, Fisher was able to show that the bosonic analogon of the Hubbard model at integer filling $\bar{n}_b$ features a quantum phase transition between a conducting and an insulating state, based on the interplay between tunneling and interaction [46]. The phase diagram of the model is governed by the ratio $U/(z\,J)$, and the critical value at which the phase transition occurs depends solely on the coordination number z for the geometry in question.

The Bose-Fermi Hubbard model in optical lattices

In 1998, Jaksch and coworkers pointed out that something similar to the Hubbard model could indeed be realized with ultracold atoms in optical lattices [77]. As the only ultracold gases available by that time were bosonic, this quickly led to an experimental realization of the Bose-Hubbard model [46] and the observation of the corresponding superfluid to Mott insulator transition [60]. Both static and dynamic properties of this model have been

---

[2] The Coulomb interaction between electrons is in general not long-ranged inside a material, due to shielding, therefore, interactions between electrons in orbitals located at different sites can be neglected.

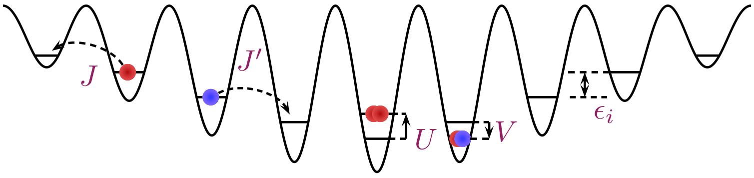

Figure 3.2: Physical meaning of the control parameters of the Bose-Fermi-Hubbard model in the presence of an external confining potential. Bosonic and fermionic atoms are depicted in red and blue, respectively.

studied in great detail since (see e. g. reference [14] for a recent review). Very recently, a fermionic Hubbard model could finally be realized in a balanced mixture of the two lowermost spin states of ultracold ^{40}K atoms [81, 138].

The Hubbard Hamiltonian can easily be generalized to describe mixtures of quantum gases. For the case of interest in this work, namely a mixture of bosons and spinpolarized fermions, the corresponding Bose-Fermi-Hubbard Hamiltonian takes the form

$$\begin{aligned} H = & - J \sum_{\langle i,j \rangle} a_i^\dagger a_j - J' \sum_{\langle i,j \rangle} c_i^\dagger c_j \\ & + \frac{U_{bb}}{2} \sum_i n_{b,i} \left(n_{b,i} - 1 \right) + V_{bf} \sum_i n_{b,i}\, n_{f,i} \\ & + \sum_i \epsilon_i\, n_{b,i} + \sum_i \epsilon_i' n_{f,i} \end{aligned} \tag{3.3}$$

Here, a_i, $a_i^\dagger$ and c_i, $c_i^\dagger$ are the annihilation and creation operators at lattice site i for bosons and fermions, respectively, and $n_{b,i}$ and $n_{f,i}$ are the corresponding number operators. We shall now discuss the control parameters of the model, which are visualized in figure 3.2.

- J and J' denote the tunneling amplitude of bosons and fermions respectively, where tunneling is understood to happen between adjacent sites only. In the limits $J \ll J'$ or $J \gg J'$, which can be realized by tuning the wavelength of the optical lattice, one species is mobile while the other one is frozen out. In such a situation, it is possible to come up with effective models for the remaining mobile species. However, in the context of the experiments reported in this work, we always have $J/J' \sim \mathcal{O}(1)$. More specifically, for the magic wavelength identified in section 2.1, J/J' is given by the mass ratio of the two species.

- U_{bb} is the on-site interaction energy of two bosons. If more than two bosons are present on one side, the total interaction energy is assumed to be the single-pair energy times the number of pairs, which is $n_b \cdot (n_b - 1)/2$ [3]. Generally, we will have $U_{bb} > 0$, i. e. repulsion between the bosons, as attractively interacting BEC above a very small particle number are instable with respect to a mean field induced collapse [128].

- V_{bf} is the strength of the interspecies interaction, which can be both repulsive or attractive. Unlike the interboson repulsion, this term is linear in the boson occupation number n_b, it should therefore be absorbed in a global energy offset if all sites available to the bosons are filled with a fermion.

- Note the absence of an interfermion interaction term. This lack of symmetry stems from the Pauli exclusion principle, which in this spin-polarized scenario does not allow two fermions to occupy the same site and interact.

- ϵ_i and ϵ'_i denote a site-specific energy offset for the bosons and fermions, respectively. These terms may account for disorder on top of the periodic potential [46]. However, in the present case, we only need to deal with the large-scale inhomogeneity introduced into the system by the presence of an overall confining potential, and therefore $\epsilon_i \sim i^2$. Due to a convenient separation of energy scales, it is often possible to ignore these terms altogether[4].

Relating Hubbard Parameters with Wannier functions

In order to apply Hubbard-type models to quantum gases in optical lattice, we have to clarify the relationship between the parameters J, J', U_{bb} and V_{bf} on the one hand, and the microscopic properties of the ultracold atoms on the other hand. The main arguments here go back to Jaksch [77] and Dickerscheid [39]. Assuming that we know the Wannier functions Φ_b and Φ_f for a boson or a fermion respectively, we can define the amplitude for a

---

[3] With experiments similar to the ones described in the following chapter, it is actually quite easy to observe the breakdown of this assumption. See [155, 157] for details.

[4] It should be noted though that these terms are absolutely crucial in allowing the observation of Mott-insulating behaviour at incommensurate filling, by the formation of the so called *shell structure* [77].

tunneling event between adjacent sites as the matrix element

$$J_{i,k} = \int \Phi_b(x - x_i)\, H_{L,b}\, \Phi_b(x - x_j) dV \tag{3.4}$$

and

$$J'_{i,k} = \int \Phi_f(x - x_i)\, H_{L,f}\, \Phi_f(x - x_j) dV\,. \tag{3.5}$$

Often, the definition

$$J = \tfrac{1}{4} D_b = \tfrac{1}{4} |\epsilon_b(0) - \epsilon_b(\hbar \frac{2\,\pi}{\lambda})| \tag{3.6}$$

and an analogous relation for the fermions are used instead (and will be used throughout this work). The two definitions are not strictly equivalent, as the latter also incorporates tunneling processes over arbitrary distances, however, the difference is negligible for practical purposes. Due to the short range of molecular potentials as compared to the optical wavelength, the interaction energy can be treated in using a Fermi contact pseudopotential approximation, leading to the expressions

$$U_{bb} = \frac{2\, a_{bb}\, h}{m_b} \int |\Phi_b|^4 dV \tag{3.7}$$

and

$$V_{bf} = \frac{4\, a_{bf}\, h}{\mu_{bf}} \int |\Phi_b|^2 \cdot |\Phi_f|^2 dV \tag{3.8}$$

for intraspecies and interspecies interaction, respectively, where $\mu_{bf} = \frac{m_b\, m_f}{m_b + m_f}$ is the reduced mass of the boson-fermion-pair, and a_{bb} and a_{bf} are the corresponding s-wave scattering length. In the course of this work, $a_{bb} \approx +100\, a_0$ is fixed, while a_{bf} is tunable with the help of the interspecies Feshbach resonance presented in section 1.5. It has been pointed out that the accurate microscopic description of atoms interacting in the vicinity of a Feshbach resonance is highly nontrivial in an optical lattice, especially for atoms with different masses, where a coupling between center-of-mass and relative motion occurs. Nevertheless, as long as molecule formation can be neglected, it is always possible to work in an effective interaction framework where such complications do not matter [38, 40]. For deep optical lattices, the overlap integrals can be approximated as Gaussian integrals, yielding a scaling

$$U_{bb}, V_{bf} \sim V_0^{3/4}. \tag{3.9}$$

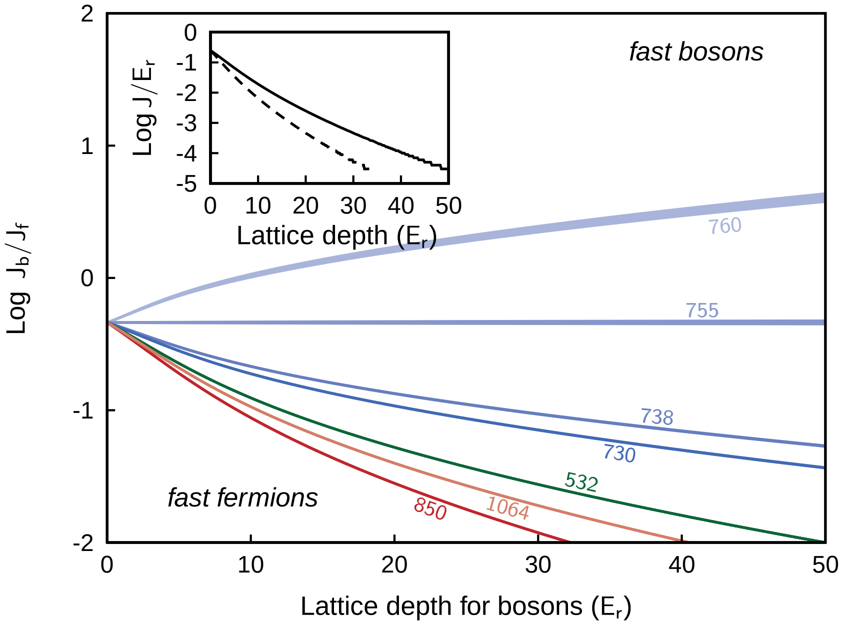

Figure 3.3: Tunneling strength in an optical lattice potential. The ratio between the boson and fermion tunneling rates is affected both by the potential depth V_0 in recoil units experienced by the two species, and thus by their AC polarizabilities, as discussed in the previous chapter, and by the mass ratio. The blue curves correspond to lattice wavelengths of 760 nm, 755 nm, 738 nm and 730 nm (from top to bottom), thus covering the practically accessible range of blue-detuned lattice wavelength derived from our Ti:Saphire laser. For comparison, we have also included curves corresponding to lattices at wavelengths of 850 nm, 1064 nm and 532 nm (dark red, faint red and green curve, respectively). Most theory predictions on the mixture are valid in the limit of fast fermions only. The inset displays the universal scaling relation between the normalized tunneling amplitude and potential depth (solid line). The dashed line in the inset indicates the corresponding tunneling amplitude for a lattice depth reduced by a factor of 2/3. It can be seen, that at any given fixed ratio of lattice depths for the two species (i. e. at a fixed wavelength) the tunneling ratio increases strongly for increasingly deep lattices.

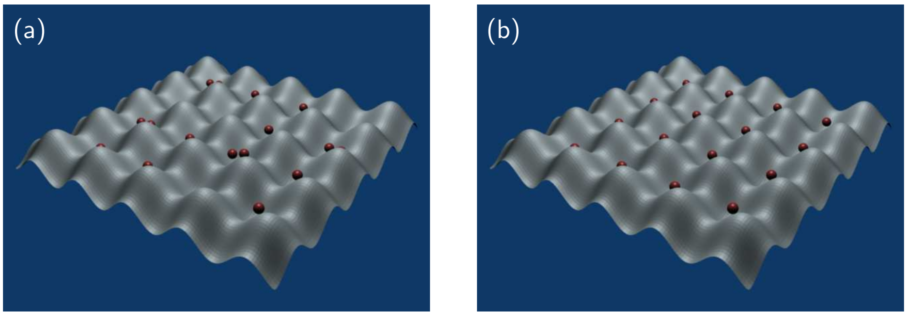

Figure 3.4: Limiting cases of the pure bosonic Hubbard model. (a) In the non-interacting limit $\frac{U}{J} \ll 1$, the system is superfluid, with a coherent state on every lattice site. (b) In the zero-tunneling limit $\frac{U}{J} \to \infty$, a Mott insulator is formed, with a well defined integer occupation on all sites.

The bosonic superfluid to Mott insulator transition

The Bose-Hubbard model can be thought of as the limiting case of the Bose-Fermi-Hubbard model both for a vanishing Fermion number or for a vanishing interspecies interaction. The quantum phase transition between the bosonic superfluid and the Mott insulator has been demonstrated in threedimensional [60] and twodimensional [141, 142] optical lattices. For $J_b \gg U_{bb}$, we recover the superfluid macroscopic matter wave described earlier, i. e. a Poissonian probability distribution of lattice site occupation, and a well-defined macroscopic phase. On the other hand, if $U_{bb} \gg J_b$, we find a well-defined site occupation, depending on the atom number and the external confinement potential. The phase coherence in the system is lost, the system turns into a bosonic Mott insulator. These two limiting cases of Bose-Hubbard physics are depicted schematically in figure 3.4. The critical ratio U_{bb}/J_b can be calculated within a mean-field approximation [151], yielding

$$(U_{bb}/z\, J_b)_c \approx 2\,\bar{n}_b + 1 + \sqrt{(2\,\bar{n}_b + 1)^2 - 1}, \tag{3.10}$$

which amounts to $(U_{bb}/J_b)_c \approx 35$ for the simple cubic threedimensional case ($z = 6$) with unity filling. A more accurate value of $(U_{bb}/J_b)_c \approx 29.3$ has recently been found for the case $z = 6$ using a Quantum Monte Carlo treatment [24]. Experimentally, the ratio U_{bb}/J_b can be translated into a depth V_0 of the optical lattice potential, given the scaling implied by the inset of figure 3.3 and equation 3.9, respectively. The experimental sequence for the observation of the superfluid to Mott insulator quantum phase transition therefore typically relies on adiabatically changing $U_b b/J_b$ by slowly increasing the depth of the optical lattice potential. A similar procedure is also followed in this work, and the phase transition is thereby associated with a critical lattice depth V_0^{crit}.

3.2 Self-consistent Wannier functions

Interactions and self-consistency

The considerations in the previous sections are only accurate within the single-band approximation, i. e. they are valid as long as the interaction energies V_{bf}, U_{bb} satisfy

$$\frac{|V_{bf}|}{\Delta}, \frac{U_{bb}}{\Delta} \ll 1, \tag{3.11}$$

where Δ is the bandgap. However, the interaction energies are by no means a small perturbation in practice. Instead, they can reach a significant fraction of the band gap. Therefore, the Wannier wavefunctions of the interacting ground state are different from the single-particle ground state wave functions, and admixtures from higher Bloch bands are necessary to describe it. In the case of repulsive interactions, we might be tempted to stop at this point and content ourselves with leading-order perturbative corrections to the Wannier orbitals, as we expect the orbitals to broaden, whereby the onsite density overlap and thus the interaction energy contribution are reduced. In the case of attractive interactions however, the corrected orbitals will give rise to higher onsite density overlap, resulting in stronger interactions. Therefore, the correction can only be applied iteratively, until convergence is reached. The resulting orbitals, which can be regarded as eigenfunctions of the full interacting Hamiltonian, are commonly termed *self-consistent*. In a sense, self-consistent orbitals are the natural basis for the investigation of strongly correlated many-body systems, where properties of individual constituents are no longer defined independently from the surrounding particles. In the following, we will investigate the modification of the Wannier wavefunctions from single-particle to self-consistent orbitals, and the consequences of this effect for the Hubbard-type many-body quantum system.

A variational estimate

In order to understand the consequences of the modification of Wannier functions by interactions, we investigate a simple model system, which can be treated analytically. In the limit of infinitely deep lattices, the lattice sites are effectively isolated harmonic potential wells, and the Wannier functions in the lowest Bloch band are the ground state wave functions of these harmonic wells, i. e. take the form:

$$\Phi(\mathbf{r}) = \frac{1}{\mathcal{N}}\, e^{-\alpha\, r^2/2} \tag{3.12}$$

where $\frac{1}{\mathcal{N}}$ is a suitable normalization constant, i. e. $\mathcal{N} = \left(\frac{\pi}{\alpha}\right)^{3/2}$ for one particle per well. For noninteracting particles, we know that $\alpha = {\sigma_0}^{-2}$, where

$$\sigma_0 = \sqrt{\frac{\hbar}{m\,\omega}} \tag{3.13}$$

is the usual oscillator length, for a harmonic oscillator of frequency $\omega/(2\,\pi)$ for a particle of mass m. We expect an attractive interparticle interaction to narrow the width of the wave function, while repulsion will broaden it. This leads us to the formulation of a variational[5] Wannier wavefunction, for the energy functional

$$\begin{aligned} E[\Phi_b, \Phi_f, n_B, n_F] = n_B & \left(\langle T_b \rangle + \frac{1}{2}\, m_b\, \omega_b^2 \langle r_b^2 \rangle \right) \\ & + n_f \left(\langle T_f \rangle + \frac{1}{2}\, m_f\, \omega_f^2 \langle r_f^2 \rangle \right) \\ & + \frac{n_b(n_b - 1)}{2}\, \langle U_{bb} \rangle + n_b\, n_f\, \langle V_{bf} \rangle, \end{aligned} \tag{3.14}$$

where $\Phi_{b,f}$ are the test wave functions for bosons and fermions respectively, for positive integers n_b and $n_f \in \{0, 1\}$ are the atom numbers within the well, $m_{b,f}$ the corresponding masses, and $\omega_{b,f}/(2\,\pi)$ the respective trap frequencies. As motivated above, we use Gaussian test functions, with independent dimensionless variational parameters

$$\beta_{b,f} = \frac{\sigma_{b,f}\, \sqrt{m_{b,f}\, \omega_{m,f}}}{\sqrt{\hbar}}. \tag{3.15}$$

The kinetic energy takes the usual form

$$\langle T_{b,f} \rangle = -\frac{\hbar^2}{2\, m_{b,f}} \int \Phi^*_{b,f} \nabla^2_{b,f} \Phi_{b,f} d^3\mathbf{r} = \frac{\hbar^2}{2\, m_{b,f}} \int (\nabla_{b,f} \Phi_{b,f})^2 d^3\mathbf{r}, \tag{3.16}$$

---

[5] It is not a priori clear that the variational approach yields a reasonable approximation to the shape of ground state Wannier orbitals. Kohn [89] has shown that for suitably chosen test functions, this is indeed the case.

where we have used integration by parts and assumed that the test wave functions are real-valued. U_{bb} and V_{bf} are given by formulae 3.7 and 3.8, respectively. Clearly, all integrals occuring in the evaluation of the functional 3.14 on Gaussian test functions can be brought into the form

$$\int_{-\infty}^{\infty} z^{\nu}\, e^{-z^2}\, dz = \Gamma\left(\frac{1+\nu}{2}\right), \tag{3.17}$$

which allows us to calculate the total energy

$$\begin{aligned} E_{tot}[\beta_b, \beta_f] = \frac{3}{4}\left(\frac{n_b}{\beta_b^2}\,\hbar\,\omega_b + \frac{n_f}{\beta_f^2}\,\hbar\,\omega_f + n_b\,\beta_b^2\,\hbar\,\omega_b + n_f\,\beta_f^2\,\hbar\,\omega_f\right) \\ + \frac{n_b\,(n_b-1)}{2}\cdot\frac{2\sqrt{2}}{\sqrt{\pi}}\cdot\frac{1}{\beta_b^3}\cdot\frac{a_{bb}}{\sigma_{0,b}}\,\hbar\,\omega_b \\ + n_b\,n_f\cdot\frac{4\sqrt{2}}{\sqrt{\pi}}\cdot\frac{1}{(\beta_b^2+\chi\,\beta_f^2)^{3/2}}\cdot\frac{a_{bf}}{\xi\,\sigma_{0,b}}\,\hbar\,\omega_b, \end{aligned} \tag{3.18}$$

where $\chi = \frac{\sigma_{0,f}^2}{\sigma_{0,b}^2}$ and $\xi = \frac{m_f}{m_b+m_f}$. At our magic wavelength, this is further simplified, as $\chi = 1$. By the variational principle [134], we have to find a minimum of functional 3.18 in order to estimate the ground state energy of the system. Figure 3.5 shows the energy landscape for one boson coexisting with a fermion on a lattice site of depth $V_{0;b,f} = 12\,E_r$ at the background interspecies scattering length $a_{bf} = -185\,a_0$. The energy minimum is found using a standard optimization algorithm[6]. We can vary the interspecies interaction strength, and obtain Wannier functions whose width depends on the interaction strength, see figure 3.6.

Onsite-collapse and enhancement of three-body losses

From the results presented in figure 3.6, we find that for any reasonable boson number, there exists a critical interspecies attractive scattering length beyond which the onsite density collapses. At this point, one might argue that the model clearly becomes invalid. Nevertheless, the collapse can be considered physical for more than two particles per site, as the tremendous increase in onsite density in the vicinity of the collapse will give rise to enhanced three-body losses. Similar behaviour has been observed in a macroscopic harmonic trap [108, 117, 10, 9], and can be considered a generalization of the well-known *bose-nova* effect [128].

---

[6] Downhill-Simplex minimization as implemented in the SciPy library, www.scipy.org.

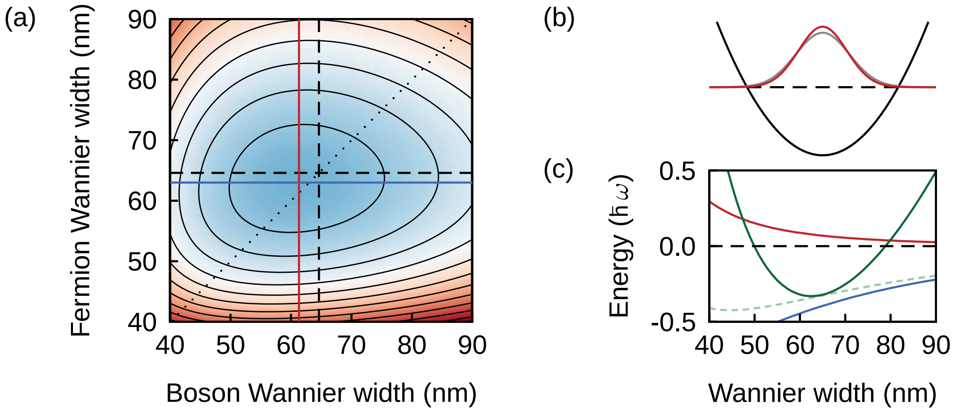

Figure 3.5: Minimization of the total energy. (a) Energy landscapes for one fermion interacting via the background scattering length $a_{bf} = -185\,a_0$, with a single boson in an optical lattice at a wavelength of 755.5 nm and at a lattice depth of $12\,E_r$. The Wannier function corresponding to the new minimum of the total onsite energy (crossing of red and blue line) is squeezed together with respect to the single-particle state characterized by the oscillator length (dashed lines) in the harmonic approximation. The dotted line indicates the *magic* relation $\sigma_b = \sigma_f$. (b) Associated modification of the bosonic Wannier orbital in the harmonic approximation (red curve), as compared to the single-particle orbital (grey curve). (c) Energy change with varying width of the bosonic wavefunction, for a site with two bosons and one fermion. The fermionic orbital is kept fixed at the optimum value. The red and blue curve show the energy contributions of the inter-boson and interspecies interaction, respectively. The dashed green curve indicates the sum of all interaction contributions. The green curve yields the change in total energy, as compared to the energy of the non-interacting three-particle ground state. All energies are given in units of the bosonic trap frequency.

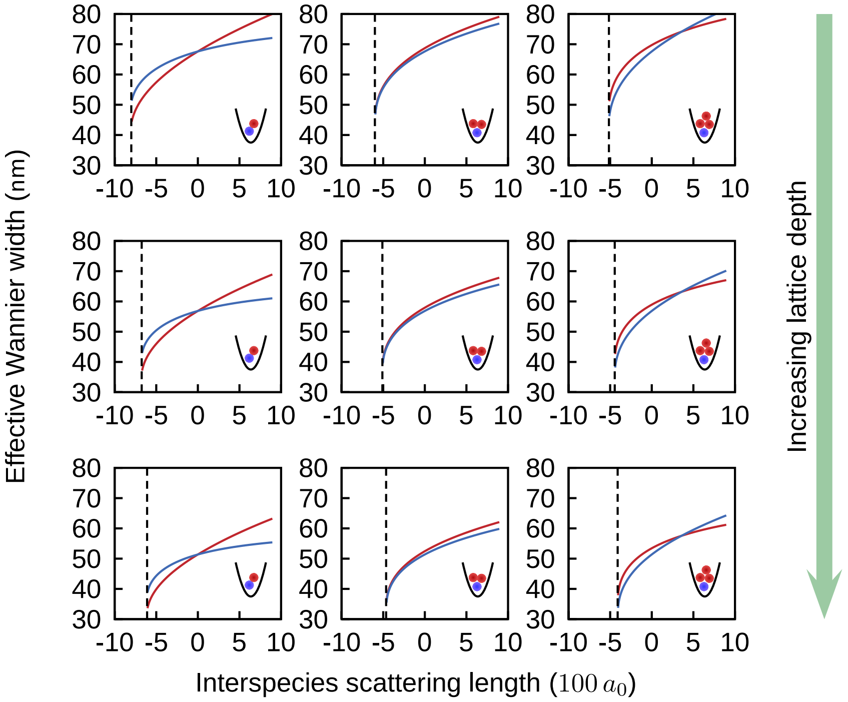

Figure 3.6: Wannier width for bosons (red) and fermions (blue) at lattice depths of 10, 20 and 30 E_r (from top to bottom row) versus interspecies scattering length a_{bf}, for one, two and three bosons (from left to right column) coexisting with one fermion. Beyond a critical scattering length indicated by the dashed vertical lines, there exists no minimum of the energy functional at any finite width of the Wannier functions. Physically, for more than two particles on a site, this is expected to result in a collapse of the onsite density.

Renormalization of interaction energies

The most important consequence of the appearance of self-consistent Wannier functions is the resulting energy change. At a first glance, one might be tempted to redefine the interaction energy of the system in analogy to the naive single-band Hubbard case, i. e. for species x and y, we would have

$$V_{xy} = \frac{4\,\pi\,\hbar^2 a_{xy}}{\mu_{xy}} \int \tilde{w}_x(\mathbf{r})^2\,\tilde{w}_y(\mathbf{r})\,dV, \tag{3.19}$$

parametrized by the respective reduced mass and s-wave scattering length, where the self-consistent Wannier function $\tilde{w}(\mathbf{r})$ replaces its single-particle counterpart. However, this description is rather poor, owing to the change in potential and kinetic energy associated with any modification of the Wannier function. Intuitively, it is clear that this contribution to the total energy can never be neglected, as, after all, it is the reason why the interaction correction to the single-particle Wannier functions is usually finite. In other words, if there were no significant change of the single-particle contributions to the total energy, the self-consistent wave-functions would either collapse or broaden without end, depending on the sign of the interaction. It is therefore crucial to include the change in potential and kinetic energy, leading to an alternative definition of the *renormalized* interaction energy:

$$E_{int}(n_b, n_f) = E_{tot}(n_b, n_f) - E_{tot}(n_b \cdot \epsilon_b^0 + n_f \cdot \epsilon_f^0). \tag{3.20}$$

That is, the interaction energy is the energy difference between the actual system of interacting particles and a corresponding (hypothetical) system of non-interacting particles, i. e. the sum of all single-particle energies in the system[7]. It is interesting to note that for the mixture, it is in general not possible to exactly separate the contributions of intra- and interspecies interactions, as the change in the boson kinetic and potential energy has to be attributed in parts to either the inter- and the intraspecies interaction. If we assume this correction to be small compared to the contribution of the aforementioned density overlap integrals 3.19, and distribute the energy corrections accordingly, we arrive at effective values

$$\tilde{U}_{bb}(n_b, n_f) = U_{bb}(n_b, n_f) + \frac{2\,\alpha\, n_b\, \delta\epsilon_b}{n_b\,(n_b - 1)} \tag{3.21}$$

$$\tilde{V}_{bf}(n_b, n_f) = V_{bf}(n_b, n_f) + \frac{n_f\, \delta\epsilon_f + (1-\alpha)\, n_b\, \delta\epsilon_b}{n_b\, n_f}, \tag{3.22}$$

where U_{bb}, V_{bf} are the contributions from equation 3.19, ϵ_b, ϵ_f are the single-particle energy corrections for Bosons and Fermions, respectively, and $\alpha = \frac{|V_{bf}|}{U_{bb}}$. Figure 3.7 shows values for the effective interboson repulsion $\tilde{U}_{bb}$, for two Bosons in the presence of a Fermion, for different values of the lattice depth and interspecies scattering length. For repulsive interspecies interactions, the bosonic repulsion is slightly reduced, while for interspecies attraction, a significant increase in the effective interboson repulsion can be seen. At lattice depths in the vicinity of the usual bosonic superfluid to Mott insulator transition, the enhancement can be on the order of twenty percent at the background Bose-Fermi interaction. The resulting bending of the isometric lines visible in figure 3.7 may lead us to expect a shift

---

[7] In fact, this is the basic definition for any interaction energy, for which the formulas usually adopted in the realm of cold atom Hubbard physics are an approximation.

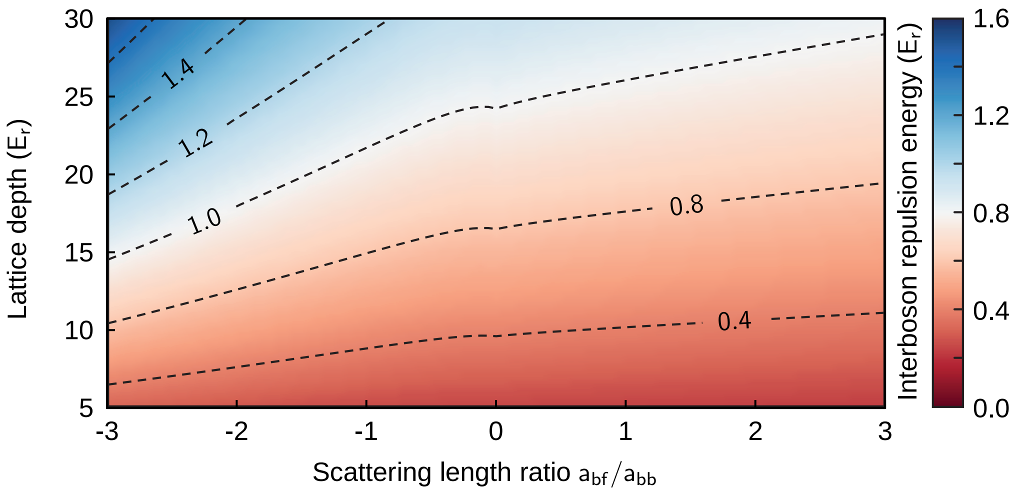

Figure 3.7: Effective interboson onsite repulsion in the presence of a Fermion, depending on the interspecies scattering length and the lattice depth. The bending of the isometrics (dashed lines) indicates a shift of the bosonic Mott insulator transitions towards deeper (shallower) lattices for attractive (repulsive) interspecies interactions.

of the bosonic Mott insulator transition in the presence of fermions, towards deeper or shallower lattices, for attractive or repulsive interspecies interaction, respectively. We can now write the total interaction energy approximately as

$$E_{int}(n_b, n_f) = \frac{n_b\,(n_b - 1)}{2}\,\tilde{U}_{bb}(n_b, nf) + n_b\,n_f\tilde{V}_{bf}(n_b) \tag{3.23}$$

The explicit n_b-dependence of the interaction energy parameters gives rise to contributions of order $\mathcal{O}(n_b^3)$ and $\mathcal{O}(n_b^2)$ and higher to the intra- and interspecies interaction energy, respectively. It has been pointed out [79] in the case of pure bosonic systems, that such contributions can be interpreted as effective many-particle interactions, and the same line of arguments readily holds in the mixture case. We can thus conclude that the renormalization of the Hubbard parameters occuring due to the self-consistency condition can be understood in terms of an extended Hubbard model including effective many-particle onsite interactions.

Renormalized tunneling

Now that we have established a renormalization of the interaction energy due to the appearance of self-consistent Wannier orbitals, it is natural to ask

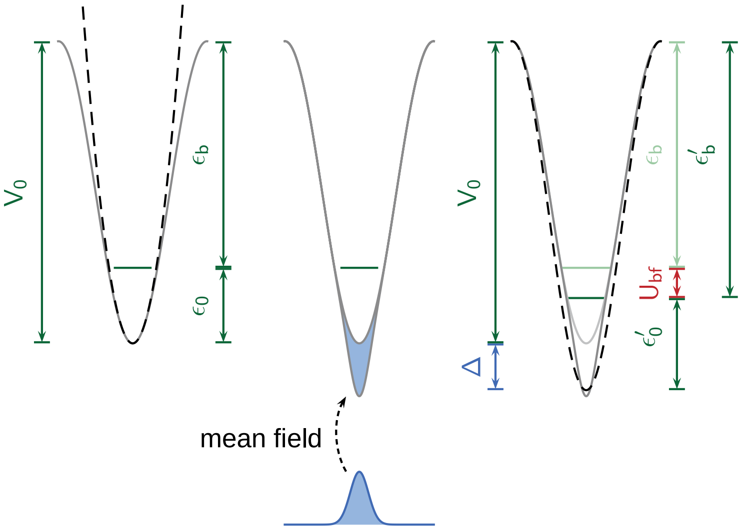

Figure 3.8: Effective lattice depth determining the renormalization of the bosonic tunneling. (a) Lattice potential (grey) of depth V_0 and harmonic approximation (dashed line) for a single lattice site. The lowest bound state (green line) has a zero point energy ϵ_0 and a binding energy ϵ_b. (b) The mean field interaction with a fermionic onsite density (blue) gives rise to an effective potential, which, in case of an attractive interaction, is deeper than the bare lattice potential. (c) The effective potential is approximated by a pure sinusoidal potential of depth $V_0' = V_0 + \Delta$, such that the binding energy of the lowest bound state is shifted according to the Bose-Fermi interaction energy V_{bf}.

for consequences with respect to the other central parameter of Hubbard-type models, i. e. the hopping J. As we know that an attractive interaction tends to shrink the Wannier function while a repulsive interaction broadens it, we expect the tails of the wavefunction to extend less (more) deeply into the intersite tunneling barrier for attractive (repulsive) onsite interaction. Thus, the overlap with the Wannier function localized on the neighbouring site, and thus the hopping strength, is reduced for attractive onsite interaction, and enhanced for onsite repulsion. A numerical estimate however is hard to get from the variational model used so far, as the Gaussian trial wavefunction is supposed to be a good approximation to the true orbital in the center of the site, where the potential is more harmonic, while it is poor in describing the wings in the strongly anharmonic part of the potential[8]. We therefore have to resort to a different approximation in order to estimate the correction to the tunneling. This can be done as follows: The single-particle orbitals are known from the band-structure calculation outlined in section 2.2. From the point of view of a single particle, and within the mean-field approximation, the presence of other particles, with which it interacts, will give rise to another periodic potential (in addition to the optical lattice), the shape and amplitude of which are given by the density associated with the self-consistent Wannier orbitals, and the interaction strength, respectively. In total, the particle will see a flattened or deepened periodic potential, depending on the sign of the interaction. Its effective tunneling can therefore be obtained from the calculation of the band structure of this effective periodic potential, analogously to equation 3.6. This scheme can be largely simplified by observing that the change in shape of the resulting potential is minor, and the change in depth largely dominates (see also figure 2 in reference [98]). Therefore, we can neglect all higher Fourier components and solve the well-known bandstructure problem from section 2.2, for an effective lattice depth. A better estimate can be obtained by including the Fourier components of the Fermion density into the matrix 2.11, and subsequent diagonalization [96].

In order to estimate the change in the effective lattice depth, we consider a *chimera* model, assuming that the potential is sufficiently well described by a harmonic approximation close to its bottom, and that the lowest band can be treated in the harmonic approximation. This would be the case in the absence of interactions for lattice depths exceeding approximately $5\,E_r$, as can be seen from figure 2.3. The zero point energy of the lowest band above the trap bottom is then given by

$$\epsilon_0 = \frac{\hbar\omega_0}{2} = \sqrt{\tilde{V}_0}\,E_r, \tag{3.24}$$

On the other hand, the lattice is only finitely deep, giving rise to a binding energy

$$\epsilon_b = (\tilde{V}_0 - \sqrt{\tilde{V}_0})\,E_r \tag{3.25}$$

For an effective lattice depth $\tilde{V}_0 + \Delta\tilde{V}_0$, the corresponding binding energy

---

[8] This is of course true even in the absence of any interaction.

would be

$$\begin{aligned}\epsilon_b' &= \left(\tilde{V}_0 + \Delta\tilde{V}_0 - \sqrt{\tilde{V}_0 + \Delta\tilde{V}_0}\right) E_r \\ &= \left(\tilde{V}_0 + \Delta\tilde{V}_0 - \sqrt{\tilde{V}_0}\,\sqrt{1 + \Delta\tilde{V}_0/\tilde{V}_0}\right) E_r \\ &= \left(\tilde{V}_0 + \Delta\tilde{V}_0 - \sqrt{\tilde{V}_0}\left(1 + \tfrac{\Delta\tilde{V}_0}{2\,\tilde{V}_0} + \mathcal{O}\left(\left(\tfrac{\Delta\tilde{V}_0}{\tilde{V}_0}\right)^2\right)\right)\right) E_r\end{aligned} \tag{3.26}$$

Rearranging terms, we obtain

$$U_{bf} = \epsilon_b' - \epsilon_b = \Delta\tilde{V}_0\left(1 - \frac{1}{2\sqrt{\tilde{V}_0}}\right) E_r.$$

Thus, the effective increase in the lattice depth $\Delta\tilde{V}_0$ is on the order of U_{bf}. Figure 3.9 shows the change in the tunneling timescale estimated using a band structure calculation based on equation 3.2.

Exact diagonalization

It is important to note that the variational model used so far has only qualitative prediction power. Quantitatively reliable results can be obtained from an *exact diagonalization* calculation[9], where the eigensystem of a suitably truncated version of the Hamiltonian matrix is found numerically using sparse-matrix tools such as the Lanczos algorithm. These inherently brute-force approaches have the advantage that they do not rely on a very smart choice of a basis set, allowing e. g. for the use of computationally handy Harmonic oscillator eigenfunctions. Also, for large enough basis sets, the results always become exact within the numerical accuracy[10].

While direct exact diagonalization also trivially works for a single fermion, it is usually prohibitive to use it for the mixture, as the calculation would have to be performed on the tensor product of the basis sets used for the individual species[11]. Instead, exact diagonalization is performed on one single

---

[9] A different approach, which is however inherently limited to single-component Bose gases and weak interactions, has been proposed in reference [95].

[10] It should be noted that in this limit, exact diagonalization in the harmonic oscillator basis is equivalent to the perturbative expression for a single-component Bose gas given in reference [79], when the perturbation series is taken to infinite order.

[11] For each individual species, the required basis set scales as the third power of the number of orbitals included. Including only bound orbitals in a reasonably deep lattice already produces a total dimensionality in excess of 4×10^3. Realistic basis sets include also orbitals which energetically belong to the continuum.

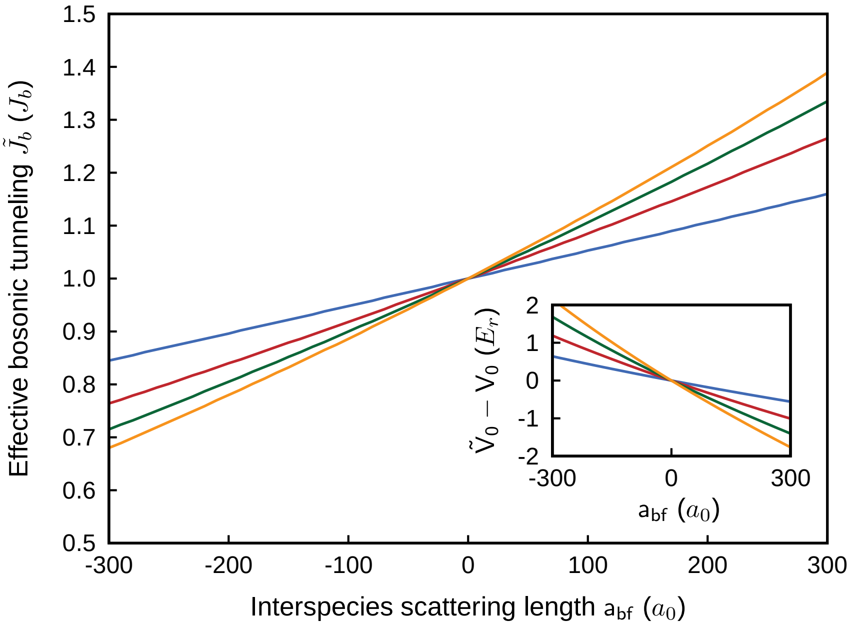

Figure 3.9: Effective bosonic tunneling in the presence of one Fermion per site, depending on the interspecies scattering length. The different curves correspond to bare lattice depths of $5\,\mathrm{E_r}$ (blue), $10\,\mathrm{E_r}$ (red), $15\,\mathrm{E_r}$ (green) and $20\,\mathrm{E_r}$ (orange). The inset shows the increase (or decrease, for repulsive interspecies interactions) $\Delta\tilde{V}_0$ of the effective potential depth with respect to the bare lattice depth $\tilde{V}_0$. All data assume a single Boson interacting with a Fermion.

species after the other, with the complimentary species providing a mean-field potential, and iterated in a self-consistency loop until convergence is found.

Exact diagonalization calculations for some parameters used in this work have been performed by D.-S. Lühmann [97, 98]. A comparison with the variational results presented earlier indicates that the corrections predicted by these are typically too small by a factor of approximately two. The qualitative predictions of the variational model have been validated in all situations where direct comparison was feasible. Therefore, the variational method is to be preferred in many situations where numerical accuracy is not of large concern, due to the vast saving of computational time[12].

---

[12] The practical difference in our situation can be between few seconds for a variational calculation on the one hand and hours for the exact diagonalization on the other hand.

3.3 Predictions based on the Bose-Fermi Hubbard model

In this section, we shortly review some of the most important theoretical predictions in the context of the Bose-Fermi Hubbard model, and comment on the underlying assumptions.

Effective interactions

The complexity of the full Bose-Fermi Hubbard Hamiltonian has so far forced theory work to concentrate on effective models, which arise within certain parameter limits. These fall into two main classes, depending on the assumed importance of the interspecies interaction. We shall discuss both limits shortly in the following section.

Weak coupling regime

If the interspecies interaction can be considered small compared to the energy scales of the bare Boson system, a perturbative approach to the Bose-Fermi Hubbard problem is possible. It is important to keep in mind however, that this treatment is inherently limited to the case where the Bose-Fermi interaction is weak enough that no new bound (localized) states can be formed. More specifically, it is not sufficient for the Bose-Fermi interaction to satisfy $|V_{bf}| \ll U_{bb}$, but we also need $|V_{bf}| \ll \Delta_b = 4\, J_b$, which, when dealing with the bosonic Superfluid to Mott insulator transition, is a much stronger condition.

Büchler and Blatter [20, 19] have considered a linear response treatment of the Bose-Fermi interaction. Hereby, the fermions respond to a density fluctuation δn_b of the bosons with a density change

$$\delta n_f \approx -\chi\, V_{bf}\, \delta n_b, \tag{3.27}$$

the strength of which is governed by the interspecies interaction energy V_{bf}. The susceptibility χ mainly depends on the density of states near the Fermi energy. The back-action of the fermions on the bosons results in an energy shift

$$\delta E_b \approx -\frac{1}{2}\, \chi\, U_{bf}^2\, \delta n_b^2 \tag{3.28}$$

and thus an effective interboson attraction. The phase diagram of the mixture is then dominated by the interplay between this effective attraction and the *native* repulsion between the bosons. In particular, reference [19] highlights the importance of van Hove type singularities in the fermionic density of states in the case of a two-dimensional system, resulting in a strong temperature-dependence of the fermion response function and thus the strength of the effective attraction.

Screening of interboson repulsion

The fermionic *screening* of the interbosonic interactions, as it arises from equation 3.28, is predicted to be independent of the sign of the interspecies interaction. Moreover, it has been argued that due to this screening of interactions, the presence of fermions suppresses the formation of the bosonic Mott insulator, which would only occur at larger values of the bare interaction to tunneling ratio as compared to the pure bosonic case (see reference [146] and references therein). However, these arguments are based on the idea of instantaneous or static screening, which may in fact not be applicable. It has been pointed out recently [123] that the ability of the Fermi gas to react to an external perturbation (as induced by the bosons), is largely limited by the antisymmetrization principle. If we consider a single particle-hole excitation on top of a Mott insulating region of bosons, the situation looks like a localized impurity potential from the fermions' point of view, which affects all occupied states in the Fermi sea. If the boson wants to tunnel to an adjacent site, all fermionic states will have to adjust to the new impurity configuration. As a consequence, the bare tunneling amplitude J_b will be replaced by an effective amplitude taking into account the overlap of the initial and final many-body wavefunction of the fermions. Although the modification of any individual state might be small, the total many-body suppression factor, which arises from the product of $\mathcal{O}(N_f)$ individual overlap contributions (where N_f is the number of fermions in the system), can deviate significantly from one, and in fact vanishes in the macroscopic limit $N_f \to \infty$, a behaviour known from electrons in traditional solid-state physics under the term *orthogonality catastrophe* [4, 133]. The role of Anderson's orthogonality catastrophe in mesoscopic systems, where the suppression factor always remains finite, has been established recently in [71]. The importance of the orthogonality catstrophe argument has been shown to depend largely on the fermionic tunneling in comparison to the other energy (time) scales in the problem: If the fermions can be considered fast, i. e. the width of the fermion band is large compared to the interaction energy scale U_{bb}, then the screening can again be considered instantaneous and the previous conclusions can be recovered, however, if the fermions are slow, i. e. the width of their band is significantly smaller than both U_{bb} and V_{bf}, then the static screening is not present, and the dominant effect of the fermions is a suppression of bosonic tunneling. If this dynamical character of the fermionic screening is taken into account in the framework of mean-field theory, a suppression of the bosonic superfluid density and an enhancement of the Mott-insulating regions may result [123].

It should, however, be noted that a different approach, employing perturbation theory to arrive at an effective field theory for the bosons, and including a correction to account for the dynamical nature of the screening, still concludes that the Mott insulator transition for the bosons should be suppressed [99], unless the single-band approximation is to be lifted, as our results in the previous chapter and the theoretical work in reference [98] clearly suggest. In the context of an extended multi-band Hubbard model, the same theoretical approach predicts an enhancement of the Mott insulator regions in the phase diagram, albeit for either sign of the Bose-Fermi interaction [146]. It has also beeen conjectured, again in the limit of weak Bose-Fermi interactions, that the character of the quantum phase transition between the bosonic superfluid and Mott insulator might be altered. In particular, the well-known Mott lobes in the phase diagram should only be affected near their tip, where the phase transition happens at fixed chemical potential [160].

Strong coupling regime

If the tunneling of both fermions and bosons is assumed to be weak compared to the interactions, it is instructive to first consider the zero-tunneling limit. This situation has been considered e. g. by Lewenstein and coworkers [94]. Departing from $V_{bf} = 0$, where the familiar bosonic Mott insulator is unaffected by the underlying Fermi sea, they predict that the regime which can be treated perturbatively is limited to

$$\mu - (\bar{n}_b - 1)\, U_{bb} < V_{bf} < \mu - \bar{n}_b\, U_{bb}, \tag{3.29}$$

where μ is the boson chemical potential, and $\bar{n}_b$ the filling of the Mott insulator. If the interspecies interaction becomes more attractive, the fermions will attract additional bosons to the sites they occupy, if it is more repulsive, they will push them away (i. e. attract bosonic holes). Thereby, fermionic composite particles are formed, consisting of one fermion and a certain number of bosonic particles or holes. The zero-tunneling phase diagram will then be divided into distinct regions, each of them corresponding to a well-defined number of bosons or bosonic holes as part of the composite particle[13]. In the case of finite, yet small tunneling $J = J_f = J_b$, second

---

[13] This also gives an indication that the strongly interacting system is asymmetric with respect to the sign of the interspecies interaction. Clearly, the number of bosons per

order degenerate perturbation theory leads to an effective model of spinless fermionic quasiparticles with nearest-neighbour interactions [94]

$$H_{eff} = -\tilde{J} \sum_{\langle i,j \rangle} (\tilde{f}_i^\dagger \tilde{f}_j + h.c.) + \tilde{K} \sum_{\langle i,j \rangle} m_i m_j, \tag{3.30}$$

where $\tilde{f}_i^\dagger, \tilde{f}_i$ are the creation and annihilation operators of the composite particles on a site i, and $m_i = \tilde{f}_i^\dagger \tilde{f}_i$ is the corresponding density operator. It should be noted that this model is quite distinct from the usual fermionic Hubbard model, both in the lack of a second spin component, and thus an onsite interaction term, and in the appearance of the next-neighbour interaction term. Also, the compounds of the fermionic quasiparticles have been fully absorbed in the model parameters. For a given ratio $\frac{V_{bf}}{U_{bb}}$ and chemical potential μ, the basic scaling of the effectiv interaction is given by

$$\tilde{K} \propto \frac{J^2}{U_{bb}} \tag{3.31}$$

highlighting the exchange character, although it is important to note that $\tilde{K}$ can be both attractive or repulsive. The effective tunneling is less universal in that respect, and has to be calculated individually for each region of the zero-tunneling phase diagram (i. e. each type of possible composite particle). The resulting spinless fermion model with repulsive interactions is known to contain both Fermi liquid and density wave phases at half filling of the Fermions, depending on the ratio $\tilde{K}/\tilde{J}$. For weak attractive interactions, the composite fermions may form a BCS-superfluid, while sufficiently large attractive interactions may lead to a ferromagnetic domain insulator [94]. A similar situation, albeit in the limit of *heavy Fermions*, namely

$$J_f \ll J_b \ll U_{bb}, V_{bf} \tag{3.32}$$

has been investigated by Mering and Fleischhauer [105]. In this case, the fermions constitute a binary disorder[14]. Partially compressible gapless phases similar to the Bose glass [44] may appear. In the case of finite fermionic tunneling the results for the annealed case qualitatively agree with those obtained in the composite fermion framework discussed above.

---

composite is a priori only limited by the boson to fermion ratio in the system (for a homogeneous system), and may be even larger in the inhomogeneous case, whereas the number of holes is stricly limited by $\bar{n}_b$.

[14] At small, but finite fermionic tunneling, the disorder may appear quenched or annealed, depending on the observation time scale.

Numerical results

Several efforts have been made to solve the Bose-Fermi Hubbard problem numerically. Most of these studies restrict themselves to the one-dimensional problem, where powerful calculational techniques exist. However, it is in general not clear whether it is possible to generalize the obtained results to higher dimensions. Exact diagonalization studies of small systems with repulsive interspecies interactions [132] provided evidence for the existence of three distinct insulating states in the system, namely the bosonic Mott insulator, a crystalline density wave phase where bosons and fermions occupy adjacent sites, and a phase consisting of separated domains of bosons and fermions. For $V_{bf} \approx U_{bb}$, the fermions tend to suppress the bosonic Mott insulator and restore superfluidity, while for $V_{bf} \gg U_{bb}$, the competing *unmixed* insulating phases may appear. For deep optical lattices with strong interactions, *quasi-disordered* states have been found, similar to the Bose glass [1]. Unlike in the pure bosonic case, where such phases arise from a disordered potential, in the case of the mixture, they can be traced back to the large number of quasi-degenerate configurations energetically accessible to the mixed system, such as a single Fermion on a background of lattice sites filled with bosonic atoms.

Supersolidity

A particularly interesting exotic quantum phase termed *supersolid* has been predicted to occur in bosonic systems with an effective next-neighbour interaction [152], which may arise due to dipolar interactions [57] or via coupling to a second species, either bosonic [103] or fermionic [19]. The supersolid phase is characterized by the presence of both diagonal and off-diagonal long range order at the same time, i.e. the system displays both long-range phase-coherence (and hence superfluidity), and non-trivial density-density correlations, which is typical for crystalline order, at the same time. In a two-dimensional system, the picture of a checkerboard is often invoked to describe the situation, where the black and white fields correspond to lattice sites occupied by Bosons and Fermions, respectively. The role of the Fermions in the system can be thought of as restricting access to the white fields for the Bosons. The emergence of the density wave is thus easily seen. The coherence stems from the fact that any assignment of *black* and *white* labels to the lattice sites is of course arbitrary. Therefore, we have to consider the superposition of the black-and-white checkerboard and its inverted counterpart, leading to an atom number uncertainty on all lattice sites, and thereby to a finite value of the off-diagonal long-range order

$\langle a_i^\dagger a_j \rangle_{i \neq j}$. While the argument given so far critically relies on half filling for both Bosons and Fermions, DMFT[15] calculations have shown that depending on the filling factors of Bosons and Fermions, slightly more complicated phases meeting the supersolidity criterion can emerge, in which the density wave structure shows a much smaller modulation [148, 149]. On the one hand, this enhances the probability that supersolid phases may exist in real systems, where the filling can not be controlled with very good accuracy. On the other hand, the detection of this low-amplitude density wave is challenging with experimental methods at hand. The question whether the delicate checkerboard order, which always has to compete with phase separation in order to exist (see e. g. [20, 19]), will survive in a trapped, and thereby necessarily inhomogeneous and finite system, is still unresolved [69], although recent real-space DMFT calculations seem to suggest it [147]. However, no experimental evidence of supersolidity in optical lattices has been found to date[16].

Adiabatic heat exchange

It has also been argued that for finite temperature systems, the dominant effect may be of thermodynamic origin. If we assume that the atoms are transferred from some trapping potential which is approximately harmonic into the optical lattice periodic potential in an adiabatic way, then the total entropy of the system must be conserved. However, if the two components in the mixture interact, they may exchange heat, and their individual entropies need not be conserved. Instead, it is to be assumed that if the interactions are sufficiently strong, the two components will eventually reach the same temperature in the optical lattice. Taking into account the initial and final density of states for both species, Cramer and Eisert [30] suggest that in this process, the bosons are heated with respect to their reduced temperature T/T_c. Therefore, an apparent reduction of superfluidity in the system might in fact be due to a reduction of the degree of degeneracy of the Bose gas [120]. The strength of the effect largely depends on the details of the trapped system, and calculations taking into account realistic experimental parameters for the setup presented in this work are currently being carried out [29].

---

[15] Dynamical mean field theory, see e. g. reference [72].

[16] Evidence for supersolidity has been reported from torsional oscillator experiments in Helium [83, 127], but the interpretation of these experiments is not yet fully clear, and the observed strength of the effect disagrees with standard theory [15, 126].

Four

Probing interaction effects via quantum phase diffusion

This chapter presents experiments aiming at demonstration as well as quantitative measurement of effects induced by the interspecies attraction, making use of the well-known quantum phase diffusion dynamics of a bosonic matter wave in an optical lattice. Parts of the results presented here have been published in references [157] and [156].

4.1 Quantum phase diffusion of the macroscopic matter wave

Time evolution of coherent states

We will first consider a coherent state within an individual well of the lattice potential. This state is characterized by a complex number α, which is related to the mean bosonic particle number $\bar{n}_b = \langle\alpha|\hat{n}_b|\alpha\rangle = |\alpha|^2$. Without loss of generality, we can assume that α is real at time $t = 0$. It is convenient to write this initial state in the local Fock basis:

$$|\alpha\rangle = e^{-|\alpha|^2/2} \cdot \sum_{n_b} \frac{\alpha^{n_b}}{\sqrt{n_b!}}|n_b\rangle \tag{4.1}$$

If we neglect interactions, the Hamiltonian is linear in the particle number, i. e. $H = n_b \cdot \hbar\omega$, and the time evolution is given by:

$$\begin{aligned} |\alpha\rangle \rightarrow |\alpha(t)\rangle &= e^{-|\alpha|^2/2} \cdot \sum_{n_b} \frac{\alpha^{n_b}}{\sqrt{n_b!}} e^{-i n_b \omega t} |n_b\rangle \\ &= e^{-|\alpha|^2/2} \cdot \sum_{n_b} \frac{\left(\alpha \cdot e^{-i\omega t}\right)^{n_b}}{\sqrt{n_b!}} |n_b\rangle = e^{-i\omega t} |\alpha\rangle . \end{aligned} \tag{4.2}$$

The coherent state is thus an eigenstate of the noninteracting Hamiltonian, or quite generally any Hamiltonian which is strictly linear in the boson number n_b. As a consequence, the coherent macroscopic matter wave remains stable as long as interactions can be neglected.

Time evolution with interactions

Now, we introduce interactions. We will first review the basic dynamics neglecting orbital effects altogether. The interboson repulsion term in the Hamiltonian is nonlinear in n_b, and the coherent state will therefore not persist under the full Hamiltonian. On the other hand, each Fock state $|n_b\rangle$ clearly is an eigenstate of the interaction term with eigenenergy

$$\frac{U}{2}\, n_b\, (n_b - 1). \tag{4.3}$$

We therefore obtain the full time evolution as

$$|\alpha\rangle \rightarrow |\alpha(t)\rangle = e^{-i\omega t} e^{-\bar{n}_b/2} \cdot \sum_{n_b} \frac{\alpha^{n_b}}{\sqrt{n_b!}}\, e^{-\frac{i}{\hbar}\frac{U}{2} n_b\, (n_b - 1)\, t} |n_b\rangle . \tag{4.4}$$

The macroscopic matter wave can be characterized by the expectation value of the boson annihilation operator $\hat{a}$, yielding

$$\begin{aligned} \langle \hat{a} \rangle &= \langle \alpha(t) | \hat{a} | \alpha(t) \rangle \\ &= e^{-\bar{n}_b} \sum_{n_b, n_b'} \frac{(\sqrt{\bar{n}_b})^{n_b + n_b'}}{\sqrt{n_b!\, n_b'!}}\, e^{-\frac{i}{\hbar}\frac{U_{bb}\, t}{2}\,(n_b(n_b-1) - n_b'(n_b'-1))} \langle n_b' | \hat{\alpha} | n_b \rangle \end{aligned} \tag{4.5}$$

and, with the well-known matrix elements $\langle n_b' | \hat{\alpha} | n_b \rangle = \sqrt{n_b}\, \delta(n_b', n_b - 1)$,

$$\langle \hat{a} \rangle = \sqrt{\bar{n}_b}\, e^{-\bar{n}_b} \sum_{n_b} \frac{\bar{n}_b^{n_b}}{n_b!}\, e^{-\frac{i}{\hbar} n_b\, U_{bb}\, t} \tag{4.6}$$

Clearly, the individual Fock components of the initially coherent state

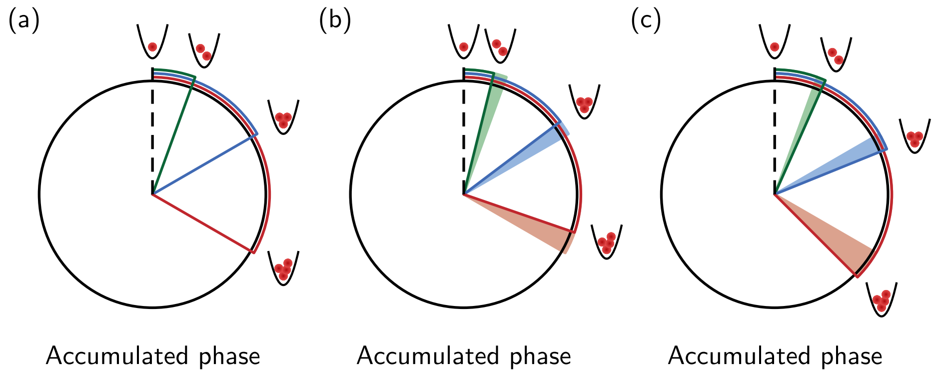

Figure 4.1: Phase evolution of individual Fock states. (a) Evolution assumed in usual single-band Hubbard model. All energies are harmonics of the interaction parameter U. (b) Evolution with renormalized interaction energies, as obtained from self-consistent bosonic Wannier orbitals. Effectively, the time evolution is slowed down as compared to the harmonic case (Indicated by the shaded areas). (c) Evolution in the presence of Fermions, assuming attractive Bose-Fermi interaction, obtained from self-consistent bosonic and fermionic orbitals. In this case, the time evolution is speeded up.

will dephase under the interboson interaction[1], as illustrated in figure 4.1 (a), and the macroscopic matter wave field will collapse. The dynamics can be visualized using the Q-function, defined on the complex plane as $Q(\beta,t) = \frac{1}{\pi}\left|\langle\beta|\alpha(t)\rangle\right|^2$ [113]. However, as all energies occuring in the time evolution are integer multiples of U, the Fock states will always rephase after a time $t_r = \frac{h}{U}$ and the macroscopic matter wave will revive. This dynamical evolution of the matter wave is visualized in figure 4.2. The time scale of the collapse decreases with increasing mean occupation number. We can understand this behaviour if we consider

$$\begin{aligned}
\frac{|\langle\hat{a}\rangle|}{\sqrt{\bar{n}_b}} &= \left| e^{-\bar{n}_b}\sqrt{\bar{n}_b}\sum_{n_b}\frac{\bar{n}_b^{n_b}}{n_b!}\, e^{-\frac{i}{\hbar}\frac{U_{bb}}{2}\,(n_b\,(n_b-1)-(n_b-1)(n_b-2))\,t}\right| \\
&= \left| e^{-\bar{n}_b}\sqrt{\bar{n}_b}\sum_{n_b}\frac{\bar{n}_b^{n_b}}{n_b!}\, e^{-\frac{i}{\hbar}U_{bb}\,n_b\,t}\right| \qquad (4.7)\\
&= |e^{-\bar{n}_b}\sqrt{\bar{n}_b}\,\exp\left(\bar{n}_b\, e^{-\frac{i}{\hbar}U_{bb}\,t}\right)| \\
&= |\sqrt{\bar{n}_b}\,\exp\left(\bar{n}_b\left(e^{-\frac{i}{\hbar}U_{bb}\,t}-1\right)\right)|
\end{aligned}$$

---

[1] The situation is very much analogous to the Kerr effect in quantum optics.

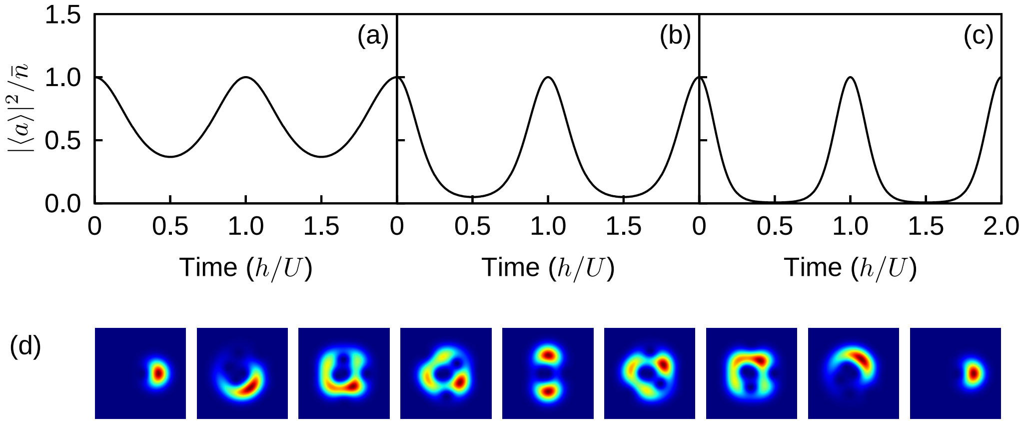

Figure 4.2: Collapse and revival of the macroscopic matter wave. (a)-(c) show the normalized expectation value of the matter wave field evolving in time, for mean occupation numbers of $\bar{n} = 0.5, 1.5$ and 2.5, respectively. Both the time scale of the collapse and the minimum value decrease strongly for higher filling. (d) Q-function plot for time steps of $\frac{U}{h}t = \nu \cdot \frac{\pi}{4}$, $\nu = 0 \dots 8$, corresponding to the first collapse and revival cycle in (b). Note the appearance of a Schrödinger cat state corresponding to the collapse of the matter wave field.

and expand the exponent to second order in time

$$\begin{aligned} &= \left|\sqrt{\bar{n}_b}\; e^{-\frac{i}{\hbar} U_{bb}\, \bar{n}_b\, t}\; e^{-\frac{U_{bb}^2\, \bar{n}_b}{\hbar^2}\, t^2}\right| \\ &= \sqrt{\bar{n}_b}\; e^{-\frac{U_{bb}^2\, \bar{n}_b}{2\,\hbar^2}\, t^2}. \end{aligned} \tag{4.8}$$

In the vicinity of each revival, the expectation value of the macroscopic matter wave therefore behaves as a Gaussian, with a collapse time scale given by $h/(\sqrt{\bar{n}_b}\, U_{bb})$. Before we proceed to a more accurate picture of the time evolution, it is worthwhile to explain how this collapse and revival dynamics can be triggered and monitored in an experimental situation. This experiment in a pure bosonic quantum gas was first performed by Greiner *et* al. [61], and we shall essentially follow the same procedure.

The experiment starts with an adiabatic ramp into a shallow optical lattice. If we assume interaction effects to be small, we will thus have a coherent state with a Poissonian atom number distribution on every lattice site. A fast increase in lattice depth then freezes out this distribution. At the same time, the interaction energy becomes important, and the time evolution given by equation 4.6 is triggered. After some hold time, the lattice and the confining potential are instantaneously switched off, and the

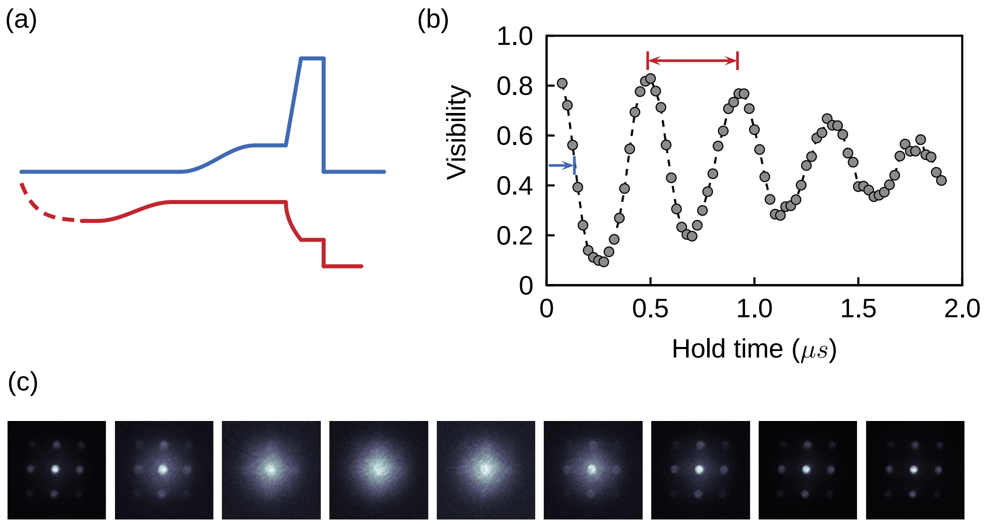

Figure 4.3: Experimental observation of collapse and revival dynamics of the macroscopic matter wave field in a pure bosonic sample. (a) Ramp sequences for dipole trap (red curve) and optical lattice (blue curve). Both curves are not drawn to scale. (b) Observed visibility vs. hold time, for a lattice depth ramp from $8\,\mathrm{E_r}$ to $22\,\mathrm{E_r}$ in $50\,\mu$s. Also shown are the extraction of the mean interaction energy (red) and the collapse time (blue) from the measured traces. (c) Representative TOF images corresponding to the measurements in (b), for times $t = 50 \ldots 100\,\mu$s, in steps of $50\,\mu$s from left to right.

atoms are imaged after TOF. The contrast of the resulting matter wave interference pattern is then measured in terms of the visibility

$$\mathcal{V} = \frac{n_{\boxdot} - n_{\square}}{n_{\boxdot} + n_{\square}} \tag{4.9}$$

where $n_{\boxdot}$ and $n_{\square}$ are the atom numbers within the boxes at the expected peak positions and suitable reference positions, analogous to the definition in [52]. Figure 4.3 illustrates the procedure and shows the result of a measurement of the dynamics at $22\,\mathrm{E_r}$ with a pure bosonic sample. In the experiment, the dynamics reveals to be damped on a timescale of several revival periods. We have verified that the decay is hindered by increasingly deeper final lattice potentials. This example demonstrates that we can measure the revival time scale and thus the interaction energy with high precision using the procedure outlined above. It should be noted however, that this way, we only obtain an averaged interaction energy, neglecting the intrinsic particle number dependence. In the following sections, we will explore what can be learned from this averaged information. Finally, in the last section of this chapter, we will go beyond this and try to identify the individual frequency components.

4.2 Changing the interaction energy

As we now have at hand a tool for precise measurements of the interaction energy, we can try to elucidate the effects of a fermionic admixture to the system. For simplicity, we will start in a scenario where essentially all bosons sit on lattice sites occupied by a fermion. For attractive interactions and suitable atom numbers, this assumption will be validated *a posteriori*, see section 4.3. In case interactions are weakly attractive or even repulsive, or the atom numbers are not suitable to fulfill this condition, additional effects will have to be taken into account, which we will defer until section 4.5.

Shift of the mean interaction energy

What kind of modifications have to be expected upon addition of fermions to the system? Within the theoretical framework given in section 4.1, the only measurable modification should be a change in the interboson interaction energy due to the adaption of the self-consistent Wannier functions as described in section 3.2. The additional interspecies interaction contribution to the Hamiltonian given by 3.3 will not contribute to the experimental signature, but is absorbed in a non-measurable global phase, as any other energy contribution which is linear in the bosonic atom number (see equation 4.2). In order to verify the expected change in the revival timescale, we use an experimental sequence similar to the one in the previous section, however, adding fermions to the mixture this time. Right before the rapid change in lattice depth which triggers the collapse and revival dynamics, we may now blast the fermions out of the system using a short pulse of resonant light. We have verified that this procedure has negligible effect on the coherence of the bosonic matter wave. Furthermore, the pulse is short as compared to the bosonic tunneling timescale, so the atom number distribution of the bosons can not adapt to the new situation. This way, we can make sure that the initial state, i. e. the atom number distribution is the same, whether or not the fermions participate in the actual collapse and revival experiment. We can then measure the revival timescale with or without the fermions. The result of this experiment can be seen in figure 4.4. As expected, the interspecies attraction leads to a shrinking of the

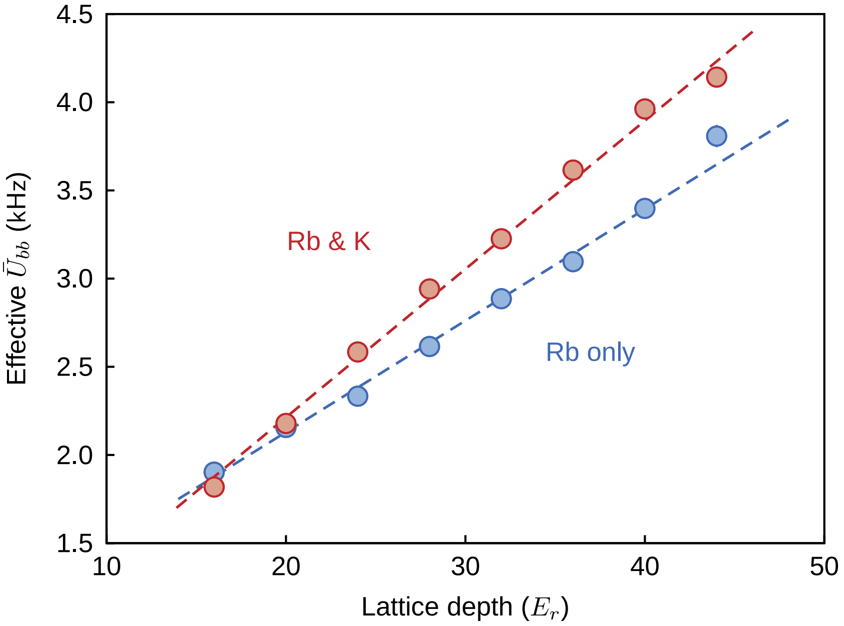

Figure 4.4: Shift of effective interaction due to an attractive interspecies interaction. Comparing the measured frequencies in the presence (red points) and absence (blue points) of Fermions, we find that the Bose-Fermi attraction indeed enhances the effective Bose-Bose repulsion, leading to a speed-up of the collapse and revival dynamics. The lines are just a guide to the eye.

bosonic Wannier function, which in turn enhances the interboson repulsion. Therefore, the collapse and revival dynamics is clearly accelerated as compared to the pure boson case. Furthermore, we observe an enhanced damping of the dynamics in the presence of fermions. This damping can at least partly be attributed to a finite tunneling of the fermions during the hold time, opening a way towards relaxation of the system. Moreover, we will have to consider the role of dependence of the Wannier function on the actual atom number, as described in section 4.6.

4.3 Probing interaction-induced changes of filling

In section 4.1, we have shown how the collapse part of the dynamics yields information on the filling in the system. Under the assumption of a Poissonian distribution, the decay shows a Gaussian shape, and the mean atom

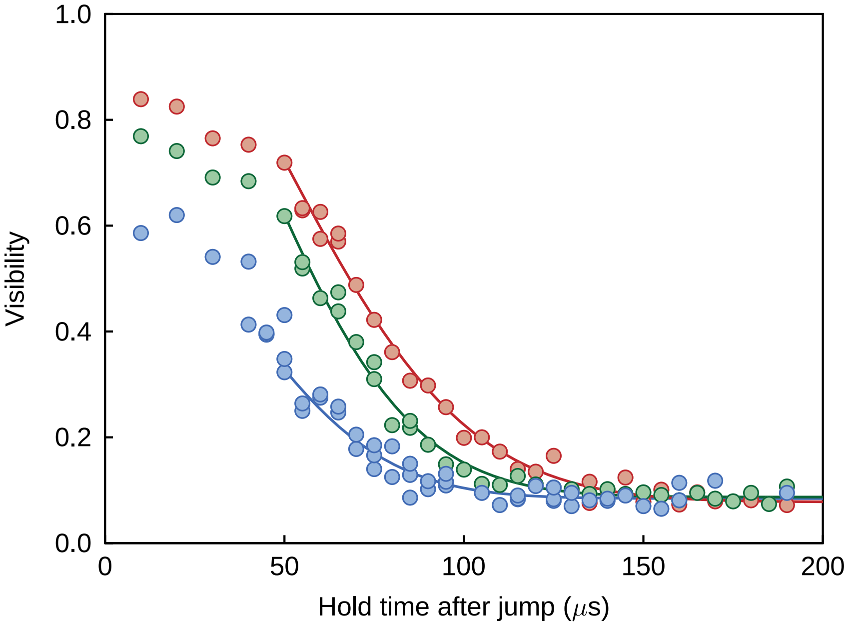

Figure 4.5: Initial collapse of bosonic matterwave in the presence of fermions, at an interspecies scattering length of $0\,a_0$ (red points), $-160\,a_0$ (green points) and $-300\,a_0$ (blue points). The lines are Gaussian fits to the data for $t > 50\,\mu$s.

number can be related to the Gaussian FWHM via equation 4.8. We shall now make use of this relation in order to investigate the effect of interspecies interactions on the atom number distribution in the optical lattice. To this end, we use the Feshbach resonance described in section 1.5 in order to tune the interspecies scattering length a_{bf} in the dipole trap. The mixture is loaded into a shallow optical lattice. Before triggering the collapse and revival dynamics, we use Raman interaction switching, bringing the potassium atoms in the $|m_F = -\frac{9}{2}\rangle$ Zeeman state, such that the actual phase evolution always takes place at the corresponding background scattering length. We then observe the initial decay of the matter wave field and extract the corresponding time scale via a Gaussian fit. Figure 4.5 shows the experimental sequence, together with exemplary results. The time scale is found to decrease significantly for increasing interspecies attraction, pointing to a larger variance of the occupation number, associated to an increasing mean occupation number under the assumption of a poissonian distribution, according to equation 4.8. For large attractive interactions, however, we find a significantly reduced initial contrast of the matterwave interference pattern, while at the same time, the goodness of fit for the Gaussian model of the revival peak decreases. Although such deviations could also be caused by multi-orbital effects as demonstrated in section 4.6, the fact that the effective width decreases instead of increases can be interpreted as evidence for the onset of a sub-poissonian number state distribution.

4.4 QPD at varying interspecies scattering length

In order to extend our analysis beyond the simple all-black-and-white experiment presented in section 4.2, we use an experimental sequence which is essentially the inverse of the procedure used in the previous section. We start out by preparing the potassium atoms in the $|F = \frac{9}{2}, m_F = -\frac{7}{2}\rangle$ state by means of radio-frequency RAP. We then apply a magnetic field such that the interspecies scattering length in the resonant channel can be tuned. Next, we load the non-resonantly interacting mixture into the shallow optical lattice. Right before the jump in lattice depth, we make use of rapid Raman interaction switching in order to bring the Potassium atoms into the resonant collision channel. This way, we ensure equivalent initial states for all experimental runs, maintaining at the same time the ability to measure QPD dynamics at varying interspecies interaction strength. The results of this experiment can be seen in figure 4.6.

4.5 Probing co-occupation of sites by heterodyne QPD

An intriguing feature in the outcome of the experiment shown in figure 4.6, is the modulation of the revival amplitudes, depending on the interspecies interaction. This effect can nicely be seen in figure 4.7, where we directly compare QPD traces for interspecies scattering lengths of $a_{bf} = -55\,a_0$ and $a_{bf} = -85\,a_0$, respectively. To understand the mechanism behind this suppression, we have to relax our initial assumption, that bosons always sit together with fermions. Instead, we assume that the optical lattice contains two kinds of sites: The ones that are occupied by a fermion and those that are not. Clearly, these two subsystems experience different time evolutions. This is true even within the single-band Bose-Fermi-Hubbard model, due to the interspecies interaction term. As we now have two different subsystems, the linear time evolution becomes measurable, as a difference in the global

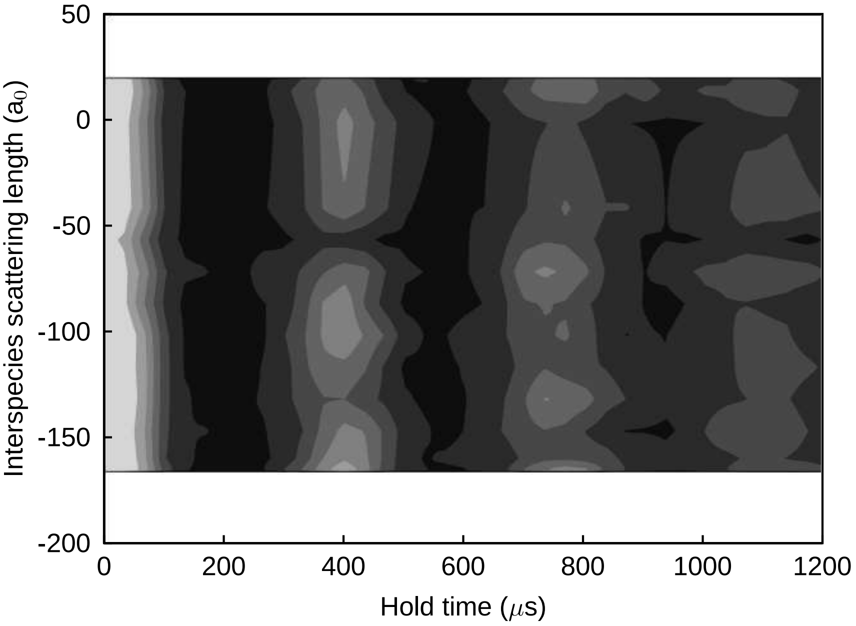

Figure 4.6: QPD dynamics for varying interspecies interaction strength. Bright and dark areas indicate high and low visibility of the interference pattern, respectively. The experimental data has been interpolated linearly along the scattering length axis. For this series of measurements, the mixture system is prepared in the nonresonant $|m_F = -\frac{7}{2}\rangle + |m_F = 1\rangle$ channel, and rapidly transferred to the resonant channel via Raman interaction switching right before the QPD dynamics is triggered. Depending on the interspecies scattering length, a suppression of the first (second, third) revival can be observed.

phases of the two systems. Figure 4.8 shows the Q-function within the single-band Hubbard model, for the two subsystems as well as the whole system[2]. It is thus possible to reproduce a strong suppression of any of the revival peaks depending on the choice of parameters, i. e. the relative weight of the two subsystems, and the ratio of the interspecies and intraspecies interaction strengths. More explicitly, a suppression of the first revival takes place if the timescale of the dephasing between the two subsystems is close to the revival time $t_r = \frac{h}{U}$ of the individual systems. The differential phase between the subsystems is given by

$$\phi(t) \approx e^{-\frac{i}{\hbar} V_{bf} \bar{n}_b t}, \tag{4.10}$$

---

[2] The Q-function is defined on the phase space of the system and can therefore easily be defined for mixed states, see e. g. [113].

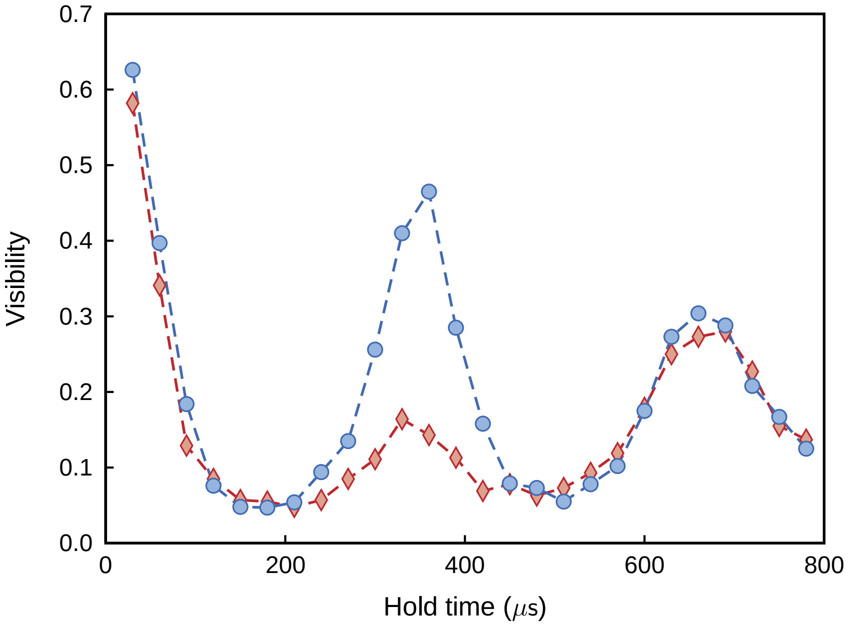

Figure 4.7: Suppression of the first revival peak. The measured points correspond to $a_{bf} = -55\,a_0$ (red diamonds, first peak strongly suppressed) and $a_{bf} = -85\,a_0$ (blue circles, usual damping). Both traces were recorded after a $50\,\mu$s lattice depth jump from 7 to $32\,E_r$ for Rubidium, using Raman interaction switching into the resonant channel right before the jump.

leading to the suppression condition

$$U_{bb} \approx 2\,V_{bf}\bar{n}_b. \tag{4.11}$$

Inserting the standard expressions for the interaction energies, we obtain the condition

$$\frac{a_{bf}}{a_{bb}} = \frac{1}{2\,\bar{n}_b} \cdot \frac{\mu_{bf}}{\mu_{bb}} \cdot \gamma, \tag{4.12}$$

where μ_{bb} and μ_{bf} are the respective reduced masses, and γ is the ratio of the density overlap integrals, with $1.0 < \gamma < 1.5$ for the parameters of this experiment. Inserting numbers, we find that the experimentally observed ratio of $\frac{a_{bf}}{a_{bb}} \approx \frac{1}{2}$ is consistent with our model, if we assume low Rubidium filling $\bar{n}_b < 1.5$ for these measurements. The peak suppression can therefore be identified with the relative evolution of the global phase of the two subsystems. In a sense, this experiment can thus be considered a heterodyne measurement of the Bose-Fermi interaction, where the lonely bosons serve as a reference clock.

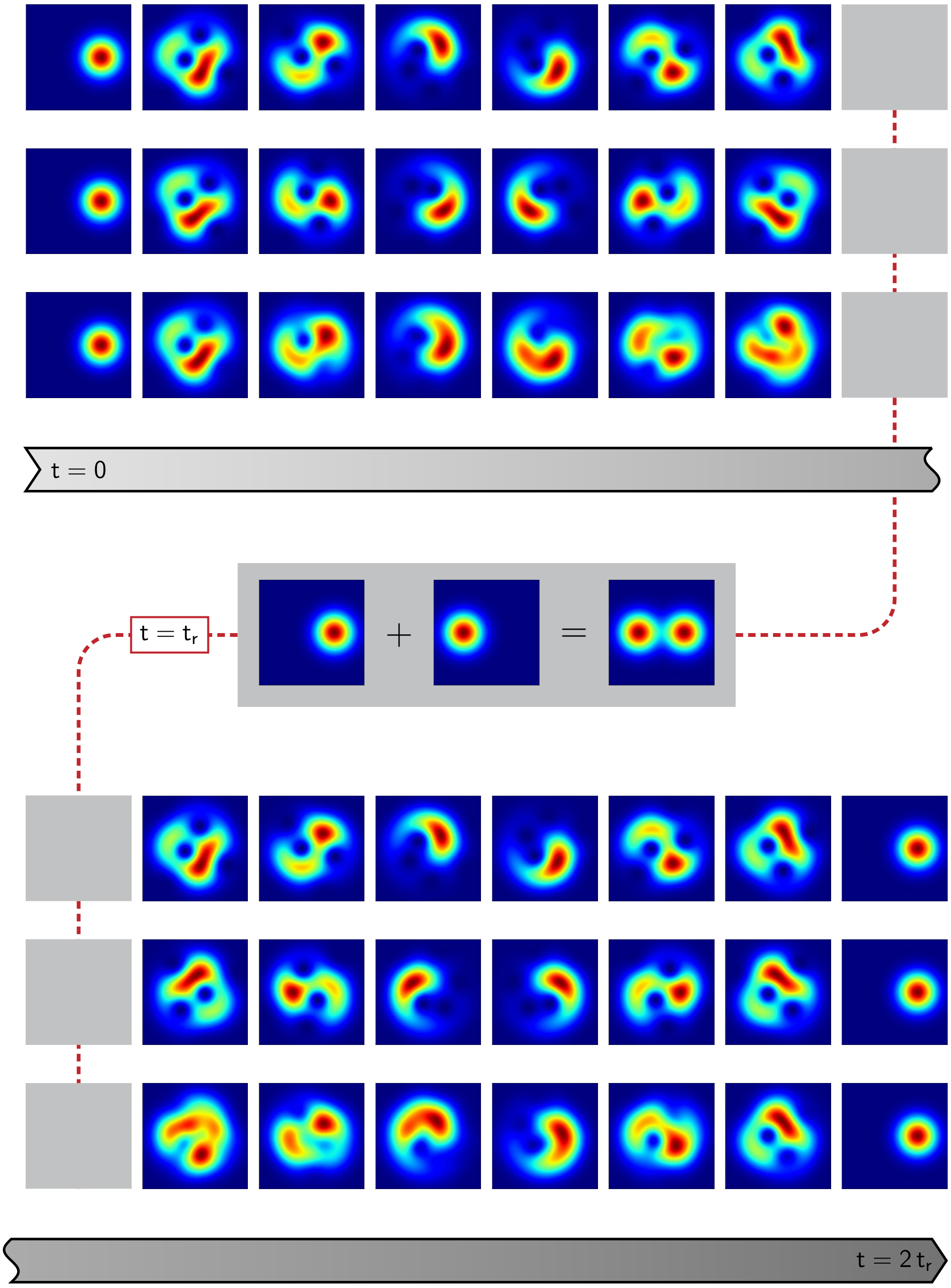

Figure 4.8: Mechanism behind the suppression of revivals in the Q-function picture. The rows represent the subsystems with (upper) and without (middle) fermions, and the total (mixed) system (lower).

4.6 Analysis of Fourier components

So far, we have only looked at the average interaction energy, and its modification by the presence of a fermion. However, it is clear from the considerations in the previous chapter that the interaction energy will also depend on the boson number. This is even true for a pure bosonic sample, where we were able to make use of this fact both for a direct observation of number squeezing as a precursor of the superfluid to Mott insulator transition and the verification of the numerical accuracy of exact diagonalization calculations in our system [157]. The details of this analysis are beyond the scope of this work, and we will here restrict ourselves on applications to mixtures. More details about this and related topics can be found in reference [155].

If we assume that the interaction energies for different boson numbers are in general not integer multiples of the two-boson interaction energy, we expect a dephasing of the collapse and revival signal in the QPD experiments on a time scale related to the difference frequencies. Clearly, the experimentally observed damping could be caused partially by such a dephasing, provided that the frequency differences would be on the order of 10% to 30% of the average frequency. By carefully adjusting the dipole trap depth during the jump, and thus eliminating additional inter-site dephasing due to spatially varying energy offsets, we can extend the timetraces of the QPD dynamics to significantly longer timescales, such that we can observe several tens of revivals. For the right choice of parameters, we can thus obtain a clear signature of a beating between multiple frequencies in a pure bosonic sample, which can be verified using a discrete Fourier transform of the trace, see upper part of figure 4.9. Once established on the pure bosonic sample, this method of analysis can be extended straightforwardly to the Bose-Fermi mixture. The experimental sequence is very simple, with the lattice loading and the QPD dynamics taking place at the same scattering length. The traces are recorded over a timescale of typically 6 ms, and then subjected to a discrete Fourier transform. The result of this experiment can be found in figure 4.9, where we compare the Fourier spectra obtained for a jump in lattice depth from 6 to $32\,E_r$, with and without Fermions present. The first thing to observe is the occurence of additional frequency components of order $\mathcal{O}(U_{bb})$, at frequencies larger than those measured in the pure bosonic case. These correspond to the modification of the interboson interaction energy U_{bb} by self-trapping, as observed previously already for the *average* interaction energy (see figure 4.4). Secondly, there appears an additional frequency component at a frequency significantly lower than the U_{bb} components, corresponding to about one third of the mean bosonic interaction energy in the situation shown in figure 4.9. In the timetrace,

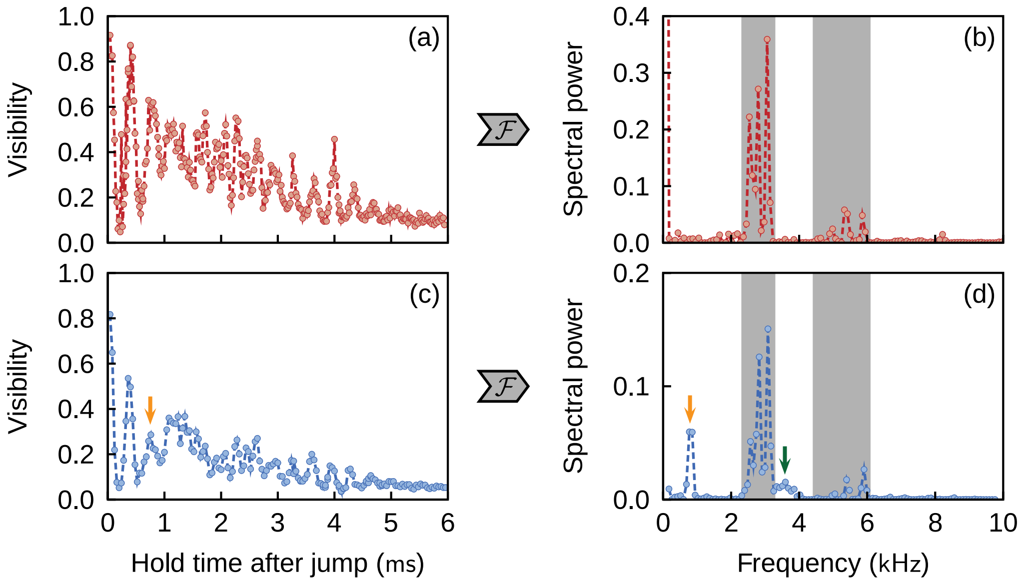

Figure 4.9: Multiorbital structure revealed in long traces of QPD dynamics. Long QPD visibility trace (a) and corresponding Fourier power spectrum (b) for a pure Rubidium system. The spectrum essentially consists of two groups of features, at frequencies of order $\mathcal{O}(U)$ and $\mathcal{O}(2\,U)$, marked by the shaded areas. (c) Long QPD trace in the presence of fermions, at an interspecies scattering length $a_{bf} = -115\,a_0$. Besides the stronger damping of the dynamics, a significant suppression of the second revival peak (indicated by yellow arrow) is clearly visible. (d) Fourier power spectrum of the mixture QPD trace. The most prominent new features are the suppression peak (indicated by the yellow arrow) and new spectral components above the $\mathcal{O}(U)$ spectrum (green arrow). Note that the vertical axis has been enlarged by a factor of two with respect to (b) in order to compensate for the stronger damping. The DC component has been removed from both spectra for clarity.

this feature corresponds to a modulation of the QPD signal on a timescale of several revivals. Both from the observed frequency and by direct inspection of the timetraces, we can identify this extra modulation with the peak suppression observed in the previous section. Thereby, the frequency of this peak is related to the difference in the time evolution between the bare bosonic and the mixed Bose-Fermi subsystems. This spectral feature thus allows, at least in principle, to extract the interspecies interaction energy. In order to verify this assumption, we compare the Fourier spectra for different values of the interspecies scattering length in figure 4.10. We observe a shift which increases linearly with the interspecies scattering length within the measurement precision. We therefore conclude that this frequency component is a direct signature of the differential global phase for the two subsystems with and without fermions, as explained in the previous section.

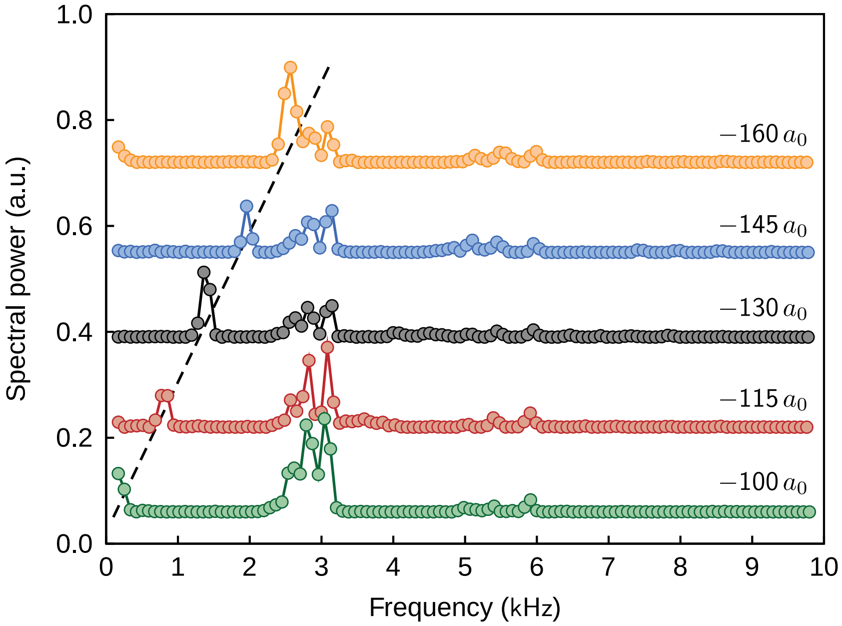

Figure 4.10: Fourier power spectra of QPD traces for mixtures of varying interspecies interaction strength. The individual traces are vertically offset by an amount corresponding to the individual interspecies scattering length, as indicated with each trace. Besides the group of spectral features of order $\mathcal{O}(U_{bb})$ and $\mathcal{O}(2\,U_{bb})$, an additional strong feature can be observed at smaller frequencies. This peak, which shifts with interspecies scattering length approximately linearly (dashed line), is identified with the peak suppression feature observed earlier, and can be explained as the differential phase shift between the subsystems with and without fermions. The DC component has been removed from all spectra for clarity.

Five

Role of interspecies interactions in the many-body system

We investigate the loading of an interacting mixture of quantum gases into a threedimensional optical lattice. It is shown how the many-body dynamics is modified due to renormalization effects and changes in filling demonstrated earlier. The main results of this chapter have been published in reference [12].

5.1 Symmetry between attractive and repulsive interactions

For a homogeneous system[1], it is to be expected from the arguments given in the previous section that the system behaves identically for both attractive and repulsive interactions. However, there are several *caveats*, all of which can play a role in the real system, namely:

- Non-linearity of the Bose-Fermi interaction strength V with respect to the interspecies scattering length a_{bf}, due to the self-consistency condition on the interacting Wannier functions, as described in section 3.2.

- Change of the interboson repulsion U with a_{bf} due to self-trapping, as discussed in section 3.2.

- Modified effective tunneling due to interactions. The effective potential is increased for attractive interactions, while it is decreased for

---

[1] Note that a homogeneous system is understood to be infinite.

repulsive interactions. Clearly, this also means that an effective exchange interaction, of the form $J_{ex} = \frac{J^2}{V}$, tends to be significantly weaker for attractive than for repulsive interactions.

- The overal trapping potential (which is confining for fermions, but anticonfining for holes). A very strong trap can therefore break the symmetry, enforcing boson-fermion co-occupation of sites in a repulsive regime where it would be avoided in the homogeneous system.

- The fixed finite atom number (instead of a well-defined filling in the homogeneous case) also breaks the symmetry, provided that $N_b/N_f \gg 1$. This stems from the fact that the interaction energies for a fermion sitting with one, two or three bosons are all different, while from the point of view of a hole, these cases are all degenerate (up to the interboson interaction energy).

We therefore conclude that for the symmetry to be observable, the interspecies interaction needs to be weaker than the interboson repulsion, such that renormalization effects can be neglected. Furthermore, it is necessary that the confining potential in which the mixture is trapped is not too strong, and that the bosonic filling is not too high, in order to preserve the symmetry between particle- and hole-based composite particles.

5.2 Previous experimental work

Recently, degenerate mixtures of bosonic ^{87}Rb and fermionic ^{40}K atoms in three-dimensional optical lattices have been investigated at a fixed attractive background scattering length in two independent experiments [63, 114]. The authors found a shift of the visibility loss of the ^{87}Rb interference pattern towards shallower lattices, which has been interpreted as a shift of the bosonic superfluid to Mott insulator transition[2]. Several mechanisms have been put forward to explain this shift, including those presented in section 3.3; however, none could clearly be identified.

5.3 Experimental sequences

In order to clarify the physics behind the visibility loss, we have prepared a degenerate Bose-Fermi mixture with magnetically tunable interactions.

---

[2] See also reference [26] for related work on a Bose-Bose mixture.

Thereby, we can investigate the coherence properties of the bosonic component in the presence of fermions over a wide range of interspecies interactions, from strongly attractive to strongly repulsive, for varying admixture of fermions. The experiment starts with approximately 4×10^5 ^{87}Rb atoms and up to 3×10^5 ^{40}K atoms in their respective hyperfine ground states $|F = 1, m_F = +1\rangle$ and $|F = \frac{9}{2}, m_F = -\frac{9}{2}\rangle$. The mixture is held in the crossed dipole trap while a homogeneous magnetic field is adiabatically applied in order to address the interspecies Feshbach resonance described in section 1.5. We can continuously tune the interspecies s-wave scattering length a_{bf} between $-170\,a_0$ and $+800\,a_0$ below the Feshbach resonance. After a fast jump over the resonance, we can also address attractive scattering length values between $-800\,a_0$ and $-200\,a_0$. After 50 ms settling time for the magnetic field, a three-dimensional optical lattice is adiabatically ramped up to a final depth in the range of $V_0 = 2 \ldots 17\,E_r$ within 100 ms using an s-shaped ramp, similar to those investigated in reference [53] [3]. The lattice wavelength $\lambda = 755$ nm in this experiment is chosen such that the lattice depths, as measured in units of the respective recoil energies, are equal for both species. This ensures maximum overlap of the single-particle Wannier functions, while the ratio of the tunneling is expected to be given by the mass ratio $\frac{m_f}{m_b}$. After a hold time of 100 ms, which is long compared to the tunneling time for any lattice depth used, all traps as well as the magnetic field are instantaneously switched off[4], and the atom clouds are allowed to expand during 18 ms time of flight. The resulting interference pattern of the ^{87}Rb atoms is recorded using standard absorption imaging. From these images, we extract the contrast in terms of the visibility, defined as in the previous chapter, see equation 4.9.

---

[3] It should be noted that due to the shorter lattice wavelength, in our work, the optimal timescales are expected to be slightly shorter than those reported in reference [53]. On the other hand, the weaker overall confinement necessitates a stronger redistribution of the boson density in our experiment, if we neglect the influence of the fermions. Experimentally, the 100 ms ramp times used in this work were found to produce the least heating.

[4] The shutdown timescales of the optical potentials (mainly due to finite turn-off times of acousto-optical modulators) are negligible, while the magnetic field shows a decay timescale of approximately 400 μs. We can not exclude slight distortions of the cloud shape due to inhomogeneous magnetic forces during this time. However, due to the high quality factor of 2×10^2 of the Feshbach resonance, these effects will essentially be constant over the whole range of our measurement.

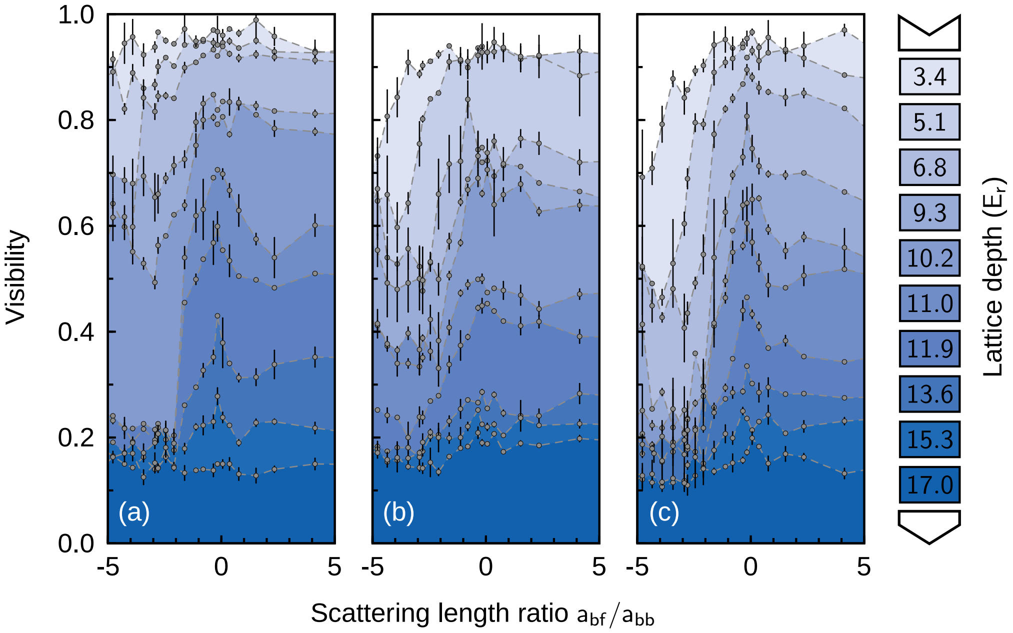

Figure 5.1: Visibility of Rubidium interference pattern, versus interspecies scattering lengths, for (a) high, (b) intermediate and (c) low fermion number. Darker colours correspond to deeper lattices. The points and error bars represent actual measurements. The dashed lines are guides to the eyes.

5.4 Visibility of bosonic interference pattern mixture

By varying both the lattice depth and the magnetic field, we can probe the phases of the mixture. We have analyzed scenarios with low ($N_f \approx 0.25\,N_b$), intermediate ($N_f \approx 0.5\,N_b$), and high ($N_f \approx 0.75\,N_b$) fermion numbers.

In figure 5.1, we show representative profiles of the visibility versus interspecies scattering length, for various values of the lattice depth, and various fermion numbers. For shallow lattices of less than $3\,E_r$, we find a high visibility, which is almost independent of the interaction strength. Also, for deeper lattices, at $a_{bf} \approx 0$, we recover a monotonic decay of the visibility versus lattice depth compatible with the superfluid to Mott insulator transition in a pure ^{87}Rb sample [52, 51]. This demonstrates that the fermion cloud becomes fully transparent for the bosons. For small absolute values of a_{bf}, we observe a decrease of visibility which is symmetric around $a_{bf} = 0$ within our measurement accuracy. This symmetry persists

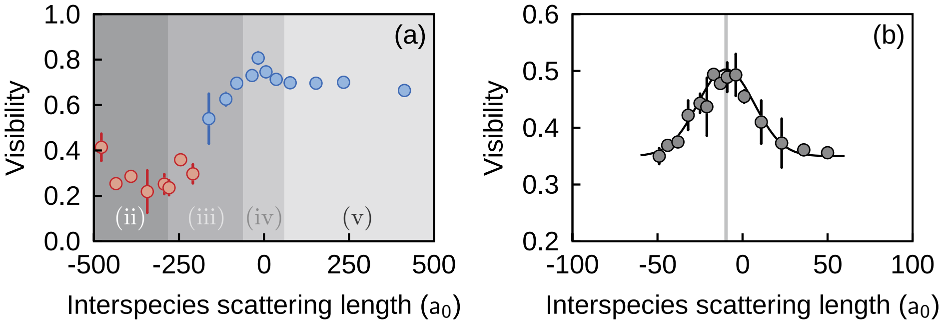

Figure 5.2: Visibility of Rubidium interference pattern for high Fermion numbers, versus interspecies scattering lengths. (a) Individual visibility trace at a lattice depth of $9.3\,\mathrm{E_r}$. The red and blue points are taken above and below the Feshbach resonance, respectively. Note that the region very close to the Feshbach resonance, where particle loss is observed in the dipole trap, is located outside the range boundaries of this graph. The shaded regions qualitatively indicate the different regimes discussed in the main text. (b) Detail trace taken at a lattice depth of $11\,\mathrm{E_r}$, illustrating the symmetry of the central feature. The line is a Gaussian fit to the data. The shaded region represents the center position and uncertainty as derived from the fit.

within an interval $|U_{bf}| \leq |U_{bb}|$, where the interboson repulsion is strong enough to effectively hinder bosonic double occupation of sites. Departing from this symmetry peak, we see a further decay of visibility, which is significantly stronger for intermediate attractive than for comparable repulsive scattering lengths. This suggests a fundamental difference in the underlying mechanisms on either side. The behaviour in the vicinity of the attractive background scattering length as we observe it is similar to earlier measurements [63, 114]. Towards very strong attraction, we find a significant loss of bosonic atoms, accompanied by an increase of visibility. For strongly repulsive interactions, the visibility remains almost constant on a high level. This could be an indication that bosons and fermions do not occupy the same lattice sites in this regime, a situation which we shall examine more closely in the following sections. For $a_{bf} > 400\,a_0$, we observe significant atom losses. However, these are found to be essentially independent of the hold time in the lattice, suggesting their occurrence early during lattice loading, when the mixture is held just below the Feshbach resonance, such that the loss channel given by collisional formation of molecules becomes accessible. Based on the observations outlined above, we qualitatively identify five distinct regimes, i. e., (i) lossless coexistence in very shallow lattices for all scattering lengths, and regimes characterized by very (ii) strong interspecies attraction, (iii) intermediate attraction, (iv) weak interaction (of either sign), and (v) very strong repulsion for deeper lattices, where the latter one might be connected with phase demixing of some kind. This classification qualitatively holds for all fermion numbers investigated in this work, although the symmetric feature around $a_{bf} \approx 0$ might be most pronounced for the highest fermion numbers. Figure 5.2 (a) presents an individual visibility profile taken at high Fermion number, with the regimes (ii)-(v) highlighted. In part (b) of this figure, a detail scan of regime (iv) is shown, demonstrating the symmetry of the effect with respect to the sign of interactions in this narrow regime[5].

5.5 Reversibility and the role of loss processes

In order to distinguish dissipative and adiabatic effects, we investigate the reversibility of the visibility loss. For a dissipative process, we expect the loss be irreversible, while any adiabatic effect can in principle be undone when the dynamics is reversed. It should be pointed out in this context that adiabatic heating effects as considered in reference [30] are expected to be perfectly reversible, as they only arise from the modification of the density of states during the lattice rampup. In the experiment, we characterize the reversibility as follows: After the usual hold time in the optical lattice, we ramp back the magnetic field to the value where the mixture becomes non-interacting within 50 ms. After a short additional hold time, we adiabatically ramp down the optical lattice to approximately 8 $\mathrm{E_r}$, in order to obtain a decent degree of visibility. We then consider the visibility improvement, given by

$$\delta v = \frac{v_r}{v_0} - 1, \tag{5.1}$$

where v_r and v_0 are the visibility with and without the ramp-back procedure, respectively. The results can be seen in figure 5.3, together with a sketch of the corresponding ramps. At scattering length of $\pm 100\, a_0$, the visibility loss can be considered mostly reversible for lattice depths of 8.5 $\mathrm{E_r}$ and below. Reversibility is then gradually lost in deeper lattices. At a lattice depth of approximately 15 $\mathrm{E_r}$, the loss is completely irreversible within

---

[5] The small deviation of the symmetry center from zero, of $9.7 \pm 1.0\, a_0$ visible in figure 5.2 is perfectly compatible with the true $a_{bf} = 0$ within the uncertainties of the magnetic field calibration and the parametrization of the Feshbach resonance.

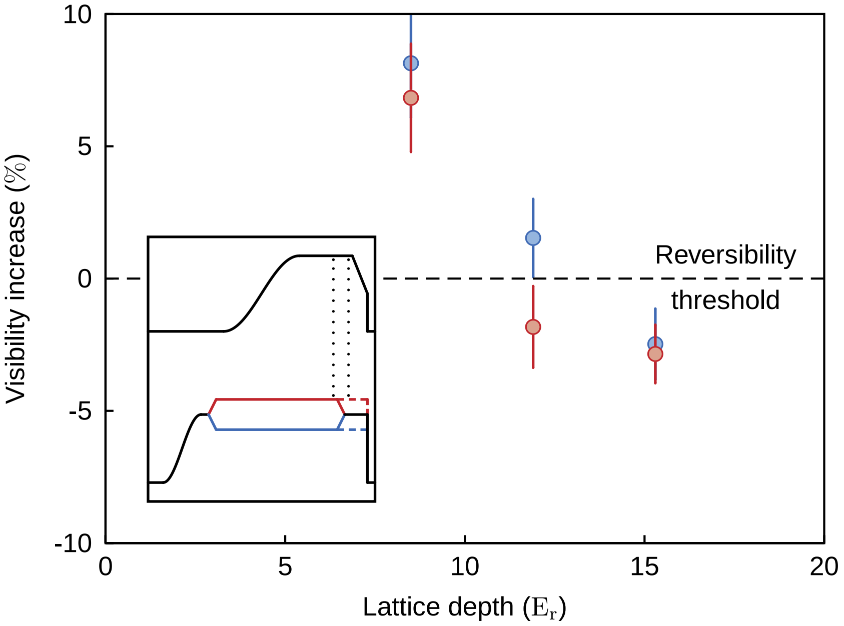

Figure 5.3: Visibility improvement for attractive (blue points) and repulsive (red points) interspecies interactions. The measured points are averaged over typically four independent runs. For lattice depths below approximately 5 E_r, the reversibility is almost perfect within the measurement uncertainty. The inset shows the corresponding ramps of the optical lattice potentials (upper curve) and magnetic field (lower curve). The colors have the same meaning as in the main graph. The dashed lines denote the reference ramps without ramp-back. The dotted vertical lines indicate the end of the usual lattice hold time (left) and the time when the mixture becomes non-interacting (right).

the measurement uncertainty. Such apparent irreversibility can be caused in two very different ways. First, the microscopic dynamics might still be reversible, but the timescales may become so slow that our ramp-back is simply non-adiabatic. As we have only limited flexibility in the ramp-back timescale[6], it is not easy to verify this hypothesis. However, it should be noted that while the single-particle tunneling is fast with respect to our ramp-back, this need not be the case for the effective tunneling in the presence of interactions, and even less, if we consider pair tunneling processes,

---

6) Faster ramps can not be controlled accurately enough due to current ringing, while for signgificantly slower ramps, technical noise and heating become an issue.

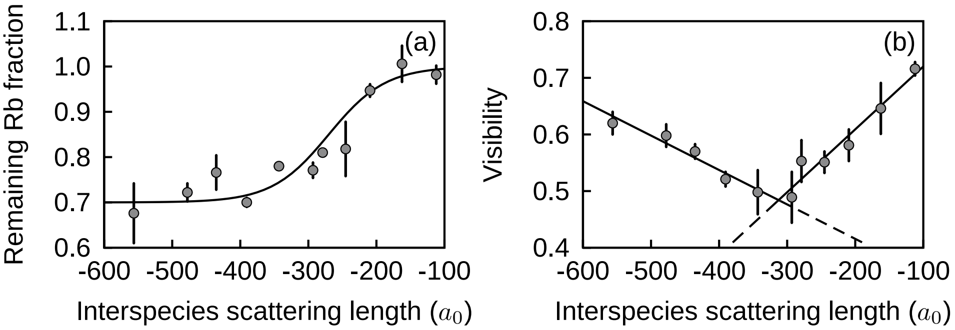

Figure 5.4: Correspondence of visibility increase and boson loss. (a) Experimentally determined visibility minimum and (b) simultaneous ^{87}Rb loss feature at a lattice depth of $9\,\mathrm{E_r}$ for intermediate fermion number. Solid lines are guides to the eye.

which scale as

$$J_{bf} = \frac{JJ'}{V}. \tag{5.2}$$

Although this interaction induced slowing-down of adiabatic time scales (see also [123]) may account for parts of the irreversibility in deep optical lattices, we have to consider the fact that the microscopic dynamics itself may be irreversible. In particular, this is to be expected as soon as particle loss processes become important. Experimentally, we do observe particle loss, mainly of Rubidium atoms, which does not exceed 10% of the particles for most measurements. However, we find that at any given lattice depth, there is a maximum attractive interspecies scattering length beyond which losses become dominant. This *critical* scattering length shows a tendency towards smaller absolute values for deeper lattices. At the same time, we note an increase of the visibility towards very strong attraction, i. e. a visibility minimum around the drop in remaining atom fraction. Despite the visibility increase, no condensate is discernible in the corresponding TOF images. These findings are summarized in figure 5.4. We can extract the value of the scattering length at which the visibility minimum is observed by fitting the decreasing and increasing slope to either site of the minimum and calculating their intersection point. This critical scattering length shows a tendency towards weaker attraction for deeper lattices, irrespective of the fermion number in the system. In fact, there is no systematic difference in the critical values observed at low, intermediate and high fermion number, respectively. This points to the fact that the underlying mechanism can be tracked back to onsite physics exclusively. The correspondence with the increase in Rubidium losses in the vicinity of this minimum reminds of

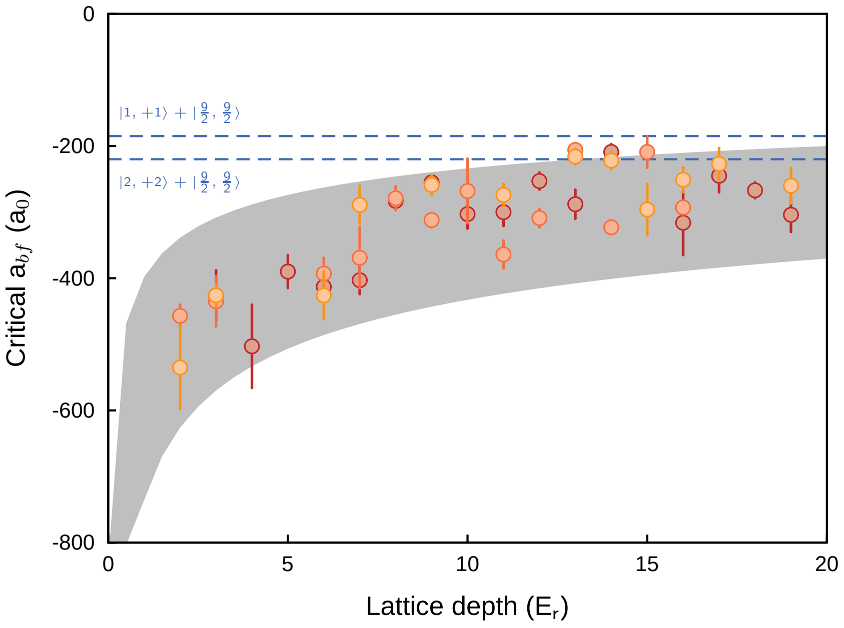

Figure 5.5: Onset of the loss-dominated regime. The points indicate the critical a_{bf} determined from the visibility data, versus lattice depth for high, intermediate and low fermion number N_f (darker colors for higher N_f). The shaded area gives an estimate of the scattering length at which the bosonic three-body loss timescale becomes shorter than the experimental hold time, based on our variational model. The dashed lines indicate the background scattering length for the hyperfine combinations used in this work (upper line) and previous experiments by other groups ([63, 114]), indicating that Feshbach control of interactions might be crucial in order to avoid the loss-dominated regime.

the conjecture in section 3.2, namely that there exists a critical attractive scattering length beyond which the onsite density becomes instable. In the vicinity of this critical scattering length, there is a very strong increase in density and hence in the three-body loss rates. In principle, we may encounter two types of three-body loss processes:

- Loss of two bosons and one fermion.
- Loss of three bosons.

As we find the boson number loss to exceed the fermion number loss by a factor of three to four in our measurements, we believe that the latter process is the dominant one here. The former process should be perfectly allowed though, and should be equally important judging from the densities and the known rate coefficients. However, it should be pointed out that this process has also not been observed in a recent measurement, where the contribution of different occupation numbers to the total loss in the system was identified by the different time scales [63]. Therefore, it is conceivable that the rate coefficient for the former process is in fact smaller than the value given in reference [21].

We shall restrict ourselves to the latter scenario, and try to understand these loss processes using our simple variational model. To this end, we minimize the total onsite energy with respect to the width σ_b and σ_f of the bosonic and fermionic Gaussian density profiles for a given lattice depth V_0 and boson occupation number N, in the presence of a fermion. Recalling that the three-boy loss rate for the bosons is given by

$$\dot{N}_3 = -K_3 \cdot N^3 \cdot \int n_b(\mathbf{r})^3 \, d^3\mathbf{r}, \tag{5.3}$$

where N is the boson filling and $n_b(\mathbf{r})$ is the self-consistent single-particle density, and inserting our variationally determined wave functions, we find that the loss rate scales as

$$\dot{N}_3 \propto \sigma_b^{-6}. \tag{5.4}$$

In other words, an decrease in the width σ_b by 5% will yield one third increase in the loss rate, which doubles for a change in width of as few as 12%.

For practical purposes, a site can be considered lost when $\dot{N}_3 \, \tau \gg 1$, where τ is the experimental hold time. Assuming a loss coefficient for collisions of three ^{87}Rb atoms in the range $K_3 = 4 \ldots 7 \times 10^{-30}\,\mathrm{cm}^6/\mathrm{s}$ [21], we find that lattice sites with four or more bosons will be lost on time scales faster than our hold time even in the absence of fermions. Therefore, we focus our attention on sites occupied by three bosons and one fermion.

The critical scattering length for bosonic three-body losses derived from our variational model shows good agreement with the experimentally observed onset of the loss-dominated regime, as can be seen in figure 5.5. We therefore conclude that for strong attraction, the dominant process is the three-body loss of highly occupied sites enhanced by the interaction-induced density accumulation, commonly referred to as self-trapping [98, 18]. The associated increase of the visibility may be thought of as the removal of strongly localized atoms on highly occupied sites from the system, and thus a reduction of the bosonic filling in the system. The absence of a condensate in this loss-dominated parameter regime hints to the non-equilibrium character of the final system. Therefore, it seems that the strongly attractive

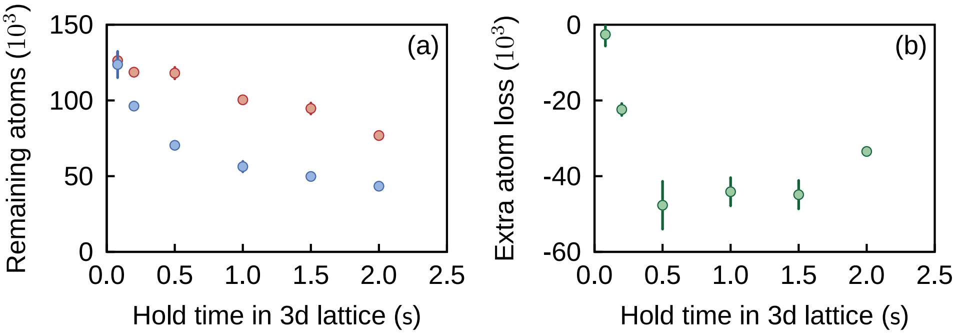

Figure 5.6: Loss of bosonic atoms induced by the presence of fermions. (a) Lifetime of bosons in a deep threedimensional optical lattice with (blue) and without (red points) fermions present. (b) The extra loss, defined as the difference in atom number with and without fermions, saturates on a timescale of less than half a second.

system is not suitable for quantum simulation applications, unless very low fillings (i. e. boson occupation numbers less than two) can be ensured.

The onsite loss model outlined above is further supported by comparative lifetime measurements of ^{87}Rb atoms in a threedimensional optical lattice with or without the presence of fermions interacting through the background scattering length. The result of this measurement is shown in figure 5.6. A clear reduction of the boson lifetime is visible with the fermions present. The extra loss due to the presence of fermions however is found to cease on a time scale of less than half a second, as we would expect for the scenario discussed above.

5.6 Shift of the superfluid to Mott insulator transition

Condensate fraction

So far, we have focussed on the visibility of the bosonic matter wave interference pattern. While this quantity has the advantage that it can be extracted relatively easily both from theoretical calculations and experimental data, its interpretation is not straightforward and has been debated controversely even in the pure bosonic case[7]. Therefore, we move on to a different observable of the experiment, namely the Bose-condensed frac-

---

[7] See the work by Gerbier and coworkers [50] and references therein.

tion. For the homogeneous case, it is known that the condensate in the periodic potential has quasi-momentum zero. As we go to a finite system, we obtain the condensate peak around zero, the width of which is linked to the coherence length in the system. After sudden release from the lattice and time of flight, the condensate atoms can be found in peaks at positions corresponding to $\left(\pm i\frac{\hbar k_x}{m} \pm j\frac{\hbar k_y}{m}\right) \cdot t_{TOF}$, where $i, j \in N_0$. Therefore, we can calculate the condensed fraction in the system by determining the atom numbers $N_{i,j}$ in all peaks as well as the total atom number N_{tot}, yielding

$$\frac{N_c}{N_{tot}} = \frac{\sum_{i,j} N_{i,j}}{N_{tot}}. \tag{5.5}$$

Determination of condensate atom number from peak fits

In our case, the peak atom numbers are obtained from independent two-dimensional bi-Gaussian fits to all first-order peaks. Higher-order peaks can savely be neglected, as the cloud envelope is narrower than the peak separation for the parameter range of interest.

In contrast to the pure bosonic case, where depletion of the condensate occurs predominantly through thermal excitation, we expect to have significant quantum depletion of the condensate in the presence of fermions. The resulting quasimomentum distribution is not known in detail, we therefore do not try to model the complete cloud shape. However, we do know that the envelope is dominated by the Wannier function, and can, to a good approximation, be described by a Gaussian. This envelope is determined from the low-optical density part of the TOF images, i. e., by masking the peaks. After substraction of this envelope, the peaks have a bimodal shape, the narrow and broad component of which represent the condensed and thermal part of the bosonic subsystem. We model the peaks by the sum of two two-dimensional concentric Gaussians, the widths and amplitudes of which can be indepently fitted, i. e.

$$n_{i,j}(x, y) = a_c\, e^{-\frac{(x-x_i)^2}{2\,\sigma_x^2} - \frac{(y-y_j)^2}{2\,\sigma_y^2}} + a_t\, e^{-\frac{(x-x_i)^2}{2\,\tilde{\sigma}_x^2} - \frac{(y-y_j)^2}{2\tilde{\sigma}_y^2}} \tag{5.6}$$

We then use a constrained Levenberg-Marquart type nonlinear regression to fit the above model to neighbourhood regions of the zero- and first-order peaks. Constraints are imposed on all width values during the fitting procedure, which is necessary due to the a priori degeneracy of the coherent and incoherent part of the fitting function. We have verified that all fitting results are well within the constraints imposed at the end of the procedure,

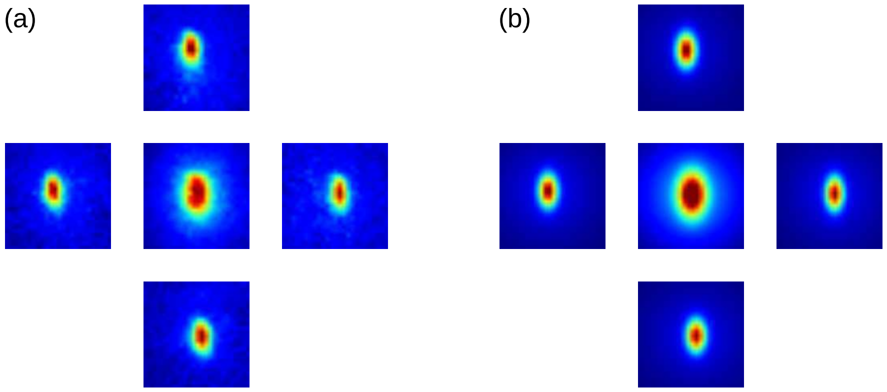

Figure 5.7: Bimodal peak fits. (a) original image data for the center and first order peaks, at a lattice depth of approximately $9\,E_r$ and a weak interspecies attraction of $-35\,a_0$, (b) corresponding fit result. The peak distances are not to scale.

the precise values of the constraints hence do not play a role. For the zero-order peak, it is necessary to exclude regions of optical density $\mathrm{OD} > 2.5$, where the dynamic range of the CCD camera is insufficient to produce reliable image data (so-called *blacking out* effect), from the analysis. The condensate atom number in each peak is then given by

$$N_{i,j} = \pi\, a_c\, \sigma_x\, \sigma_y. \tag{5.7}$$

The total atom number is determined from a sum over all pixels within the image, and corrected for blacking out, using the fitted instead of the recorded optical densities within the blacked-out regions. The fitting result are shown exemplarily in figure 5.7.

Quantum depletion in the superfluid to Mott insulator transition

We can thus obtain the condensate fraction at a given interspecies interaction strength, as we vary the lattice depth. Clearly, as we increase the lattice depth towards the critical U_{bb}/J_b, we observe quantum depletion of the condensate. In the vicinity of the critical lattice depth, the decay of the condensate fraction is found to be linear within the measurement accuracy. Beyond the critical lattice depth, the condensate fraction vanishes. Hence, it is possible to determine the transition point[8], i.e. the lattice depth for

---

[8] Strictly speaking, the notion of a transition point is ill-defined in a finite-temperature system, where the quantum phase transition is smoothed out and no sharp phase

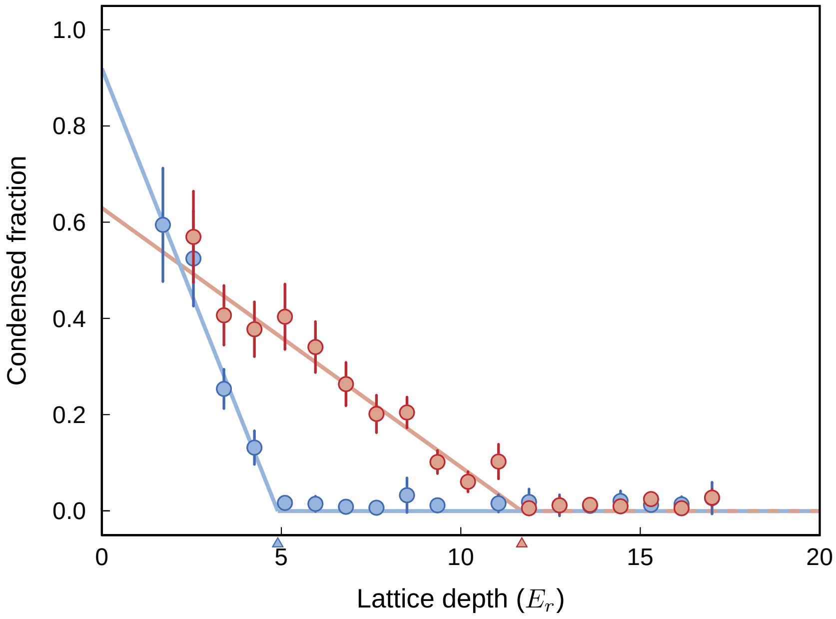

Figure 5.8: Vanishing of the condensate due to quantum depletion in the bosonic superfluid to Mott insulator transition. The blue and red points represent measurements with $a_{bf} = -293\,a_0$ and $a_{bf} = +233\,a_0$, respectively. The lines are linear slope fits to the first points. The triangles on the lattice depth axis indicate the resulting transition points.

which $U_{bb}/J_b > 29.3$, by fitting a straight line to the condensed fraction in shallow lattices, and extracting the intersection point with the $N_c = 0$ axis. The behaviour of the quantum depletion with increasing lattice depth and the extraction of the transition point are shown exemplarily in figure 5.8.

Shift of the superfluid to Mott insulator transition

As can be seen from figure 5.8, the Mott insulator transition may show a pronounced shift in the presence of interspecies interactions. A similar shift has previously been observed in references [63, 114], for a Bose-Fermi mixture interacting at the attractive background interaction. We have evaluated the shift of the transition point obtained for different strengths of the interspecies interaction. For intermediate to high fermion numbers, we ob-

---

boundaries exist between the superfluid and the Mott insulating phase. Also, in the inhomogeneous (i. e. trapped) system, the transition happens at slightly different points depending on the position within the trap. However, these effects can still savely be neglected for the given level of precision of our measurement.

serve a pronounced shift of the transition point towards shallower lattices with increasing attractive interspecies interaction. On the repulsive side however, the data is consistent with no shift at all. This behaviour is to be anticipated if we assume that for the parameters of these measurements, essentially all bosons may sit together with fermions. In the absence of fermions, we expect the formation of a bosonic Mott insulator of filling one at a critical ratio $U_{bb}/J_b \approx 29.3$ [24], which can be calculated using exact diagonalization to correspond to a lattice depth of $12.97\,E_r$. The critical U_{bb}/J_b of a Mott insulator of filling two is unfortunately not known with the same precision from ab initio theory, but we can get a reasonable guess by applying the scaling

$$\left(\frac{U_{bb}}{J_b}\right)_c(\nu) = \left(\frac{U_{bb}}{J_b}\right)_c(\nu = 1) \cdot \frac{2\,\nu + 1 + \sqrt{(2\,\nu + 1)^2 - 1}}{3 + 2\,\sqrt{2}} \tag{5.8}$$

which arises from second-order perturbation theory [150], yielding a critical value $(U_{bb}/HJ_b)_c(\nu = 2) \approx 1.89 \times\ (U_{bb}/HJ_b)_c(\nu = 1) \approx 56.7$ corresponding to a lattice depth of $14.96\,E_r$, which again is calculated using exact diagonalization. In order to understand the observed shift, we will again resort to self-consistent Wannier functions. As we have shown in section 3.2, these give rise to renormalized values for the Bose-Hubbard parameters U_{bb} and J_b, depending on the strength of the interspecies interaction. Clearly, we will also have a renormalized U_{bb}/J_b. If we assume an attractive interspecies interaction, the bosonic Wannier functions will shrink, yielding an increase in U_{bb} and a decrease in J_b, thus, we are left with a strong net increase of U_{bb}/J_b, and therefore will reach the critical value already for shallower lattice potentials. On the other hand, interspecies repulsion tends to spread the Wannier function, which results in decreasing U_{bb} and increasing J_b, thus U_{bb}/J_b decreases and the transition point should be shifted towards deeper lattice depths. The effects can qualitatively be understood using the variational model. However, for a good numerical agreement, we once again have to use exact diagonalization. Figure 5.9 shows the experimental data points for intermediate and high fermion numbers, together with the predictions from the variational and exact diagonalization model. From the comparison to these theory curves, we can also infer the transition from a Mott insulator of filling one for weak interspecies interaction, to a Mott insulator of filling two for stronger interspecies attraction. Here, we encounter the same filling increase, which we have observed more directly in the quantum phase diffusion measurement in figure 4.5, albeit in a true strongly correlated many-body scenario.

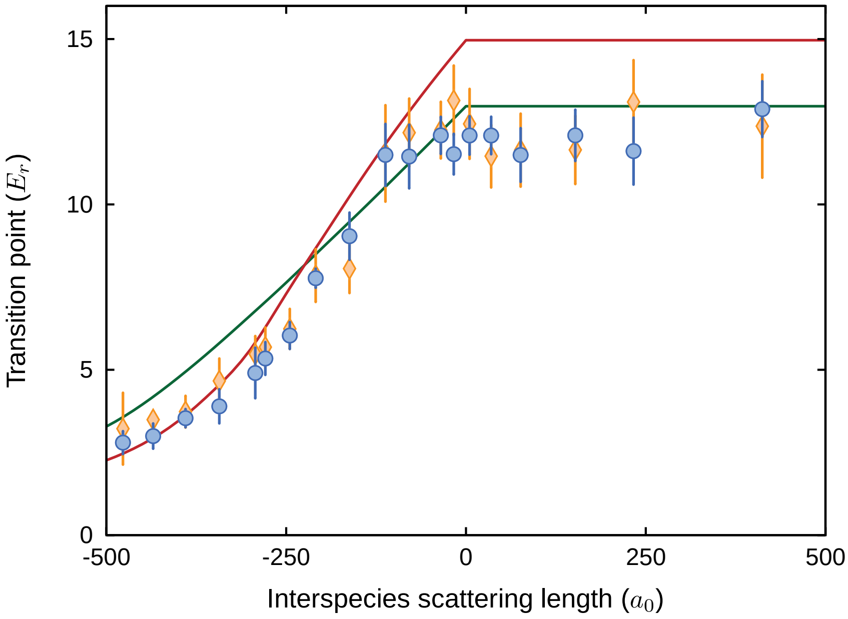

Figure 5.9: Shift of the Mott insulator transition with interspecies scattering length. Blue circles and yellow diamonds indicate the experimentally determined critical point (see also 5.8), for high and intermediate Fermion numbers, respectively. The error bars indicate the uncertainties from the slope fits described in the main text. The solid lines indicate exact diagonalization results for the critical points incorporating the renormalization of both tunneling and interboson repulsion, for the case of boson fillings $n_b = 1$ (green line) and $n_b = 2$ (red line) on the attractive side. On the repulsive side, the lines indicate the non-interacting result, which would correspond to a demixing scenario for repulsive interspecies interactions.

5.7 Phase demixing

Evidence for phase demixing

Theories based on renormalization due to self-consistent Wannier orbitals predict that as interspecies interactions become repulsive, the onsite densities spread out, leading to decreased effective interaction energies and increased tunneling rates for the bosons. By this argument, we would expect a shift of the bosonic Superfluid to Mott insulator transition towards deeper lattice potentials. However, no significant shift is observed in the experiment for repulsive interspecies interactions. As only the strength of the effect, but not the qualitative behaviour depends on the calculational method employed, this suggests that the basic assumption underlying this

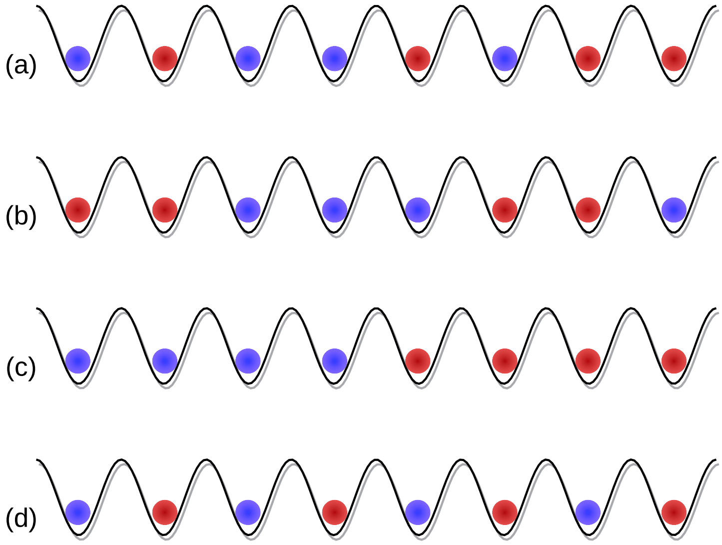

Figure 5.10: Possible scenarios for phase demixing. (a) Fully disordered state, particles avoid each other locally. (b) Domain formation. (c) Macroscopic phase separation. (d) Density wave.

kind of models breaks down for sufficiently strong interspecies repulsion, namely that bosons and fermions do no longer occupy the same lattice sites. The saturation behaviour observed in the visibility data over a wide range of lattice depths could also be explained by this hypothesis. Thus, we have strong evidence for a phase demixing at sufficiently strong interspecies repulsion, where the visibility data suggest that the *critical* interaction strength could be around $U_{bf} \approx U_{bb}$.

Demixing scenarios

Assuming that in the case of very strong interspecies repulsion, bosons and fermions tend not to occupy the same lattice sites, we have to ask ourselves what the resulting particle distribution looks like. A couple of scenarios are conceivable and have been discussed previously in the literature. It should be pointed out that all of these suggestions have neglected the presence of an external trapping potential, which may very well tip the scales in favour of one or the other scenario. The suggested phases can be categorized as follows (see figure 5.10 for a schematic representation):

- Disordered phase. Bosons and fermions are arbitrarily placed on lattice sites, with no regard to the neighbouring sites. This phase should be entropically favoured for $J \ll k_B T \ll U_{bf}$.

- Clustered phase. For finite tunneling, it is favourable to delocalize particles over a few neighbouring lattice sites. This may result in clustered phases, as has been described in [105].

- Macroscopic phase separation. This is the phase separation scenario encountered most often in the case of inmiscible fluids in the macroscopic classical world.

- Density wave phases. At sufficiently low temperatures, ordering might occur, giving rise to a density wave, i. e. an extra density-density correlation at a length scale larger than the lattice spacing. In the extreme case, this state might consist of an alternating occupation of lattice sites by a boson and a fermion, in the 3D analogon to a checkerboard pattern. However, there may also exist smaller amplitude density modulations. It should be noted that this kind of ordering relies on an effective interaction between neighbouring sites, similar to the case of antiferromagnetism, where the quantum-mechanical spin exchange interaction takes this role. A particularly interesting representative of this class of phases is the supersolid, which can be thought of as a superfluid coexisting with a density wave structure.

From the data presented so far, it is not possible to distinguish between the aforementioned scenarios. However, we can most probably exclude a density wave phase on the basis of theoretical arguments. This phase is supposedly quite sensitive to the filling in the system. As we observe demixing for any number of fermions in the system, this would probably spoil the emergence of the density wave.

While all the other phases should still be possible, we strongly suspect macroscopic phase separation to take place, as it is promoted by the external trapping potential. Clearly, there is a finite differential sag between the two components for the parameters of the experiment, albeit significantly smaller than the respective cloud sizes. If we assume that bosons and fermions repel each other, it is easily conceivable that a further separation of their respective centers of mass occurs along the vertical direction. In the limit of infinitely strong repulsion, this might result in a situation where the fermion cloud *floats* on top of the boson cloud due to its lower specific weight. This scenario would in a sense be equivalent to the classical phase separation between two inmiscible fluids inside a container, like water and oil in a glass, where the lighter componenent floats on top of the heavier one.

The two-dimensional situation

Fortunately, it is possible to suppress this kind of macroscopic phase separation by going to an effective two-dimensional system. This can easily be achieved by applying a very deep optical lattice in the vertical direction, such that tunneling is effectively suppressed on the relevant time scales of the experiment, and the clouds are sliced into several mutually decoupled disk-shaped systems. In this case, phase separation is only possible within the disks. Therefore, global phase separation is suppressed as it would require a spontaneous breaking of the rotational symmetry. To realize such a situation in the experiment, we first tune the interspecies scattering length in the dipole trap as we did before. Then, we ramp up the vertical optical lattice to a $V_0 = 45\,E_R$ in 100 ms in order to slice the cloud into independent horizontal planes. Next, we ramp up the horizontal optical lattices to $V_0 = 8\,E_R$ in 100 ms. After a hold time of 50 ms, we release the atoms from the trap. We then evaluate the visibility of the TOF images recorded along the vertical axis. The result of this measurement is shown in figure 5.11. While an asymmetry between attractive and repulsive interaction remains (which might again be due to renormalization effects), we now observe a clear decrease of visibility for strong repulsive interspecies interactions. This suggests that demixing does not occur in the two-dimensional case, which supports the interpretation of gravity-promoted global phase separation in the three-dimensional case as outlined in the previous paragraphs.

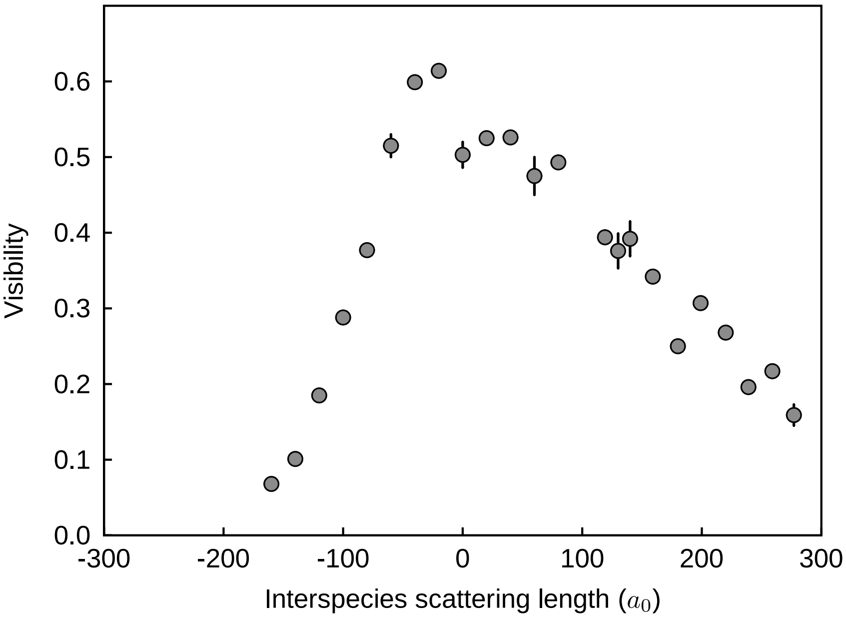

Figure 5.11: Visibility decrease with increasing attractive or repulsive interspecies interaction, as observed in an effective two-dimensional horizontal disk-shaped system, for lattice depths of $V_0 = 8(45)\,E_R$ in the horizontal and vertical directions, respectively.

Six

An outlook

The experiments described in this thesis have important implications for future research on mixed-, but also on single-species quantum gases. On the one hand, the correlation analysis of atomic shot noise, which was demonstrated here for the first time for fermionic atoms in an optical lattice, is an important new tool that may be very helpful to reveal interesting ordering phenomena, as was already demonstrated in the case of bosons [48]. Also, the demonstrated tunability of interspecies interactions which allows to dynamically make the components of the mixture perfectly transparent to each other, promises to be useful for quantum simulation, e.g. in the sense of tunable impurities [18].

Yet, especially in the context of quantum simulation of complex many-body systems, the renormalization effects manifest in this thesis impose a serious *caveat* on the exploration of phase diagrams, especially when quantitative results for the phase boundaries in terms of experimental parameters are requested. Clearly, the mapping between experimentally controllable *knobs* and the model parameters of the Hamiltonian in question can be far more complicated than previously anticipated, and an interesting, yet complicated interplay between different parameters may arise. In the Bose-Fermi-Hubbard example considered in the last chapter of this thesis, this is the case for the interboson repulsion U_{bb} and the boson tunneling J_b, which both react strongly to a tuning of the interspecies scattering length a_{bf}, contrary to the usual assumptions. On the other hand, the effective many-body character of the onsite interactions which was pointed out in reference [79], might be considered an interesting target of quantum simulation in its own right.

The results obtained in this thesis also indicate a strong dependence of the atom number statistics on interspecies interactions. A more detailed analysis of these effects in a spatially resolved way would clearly be desirable, which might be possible along the spirit of previous quasi-tomographic investigations [49, 22], or using the recently developed concepts of *in situ* imaging with singe-site resolution, by means of optical [7, 8] or non-optical probing [50, 159]. This would be even more interesting as many interesting many-body states are very sensitive to the filling fraction and could thus exist locally in a trapped system, yet be hard to detect without the coresponding spatial resolution.

So far, we have not been able to observe any of the more exotic quantum phases predicted in the context of a Bose-Fermi Hubbard model, such as charge density waves or supersolidity, which would demonstrate an effective next-neighbour interaction in the optical lattice mediated by the other species (see e.g. reference [20]). Besides the aforementioned possibility that due to the inhomogeniety introduced by the external trap, these phases exist locally and ask for more sophisticated detection schemes, other reasons are also conceivable. Little is known in general about their chances of survival at finite temperature, or in the presence of particle loss processes. It is therefore possible that further entropy reduction of the mixture is necessary in order to be able to observe such delicate quantum phases. Finally, there is an ongoing search for suitable observables, as some of the proposals made so far are not practical. One example here would be the detailed shape of shot noise correlation features or interference patterns, which to date are still very much limited by the finite imaging resolution, finite time of flight, or residual collisions in the inital expansion phase.

One way of circumventing some of these problems would consist in moving from threedimensional to twodimensional systems living in horizontal planes, e.g. by slicing the cloud with a deep vertical optical lattice, such that tunneling in the vertical direction is efficiently suppressed on the timescale of the experiments. In the horizontal direction, the effective trap frequency in the radial direction can then be lowered in order to make the system even more homogeneous. One obvious drawback inevitable in this case is the fact that only one species can presently be imaged along the vertical symmetry axis in every experimental run, whereas the other species would have to be imaged from the side, which would probably yield less useful information. However, we are convinced that the investigation of twodimensional systems will yield interesting insight, and enhanced chances of observing exotic quantum phases, especially given that the phase separation mechanism driven by gravitation is suppressed in this constellation.

Finally, we would like to point out one interesting direction for future experiments, which arises from consideration of the tunneling ratio between the species, as depicted in figure 3.3. If we assume an effective twodimensional system, in which tunneling in the vertical direction is effectively suppressed, and now choose different wavelengths for the x- and y-lattice axes, respectively (e.g. 730 nm vs. 760 nm, then at a given lattice depth for one species (i.e. the same in both horizontal axes), the other species can only move along one axis (but relatively fast), or *vice versa*. Thus, effectively, the one component would essentially only be able to move along a onedimensional tube, yet, the other species could couple these tubes on an intermediate timescale, with a coupling possibly tunable via the interspecies Feshbach resonance. Also, less extreme versions of this constellation are conceivable, where both species have the same tunneling timescale along one axis, but vastly differing ones along the other axis.

The door to the field of Bose-Fermi mixtures in optical lattices has just been pushed open. We may expect the significantly larger parameter space compared to the single-species case to contain a large variety of many-body phenomena as yet undiscovered, including, but not limited to the scenarios listed in section 3.3.

Appendix

A: Some properties of ^{87}Rb and ^{40}K atoms

Atomic mass	86.909	39.964	amu
Natural abundance	27.8	0.012	%
Nuclear spin	$\frac{3}{2}$	4	
Ground state electronic configuration	(Kr)(5s) $5\,S_{1/2}$	(Ar) (4s) $4\,S_{1/2}$	
Ground state hyperfine splitting	6.835	1.286	GHz
D1 resonance wavelength	794.979	770.109	nm
D2 resonance wavelength	780.241	766.702	nm
D1 resonance frequency	377.107	389.286	THz
D2 resonance frequency	384.230	391.016	THz
D1 natural line width	5.750	5.944	MHz
D2 natural line width	6.067	6.020	MHz

Table 1: Properties of Rubidium 87 and Potassium 40 isotopes (adapted from references [143] and [92])

B: Hyperfine structure in magnetic fields

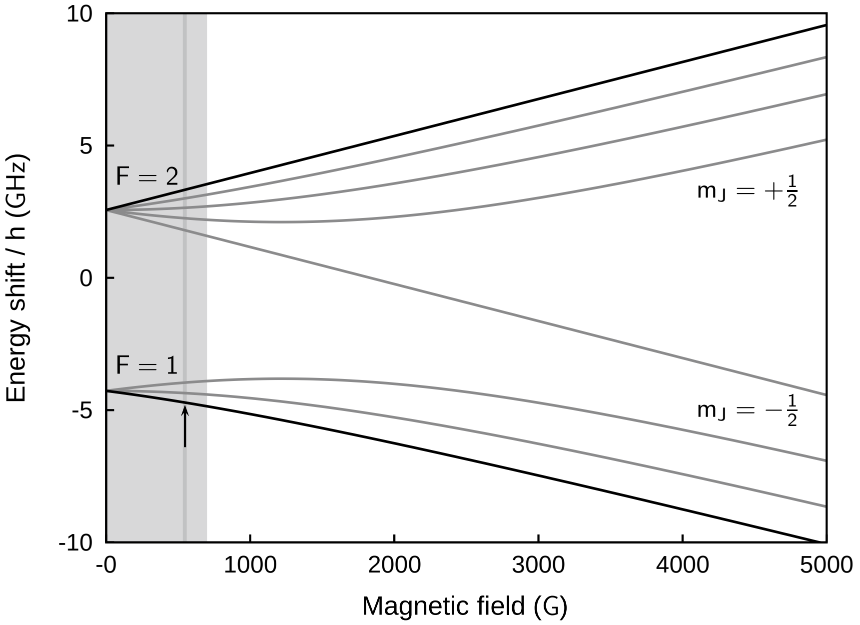

Figure 1: Breit-Rabi diagram for ^{87}Rb. The experimentally accessible range of magnetic fields (lightly shaded area) lies well in the linear Zeeman regime. The black curves correspond to the states of interest in the experiment, namely the uppermost $|F = 2, m_F = +2\rangle$ state (for laser cooling, magnetic trapping and absorption imaging) and the absolute ground state $|F = 1, m_F = +1\rangle$, which is used for most of the actual measurements. This state features the interspecies Feshbach resonance marked by the black arrow. The actual range of magnetic fields used to tune the interspecies scattering length in the vicinity of this resonance lies well within the shaded bar, demonstrating the need for excellent field stability.

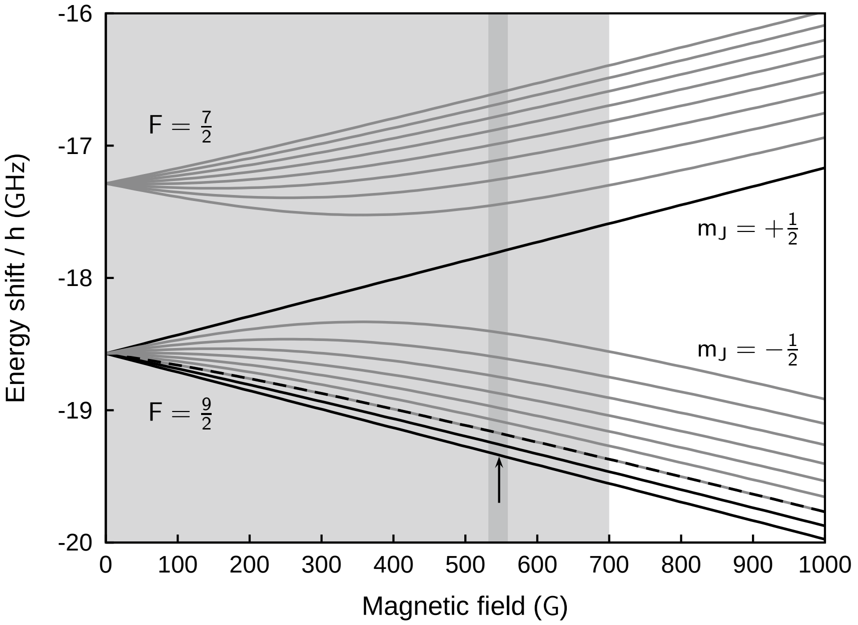

Figure 2: Breit-Rabi diagram for ^{40}K. The experimentally accessible range of magnetic fields (lightly shaded area) and also the tuning range (dark shaded area) around the interspecies Feshbach resonance (marked by the black arrow) in the absolute ground state $|F = \frac{9}{2}, m_F = -\frac{-9}{2}\rangle$ reach well into the hyperfine Paschen-Back regime. Beside the lowermost state, the experimentally interesting states are the $|F = \frac{9}{2}, m_F = -\frac{-7}{2}\rangle$ (second-lowest, used for radio-frequency molecule association and Raman interaction switching, as well as the actual field calibration spectroscopy), and the $|F = \frac{9}{2}, m_F = -\frac{+9}{2}\rangle$ (uppermost state of lower hyperfine manifold), which is used for laser cooling and magnetic trapping. The $|F = \frac{9}{2}, m_F = -\frac{-5}{2}\rangle$ state (dashed curve) is useful in the context of experiments on fermionic spin mixtures, which are beyond the scope of this thesis, see e.g. [137] and references therein.

C: Laser systems for cooling and imaging

Laser system for cooling ^{87}Rb and ^{40}K atoms. (a) The light is derived from external-cavity Littrow-type diode lasers which are referenced to saturated absorption frequency modulation spectroscopy setups for both species, either directly, or via offset frequency locking. A slave laser diode and three tapered amplifier systems help to boost the available output power. (b) The laser beams that serve analogous purposes for the two species are combined into a common single-mode polarization maintaining optical fiber, thereby largely reducing the need for alignment on the experiment side. Lossless overlapping of the two beams is achieved using special waveplates, which only turn the polarization for one of the two wavelengths in question, while leaving the other unaffected.

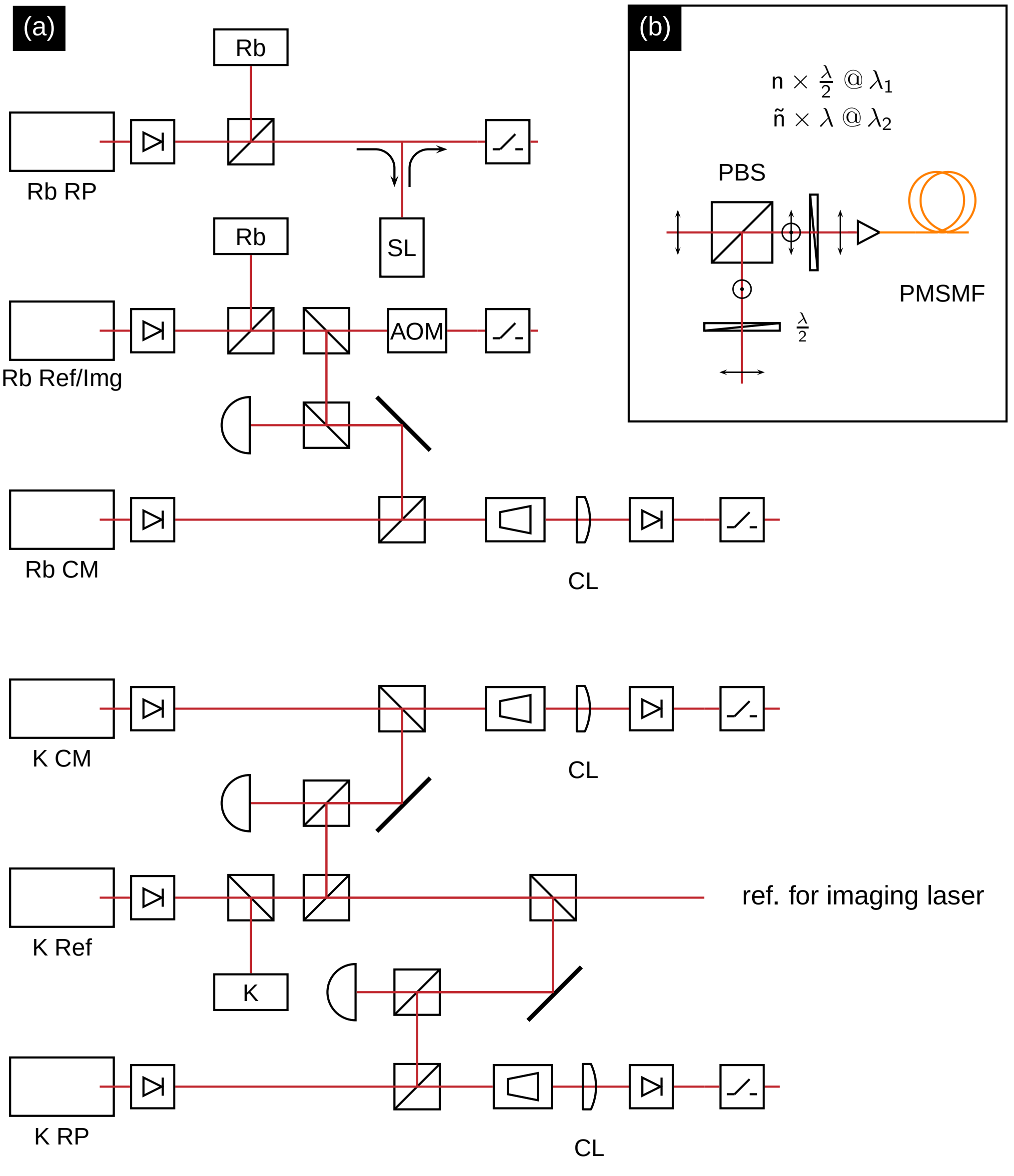
(a)
Rb
Rb RP
SL
Rb
AOM
Rb Ref/Img
Rb CM
CL
K CM
CL
ref. for imaging laser
K Ref
K
K RP
CL
(b)
n × $\frac{\lambda}{2}$ @ λ_1
ñ × λ @ λ_2
PBS
PMSMF
$\frac{\lambda}{2}$

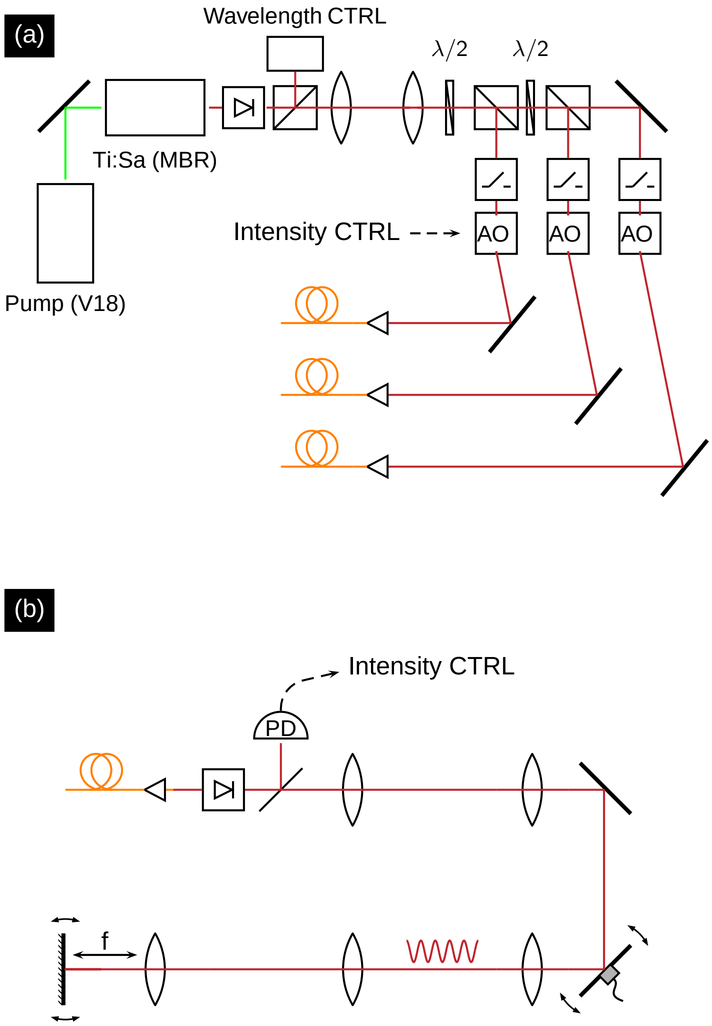

Figure 3: Simplified schematic of the optics setup used to provide the optical lattice. (a) All three lattice axes are derived from the same Ti:Sa laser (Coherent MBR), which is pumped by a Verdi V18 Yb:YAG laser. The beams for the individual axes are individually frequency-shifted and intensity controlled via acousto-optic modulators, and coupled into polarization-maintaining single-mode fibers. (b) Each lattice axis essentially consists of a beam-shaping telescope, followed by a second telescope, the focus of which is at the position of the optical lattice, and a retro-mirror in *cat's eye* configuration. A piezo-controlled mirror in conjunction with the retro mirror are used for alignment of the optical lattice. A pickup photodiode provides the feedback signal for light intensity regulation

Bibliography

[1] Albus, A., Illuminati, F., and Eisert, J.
Mixtures of bosonic and fermionic atoms in optical lattices.
Phys. Rev. A 68 (2003), 023606.

[2] Allen, L., and Eberly, J.
Optical resonance and two-level atoms. Dover Publications, 1987.

[3] Altman, E., Demler, E., and Lukin, M. D.
Probing many-body states of ultracold atoms via noise correlations.
Phys. Rev. A 70 (2004), 013603.

[4] Anderson, P. W.
Infrared catastrophe in Fermi gases with local scattering potentials.
Phys. Rev. Lett. 18 (1967), 1049.

[5] Ashkin, A., Dziedzic, J., Bjorkholm, J., and Chu, S.
Observation of a single beam gradient force optical trap for dielectric particles.
Opt. Lett. 11 (1986), 288.

[6] Aubin, S., Myrskog, S., Extavour, M. H. T., LeBlanc, L. J., McKay, D., Stummer, A., and Thywissen, J. H.
Rapid sympathetic cooling to Fermi degeneracy on a chip.
Nature Physics 2 (2006), 384.

[7] Bakr, W. S., Gillen, J. I., Peng, A., Fölling, S., and Greiner, M.
A quantum gas microscope for detecting single atoms in a Hubbard-regime optical lattice.
Nature 462 (2009), 74.

[8] Bakr, W. S., Peng, A., Tai, M. E., Ma, R., Simon, J., Gillen, J. I., Fölling, S., Pollet, L., and Greiner, M.

Probing the superfluidtoMott-insulator transition at the single-atom level.
2010.

[9] BELEMUK, A. M., AND RYZHOV, V. N.
On the critical temperature in a boson-fermion mixture with attraction between the components.
JETP Letters 87 (2008), 376.

[10] BELEMUK, A. M., RYZHOV, V. N., AND CHUI, S.-T.
Stable and unstable regimes in Bose-Fermi mixtures with attraction between components.
Phys. Rev. A 76 (2007), 013609.

[11] BERG, T.
Eine magneto-optische Falle für Kalium und Rubidium-Atome.
Diploma thesis, Johannes Gutenberg-Universität Mainz, 2005.

[12] BEST, T., WILL, S., SCHNEIDER, U., HACKERMÜLLER, L., VAN OOSTEN; DRIES, BLOCH, I., AND LÜHMANN, D.-S.
Role of interactions in ^{87}Rb-^{40}K Bose-Fermi mixtures in a 3d optical lattice.
Phys. Rev. Lett. 102 (2009), 030408.

[13] BJORKLUND, G. G.
Frequency-modulation spectroscopy: A new method for measuring weak absorptions and dispersions.
Opt. Lett. 5 (1980), 15.

[14] BLOCH, I., DALIBARD, J., AND ZWERGER, W.
Many-body physics with ultracold gases.
Rev. Mod. Phys. 80 (2008), 885.

[15] BONINSEGNI, M., KUKLOV, A. B., POLLET, L., PROKOF'EV, N. V., SVISTUNOV, B. V., AND TROYER, M.
Fate of vacancy-induced supersolidity in ^{4}He.
Phys. Rev. Lett. 97 (2006), 080401.

[16] BOURDEL, T., DONNER, T., RITTER, S., ÖTTL, A., KÖHL, M., AND ESSLINGER, T.
Cavity QED detection of interfering matter waves.
Phys. Rev. A 73 (2006), 043602.

[17] Braun, S.
Diploma thesis, Johannes Gutenberg-Universität Mainz.

[18] Bruderer, M., Bao, W., and Jaksch, D.
Self-trapping of impurities in Bose-Einstein condensates: Strong attractive and repulsive coupling.
Europhys. Lett. 82 (2008), 30004.

[19] Büchler, H., and Blatter, G.
Phase separation of atomic Bose-Fermi mixtures in an optical lattice.
Phys. Rev. A 69 (2004), 063603.

[20] Büchler, H. P., and Blatter, G.
Supersolid versus phase separation in atomic Bose-Fermi mixtures.
Phys. Rev. Lett. 91 (2003), 130404.

[21] Burt, E. A., Ghrist, R. W., Myatt, C. J., Holland, M. J., Cornell, E. A., and Wieman, C. E.
Coherence, correlations, and collisions: What one learns about Bose-Einstein condensates from their decay.
Phys. Rev. Lett. 79 (1997), 337.

[22] Campbell, G. K., Mun, J., Boyd, M., Medley, P., Leanhardt, A. E., Marcassa, L. G., Pritchard, D. E., and Ketterle, W.
Imaging the Mott insulator shells by using atomic clock shifts.
Science 313 (2006), 649.

[23] Campey, T., Vale, C. J., Davis, M. J., Heckenberg, N. R., Rubinsztein-Dunlop, H., Kraft, S., Zimmermann, C., and Fortágh, J.
Atom counting in ultracold gases using photoionization and ion detection.
Phys. Rev. A 74 (2006), 043612.

[24] Capogrosso-Sansone, B., Prokof'ev, N. V., and Svistunov, B. V.
Phase diagram and thermodynamics of the three-dimensional Bose-Hubbard model.
Phys. Rev. B 75 (2007), 134302.

[25] Cataliotti, F. S., Cornell, E. A., Fort, C., Inguscio, M., Marin, F., Prevedelli, M., Ricci, L., and Tino, G. M.

Magneto-optical trapping of fermionic Potassium atoms.
Phys. Rev. A 57 (1998), 1136.

[26] CATANI, J., DE SARLO, L., BARONTINI, G., MINARDI, F., AND INGUSCIO, M.
Degenerate Bose-Bose mixture in a three-dimensional optical lattice.
Phys. Rev. A 77 (2008).

[27] CHILD, M.
Molecular collision theory. Academic Press, 1974.

[28] COLOMBE, Y., STEINMETZ, T., DUBOIS, G., LINKE, F., HUNGER, D., AND REICHEL, J.
Strong atomfield coupling for Bose-Einstein condensates in an optical cavity on a chip.
Nature 450 (2007), 272.

[29] CRAMER, M.
Private communication.

[30] CRAMER, M., OSPELKAUS, S., OSPELKAUS, C., BONGS, K., SENGSTOCK, K., AND EISERT, J.
Do mixtures of bosonic and fermionic atoms adiabatically heat up in optical lattices?
Phys. Rev. Lett. 100 (2008), 140409.

[31] DAVIS, K., MEWES, M., ANDREWS, M., VANDRUTEN, N., DURFEE, D., KURN, D., AND KETTERLE, W.
Bose-Einstein condensation in a gas of Sodium atoms.
Phys. Rev. Lett. 75 (1995), 3969.

[32] DAVIS, K., MEWES, M., JOFFE, M., ANDREWS, M., AND KETTERLE, W.
Evaporative cooling of Sodium atoms.
Phys. Rev. Lett. 74 (1995), 5202.

[33] DE BOER, J. H., AND VERWEY, E. J. W.
Semi-conductors with partially and with completely filled 3D-lattice bands.
Proc. Phys. Soc. 49 (1937), 59.

[34] DE MILLE, D.
Quantum computation with trapped polar molecules.
Phys. Rev. Lett. 88 (2002), 067901.

[35] DeMarco, B., Rohner, H., and Jin, D. S.
An enriched ^{40}K source for fermionic atom studies.
Rev. Sc. Instr. 70 (1999), 1967.

[36] D'Errico, C.
Osservazione di risonanze di Fano-Feshbach in miscele atomiche K-Rb.
Master's thesis, Universit degli Studi di Firenze, 2005.

[37] Deuretzbacher, F., Plassmeier, K., Pfannkuche, D., Werner, F., Ospelkaus, C., Ospelkaus, S., Sengstock, K., and Bongs, K.
Heteronuclear molecules in an optical lattice: Theory and experiment.
Phys. Rev. A 77 (2008), 032726.

[38] Dickerscheid, D., Al Khawaja, U., van Oosten, D., and Stoof, H.
Feshbach resonances in an optical lattice.
Phys. Rev. A 71 (2005), 043604.

[39] Dickerscheid, D., van Oosten, D., Denteneer, P., and Stoof, H.
Ultracold atoms in optical lattices.
Phys. Rev. A 68 (2003), 043623.

[40] Dickerscheid, D., van Oosten, D., Tillema, E., and Stoof, H.
Quantum phases in a resonantly interacting boson-fermion mixture.
Phys. Rev. Lett. 94 (2005), 230404.

[41] Drever, R., Hall, J., Kowalski, F., Hough, J., Ford, G., Munley, A., and Ward, H.
Laser phase and frequency stabilization using an optical resonator.
Appl. Phys. B 31 (1983), 97.

[42] Dürr, S., Volz, T., Marte, A., and Rempe, G.
Observation of molecules produced from a Bose-Einstein condensate.
Phys. Rev. Lett. 92 (2004), 020406.

[43] Esslinger, T., Bloch, I., and W.Hänsch, T.
Bose-Einstein condensation in a quadrupole-Ioffe-configuration trap.
Phys. Rev. A 58 (1998), R2664.

[44] FALLANI, L., LYE, J. E., GUARRERA, V., FORT, C., AND INGUSCIO, M.
Ultracold atoms in a disordered crystal of light: Towards a Bose glass.
Phys. Rev. Lett. 98 (2007), 130404.

[45] FETTER, A. L., AND WALECKA, J. D.
Quantum Theory of Many-particle systems. Dover Publications, 2003.

[46] FISHER, M., WEICHMAN, P., GRINSTEIN, G., AND FISHER, D.
Boson localization and the superfluid-insulator transition.
Phys. Rev. B 40 (1989), 546.

[47] FÖLLING, S.
Probing Strongly Correlated States of Ultracold Atoms in Optical Lattices.
PhD thesis, Johannes Gutenberg Universität Mainz, 2008.

[48] FÖLLING, S., GERBIER, F., WIDERA, A., MANDEL, O., GERICKE, T., AND BLOCH, I.
Spatial quantum noise interferometry in expanding ultracold atom clouds.
Nature 434 (2005), 481.

[49] FÖLLING, S., WIDERA, A., MUELLER, T., GERBIER, F., AND BLOCH, I.
Formation of spatial shell structure in the superfluid to Mott insulator transition.
Phys. Rev. Lett. 97 (2006), 060403.

[50] GERBIER, F., TROTZKY, S., FÖLLING, S., SCHNORRBERGER, U., THOMPSON, J. D., WIDERA, A., BLOCH, I., POLLET, L., TROYER, M., CAPOGROSSO-SANSONE, B., PROKOF'EV, N. V., AND SVISTUNOV, B. V.
Expansion of a quantum gas released from an optical lattice.
Phys. Rev. Lett. 101 (2008), 155303.

[51] GERBIER, F., WIDERA, A., FÖLLING, S., MANDEL, O., GERICKE, T., AND BLOCH, I.
Interference pattern and visibility of a Mott insulator.
Phys. Rev. A 72 (2005), 053606.

[52] GERBIER, F., WIDERA, A., FÖLLING, S., MANDEL, O., GERICKE, T., AND BLOCH, I.

Phase coherence of an atomic Mott insulator.
Phys. Rev. Lett. 95 (2005), 050404.

[53] Gericke, T., Gerbier, F., Widera, A., Fölling, S., Mandel, O., and Bloch, I.
Adiabatic loading of a Bose-Einstein condensate in a 3D optical lattice.
J. Mod. Opt. 54 (2007), 735.

[54] Gericke, T., Würtz, P., Reitz, D., Langen, T., and Ott, H.
High-resolution scanning electron microscopy of an ultracold quantum gas.
Nature Physics 4 (2008), 949.

[55] Gerlach, W., and Stern, O.
Der experimentelle Nachweis der Richtungsquantelung im Magnetfeld.
Z. f. Physik 9 (1922), 349.

[56] Goldwin, J., Papp, S., DeMarco, B., and Jin, D.
Two-species magneto-optical trap with K-40 and Rb-87.
Phys. Rev. A 65 (2002), 021402R.

[57] Góral, K., Santos, L., and Lewenstein, M.
Quantum phases of dipolar bosons in optical lattices.
Phys. Rev. Lett. 88 (2002), 170406.

[58] Gottwald, T., and van Dongen, P.
Antiferromagnetic order of repulsively interacting fermions on optical lattices.
Phys. Rev. A 80 (2009), 033603.

[59] Greiner, M., Bloch, I., Hänsch, T., and Esslinger, T.
Magnetic transport of trapped cold atoms over a large distance.
Phys. Rev. A 6303 (2001), 031401R.

[60] Greiner, M., Mandel, O., Esslinger, T., Hänsch, T., and Bloch, I.
Quantum phase transition from a superfluid to a Mott insulator in a gas of ultracold atoms.
Nature 415 (2002), 39.

[61] Greiner, M., Mandel, O., Hänsch, T., and Bloch, I.
Collapse and revival of the matter wave field of a Bose-Einstein condensate.
Nature 419 (2002), 51.

[62] Grimm, R., Weidemüller, M., and Ovchinnikov, Y.
Optical dipole traps for neutral atoms.
Adv. At. Mol. Opt. Phys. 42 (2000), 95.

[63] Günter, K., Stöferle, T., Moritz, H., Köhl, M., and Esslinger, T.
Bose-Fermi mixtures in a three-dimensional optical lattice.
Phys. Rev. Lett. 96 (2006), 180402.

[64] Hackermüller, L., Schneider, U., Moreno-Cardoner, M., Kitagawa, T., Best, T., Will, S., Demler, E., Altman, E., Bloch, I., and Paredes, B.
Anomalous expansion of attractively interacting fermionic atoms in an optical lattice.
Science 327 (2010), 5973.

[65] Hall, J. L., Hollberg, L., Baer, T., and Robinson, H. G.
Optical heterodyne saturation spectroscopy.
Appl. Phys. Lett. 39 (1981), 680.

[66] Hanbury Brown, R., and Twiss, R. Q.
A test of a new type of stellar interferometer on Sirius.
Nature 178 (1956), 1046.

[67] Hanbury Brown, R., and Twiss, R. Q.
Interferometry of the intensity fluctuations in light. I. Basic theory: The correlations between photons in coherent beams of radiation.
Proc. R. Soc. Lond. 242 (1957), 300.

[68] Hanbury Brown, R., and Twiss, R. Q.
Interferometry of the intensity fluctuations in light. II. An experimental test of the theory for partially coherent light.
Proc. R. Soc. Lond. 243 (1958), 391.

[69] Hébert, F., Batrouni, G. G., Roy, X., and Rousseau, V. G.
Supersolids in one-dimensional Bose-Fermi mixtures.
Phys. Rev. B 78 (2008), 184505.

[70] Henny, M., Oberholzer, S., Strunk, C., Heinzel, T., Ensslin, K., Holland, M., and Schönenberger, C.
The fermionic Hanbury Brown and Twiss experiment.
Science 284 (1999), 296.

[71] Hentschel, M., Ulllmo, D., and Baranger, H. U.
Fermi edge singularities in the mesoscopic regime: Anderson orthogonality catastrophe.
Phys. Rev. B 72 (2005), 035310.

[72] Hofstetter, W.
Generalized numerical renormalization group for dynamical quantities.
Phys. Rev. Lett. 85 (2000), 1508.

[73] Hubbard, J.
Electron correlations in narrow energy bands.
Proc. R. Soc. Lond. 276 (1963), 238.

[74] Hudson, J. J., Sauer, B. E., Tarbutt, M. R., and Hinds, E. A.
Measurement of the electron electric dipole moment using YbF molecules.
Phys. Rev. Lett. 89 (2002), 023003.

[75] Iannuzzi, M., Orecchini, A., Sacchetti, F., Facchi, P., and Pascazio, S.
Direct experimental evidence of free-Fermion antibunching.
Phys. Rev. Lett. 96 (2006), 080402.

[76] Inouye, S., Goldwin, J., Olsen, M. L., Ticknor, C., Bohn, J. L., and Jin, D. S.
Observation of heteronuclear Feshbach resonances in a mixture of bosons and fermions.
Phys. Rev. Lett. 93 (2004), 183201.

[77] Jaksch, D., Bruder, C., Cirac, I., Gardiner, C., and Zoller, P.
Cold bosonic atoms in optical lattices.
Phys. Rev. Lett. 81 (1998), 3108.

[78] Jeltes, T., McNamara, J. M., Hogervorst, W., Vassen, W., Krachmalnicoff, V., Schellekens, M., Perrin, A., Chang,

H., Boiron, D., Aspect, A., and Westbrook, C. I.
Comparison of the Hanbury Brown-Twiss effect for bosons and fermions.
Nature 445 (2007), 402.

[79] Johnson, P., Tiesinga, E., Porto, J., and Williams, C.
Effective three-body interactions of neutral bosons in optical lattices.
N.J.P. 11 (2009), 093022.

[80] Jones, K. M., Tiesinga, E., Lett, P. D., and Julienne, P. S.
Ultracold photoassociation spectroscopy: Long-range molecules and atomic scattering.
Rev. Mod. Phys. 78 (2006), 483.

[81] Jördens, R., Strohmaier, N., Günther, K., Moritz, H., and Esslinger, T.
A Mott insulator of fermionic atoms in an optical lattice.
Nature 455 (2008), 204.

[82] Khaykovich, L., and Davidson, N.
Compression of a cold atomic cloud by on-resonance laser light.
J. Opt. Soc. Am.B 16 (1999), 702.

[83] Kim, E., and Chan, M.
Probable observation of a supersolid helium phase.
Nature 427 (2004), 225.

[84] Kittel, C.
Introduction to Solid State Physics. John Wiley & Sons, 1986.

[85] Klempt, C., Henninger, T., Topic, O., Scherer, M., Kattner, L., Tiemann, E., Ertmer, W., and Arlt, J. J.
Radio-frequency association of heteronuclear Feshbach molecules.
Phys. Rev. A 78 (2008), 061602.

[86] Klempt, C., Henninger, T., Topic, O., Will, J., Ertmer, W., Tiemann, E., and Arlt, J.
^{40}K-^{87}Rb Feshbach resonances: Modeling the interatomic potential.
Phys. Rev. A 76 (2007), 020701.

[87] Köhl, M., Moritz, H., Stöferle, T., Günter, K., and Esslinger, T.
Fermionic atoms in a three dimensional optical lattice: Observing Fermi surfaces, dynamics, and interactions.
Phys. Rev. Lett. 94 (2005), 080403.

[88] Köhler, T., Góral, K., and Julienne, P. S.
Production of cold molecules via magnetically tunable Feshbach resonances.
Rev. Mod. Phys. 78 (2006), 1311.

[89] Kohn, W.
Construction of Wannier functions and applications to energy bands.
Phys. Rev. B 7 (1973), 4388.

[90] Kozlov, M., and Labzowsky, L.
Parity violation effects in diatomics.
J. Phys. B 28 (1995), 1933.

[91] Lahaye, T., Menotti, C., Santos, L., Lewenstein, M., and Pfau, T.
The physics of dipolar bosonic quantum gases.
Rep. Prog. Phys. 72 (2009), 126401.

[92] LeBlanc, L. Hyperfine structure of 40K. report available online at http://www.physics.utoronto.ca/~jht/pubs.html, 2006.

[93] LeBlanc, L. J., and Thywissen, J. H.
Species-specific optical lattices.
Phys. Rev. A 75 (2007), 053612.

[94] Lewenstein, M., Santos, L., Baranov, M., and Fehrmann, H.
Atomic Bose-Fermi mixtures in an optical lattice.
Phys. Rev. Lett. 92 (2004), 050401.

[95] Liang, Z. X., Hu, B. B., and Wu, B.
Interaction effects on Wannier functions of a Bose-Einstein condensate in an optical lattice and implications for Bose-Hubbard model.
preprint online at arxiv:0903.4058.

[96] Lühmann, D.-S.
Private communication.

[97] Lühmann, D.-S., Bongs, K., Sengstock, K., and Pfannkuche, D.
Localization and delocalization of ultracold bosonic atoms in finite optical lattices.
Phys. Rev. A 77 (2008), 023620.

[98] LÜHMANN, D.-S., BONGS, K., SENGSTOCK, K., AND PFANNKUCHE, D.
Self-trapping of bosons and fermions in optical lattices.
Phys. Rev. Lett. 101 (2008), 050402.

[99] LUTCHYN, R. M., TEWARI, S., AND SARMA, S. D.
Boson Hubbard model with weakly coupled fermions.
Phys. Rev. B 78 (2008), 220504.

[100] MAJORANA, E.
Atomi orientati in campo magnetico variabile.
Nuovo Cimento 9 (1932), 43.

[101] MARTE, A., VOLZ, T., SCHUSTER, J., DÜRR, S., REMPE, G., VAN KEMPEN, E. G. M., AND VERHAAR, B. J.
Feshbach resonances in Rubidium 87: Precision measurement and analysis.
Phys. Rev. Lett. 89 (2002), 283202.

[102] MATHEY, L., ALTMAN, E., AND VISHWANATH, A.
Noise correlations in one-dimensional systems of ultra-cold fermions.
Phys. Rev. Lett. 100 (2008), 240401.

[103] MATHEY, L., DANSHITA, I., AND CLARK, C. W.
Creating a supersolid in one-dimensional Bose mixtures.
Phys. Rev. A 79 (2009), 011602.

[104] MEFFERT, B., AND HOCHMUTH, O.
Werkzeuge der Signalverarbeitung. Pearson, 2004.

[105] MERING, A., AND FLEISCHHAUER, M.
One-dimensional Bose-Fermi-Hubbard model in the heavy-fermion limit.
Phys. Rev. A 77 (2008), 023601.

[106] METCALF, H., AND VAN DER STRATEN, P.
Laser cooling and trapping. Springer, New York, 1999.

[107] MODUGNO, G.
Fermi-Bose mixture with tunable interactions.
Proc. Int. School of Physics "Enrico Fermi" - Course CLXIV "Ultra-Cold Fermi Gases" (2006).

[108] Modugno, M., Ferlaino, F., Riboli, F., Roati, G., Modugno, G., and Inguscio, M.
Mean-field analysis of the stability of a K-Rb fermi-Bose mixture.
Phys. Rev. A 68 (2003).

[109] Monroe, C., Swann, W., Robinson, H., and Wieman, C.
Very cold trapped atoms in a vapor cell.
Phys. Rev. Lett. 65 (1990), 1571.

[110] Mott, N.
The basis of the electron theory of metals, with special reference to the transition metals.
Proc. Phys. Soc. 62 (1949), 416.

[111] Naik, D. S., and Raman, C.
Optically plugged quadrupole trap for Bose-Einstein condensates.
Phys. Rev. A 71 (2005), 033617.

[112] Ni, K.-K., Ospelkaus, S., de Miranda, M. H. G., Pe'er, A., Neyenhuis, B., Zirbel, J. J., Kotochigova, S., Julienne, P. S., Jin, D. S., and Ye, J.
A high phase-space-density gas of polar molecules.
Science 322 (2008), 231.

[113] Orszag, M.
Quantum Optics. Springer, 1999.

[114] Ospelkaus, C., Ospelkaus, S., Ernst, P., Wille, O., Succo, M., Humbert, L., Sengstock, K., and Bongs, K.
Fermi-Bose mixtures in three-dimensional optical lattices.
In *Atomic Physics 20* (2006), vol. 869 of *AIP CONFERENCE PROCEEDINGS*, p. 219.

[115] Ospelkaus, C., Ospelkaus, S., Humbert, L., Ernst, P., Sengstock, K., and Bongs, K.
Ultracold heteronuclear molecules in a 3D optical lattice.
Phys. Rev. Lett. 97 (2006).

[116] Ospelkaus, S.
Quantum Degenerate Fermi-Bose Mixtures of ^{40}K *and* ^{87}Rb *in 3D Optical Lattices.*
PhD thesis, Universität Hamburg, 2006.

[117] OSPELKAUS, S., OSPELKAUS, C., HUMBERT, L., SENGSTOCK, K., AND BONGS, K.
Tuning of heteronuclear interactions in a degenerate fermi-Bose mixture.
Phys. Rev. Lett. 97 (2006), 120403.

[118] OSPELKAUS, S., PEER, A., NI, K.-K., ZIRBEL, J. J., NEYENHUIS, B., KOTOCHIGOVA, S., JULIENNE, P. S., YE, J., AND JIN, D. S.
Efficient state transfer in an ultracold dense gas of heteronuclear molecules.
Nature Physics 4 (2008), 622.

[119] ÖTTL, A., RITTER, S., KÖHL, M., AND ESSLINGER, T.
Correlations and counting statistics of an atom laser.
Phys. Rev. Lett. 95 (2005), 090404.

[120] POLLET, L., KOLLATH, C., SCHOLLWOECK, U., AND TROYER, M.
Mixture of bosonic and spin-polarized fermionic atoms in an optical lattice.
Phys. Rev. A 77 (2008), 023608.

[121] RAAB, E., PRENTISS, M., CABLE, A., CHU, S., AND PRITCHARD, D.
Trapping of neutral Sodium atoms with radiation pressure.
Phys. Rev. Lett. 59 (1987), 2631.

[122] RAMSAUER, C.
Über den Wirkungsquerschnitt der Gasmoleküle gegenüber langsamen Elektronen.
Annalen der Physik 369 (1921), 513.

[123] REFAEL, G., AND DEMLER, E.
Superfluid-insulator transition in Fermi-Bose mixtures and the orthogonality catastrophe.
Phys. Rev. B 77 (2008), 144511.

[124] REY, A. M., SATIJA, I. I., AND CLARK, C. W.
Hanbury Brown-Twiss interferometry for fractional and integer Mott phases.
N.J.P. 8 (2006), 155.

[125] RICCI, L., WEIDEMÜLLER, M., ESSLINGER, T., HEMMERICH, A., ZIMMERMANN, C., VULETIC, V., KÖNIG, W., AND HÄNSCH,

T. W.
A compact grating-stabilized diode laser system for atomic physics.
Opt. Comm. 117 (1995), 541.

[126] Ritter, S., Öttl, A., Donner, T., Bourdel, T., Köhl, M., and Esslinger, T.
Observing the formation of long-range order during Bose-Einstein condensation.
Phys. Rev. Lett. 98 (2007), 090402.

[127] Rittner, A. S. C., and Reppy, J. D.
Observation of classical rotational inertia and nonclassical supersolid signals in solid [sup 4]he below 250 mk.
Phys. Rev. Lett. 97 (2006), 165301.

[128] Roberts, J. L., Claussen, N. R., Cornish, S. L., Donley, E. A., Cornell, E. A., and Wieman, C. E.
Controlled collapse of a Bose-Einstein condensate.
Phys. Rev. Lett. 86 (2001), 4211.

[129] Rom, T.
Bosonische und fermionische Quantengase in dreidimensionalen optischen Gittern: Präparation, Manipulation und Analyse.
PhD thesis, Ludwig Maximilians Universität München, 2009.

[130] Rom, T., Best, T., Mandel, O., Widera, A., Greiner, M., Hänsch, T. W., and Bloch, I.
State selective production of molecules in optical lattices.
Phys. Rev. Lett. 93 (2004), 073002.

[131] Rom, T., Best, T., van Oosten, D., Schneider, U., Fölling, S., Paredes, B., and Bloch, I.
Free fermion antibunching in a degenerate atomic fermi gas released from an optical lattice.
Nature 444 (2006), 733.

[132] Roth, R., and Burnett, K.
Quantum phases of atomic boson-fermion mixtures in optical lattices.
Phys. Rev. A 69 (2004), 021601.

[133] Roulet, B., Gavoret, J., and P.Nozieres.
Singularities in the X-ray absorption and emission of metals.
Phys. Rev. 178 (1969), 1072.

[134] SAKURAI, J.
Modern Quantum Mechanics. Addison-Wesley, 1994.

[135] SCAROLA, V. W., DEMLER, E., AND SARMA, S. D.
Searching for a supersolid in cold-atom optical lattices.
Phys. Rev. A 73 (2006), 051601.

[136] SCHELLEKENS, M., HOPPELER, R., PERRIN, A., GOMES, J., BOIRON, D., ASPECT, A., AND WESTBROOK, C.
Hanbury Brown Twiss effect for ultracold quantum gases.
Science 310 (2005), 648.

[137] SCHNEIDER, U.
PhD thesis, in preparation, Johannes Gutenberg Universität Mainz.

[138] SCHNEIDER, U., HACKERMÜLLER, L., WILL, S., BEST, T., BLOCH, I., COSTI, T. A., HELMES, R. W., RASCH, D., AND ROSCH, A.
Metallic and insulating phases of repulsively interacting fermions in a 3D optical lattice.
Science 322 (2008), 1520.

[139] SCHÜNEMANN, U., ENGLER, H., GRIMM, R., WEIDEMÜLLER, M., AND ZIELONKOWSKI, M.
Simple scheme for tunable frequency offset locking of two lasers.
Rev. Sc. Instr. 70 (1999), 242.

[140] SIMONI, A., FERLAINO, F., ROATI, G., MODUGNO, G., AND INGUSCIO, M.
Magnetic control of the interaction in ultracold K-Rb mixtures.
Phys. Rev. Lett. 90 (2003), 163202.

[141] SPIELMAN, I. B., PHILLIPS, W. D., AND PORTO, J. V.
Mott-insulator transition in a two-dimensional atomic Bose gas.
Phys. Rev. Lett. 98 (2007), 080404.

[142] SPIELMAN, I. B., PHILLIPS, W. D., AND PORTO, J. V.
Condensate fraction in a 2D Bose gas measured across the Mott-insulator transition.
Phys. Rev. Lett. 100 (2008), 120402.

[143] STECK, D. Rubidium 87 D line data. Online report available at http://george.ph.utexas.edu/˜dsteck/alkalidata/, 2008.

[144] Stenger, J., Inouye, S., Stamper-Kurn, D. M., Miesner, H.-J., Chikkatur, A. P., and Ketterle, W.
Spin domains in ground-state Bose-Einstein condensates.
Nature 396 (1998), 345.

[145] Taglieber, M., Voigt, A.-C., Henkel, F., Fray, S., Hänsch, T. W., and Dieckmann, K.
Simultaneous magneto-optical trapping of three atomic species.
Phys. Rev. A 73 (2006), 011402.

[146] Tewari, S., Lutchyn, R., and Sarma, S. D.
Effects of a dilute gas of fermions on the superfluid-insulator phase diagram of the Bose-Hubbard model.
Phys. Rev. B. 80 (2009), 054511. arXiv:0902.0172.

[147] Titvinidze, I.
Private communication.

[148] Titvinidze, I., Snoek, M., and Hofstetter, W.
Supersolid Bose-Fermi mixtures in optical lattices.
Phys. Rev. Lett. 100 (2008), 100401.

[149] Titvinidze, I., Snoek, M., and Hofstetter, W.
Generalized dynamical mean-field theory for Bose-Fermi mixtures in optical lattices.
Phys. Rev. B 79 (2009), 144506.

[150] van Oosten, D.
Quantum gases in optical lattices: the atomic Mott insulator.
PhD thesis, Universiteit Utrecht, 2004.

[151] van Oosten, D., van der Straten, P., and Stoof, H.
Quantum phases in an optical lattice.
Phys. Rev. A 63 (2001).

[152] van Otterlo, A., Wagenblast, K.-H., Baltin, R., Bruder, C., Fazio, R., and Schön, G.
Quantum phase transitions of interacting bosons and the supersolid phase.
Phys. Rev. B 52 (1995), 16176.

[153] Volz, T., Syassen, N., Bauer, D., Hansis, E., Dürr, S., and Rempe, G.
Preparation of a quantum state with one molecule at each site of an

optical lattice.
Nature physics 2 (2006), 692.

[154] WERNER, F., PARCOLLET, O., GEORGES, A., AND HASSAN, S.
Interaction-induced adiabatic cooling and antiferromagnetism of cold fermions in optical lattices.
Phys. Rev. Lett. 95 (2005), 056401.

[155] WILL, S.
PhD thesis, in preparation, Johannes Gutenberg Universität Mainz.

[156] WILL, S., BEST, T., BRAUN, S., SCHNEIDER, U., AND BLOCH, I.
Coherent interaction of a single fermion with a small bosonic field.
Phys. Rev. Lett. 106 (2011), 115305.

[157] WILL, S., BEST, T., SCHNEIDER, U., HACKERMÜLLER, L., LÜHMANN, D.-S., AND BLOCH, I.
Time-resolved observation of coherent multi-body interactions in quantum phase revivals.
Nature 465 (2010), 197.

[158] WINKLER, K., LANG, F., THALHAMMER, G., V. D. STRATEN, P., GRIMM, R., AND DENSCHLAG, J. H.
Coherent optical transfer of Feshbach molecules to a lower vibrational state.
Phys. Rev. Lett. 98 (2007), 043201.

[159] WÜRTZ, P., LANGEN, T., GERICKE, T., KOGLBAUER, A., AND OTT, H.
Experimental demonstration of single-site addressability in a two-dimensional optical lattice.
Phys. Rev. Lett. 103 (2009), 080404.

[160] YANG, K.
Superfluid-insulator transition and fermion pairing in Bose-Fermi mixtures.
Phys. Rev. B 77 (2008), 085115.

[161] ZIRBEL, J. J., NI, K. K., OSPELKAUS, S., D'INCAO, J. P., WIEMAN, C. E., YE, J., AND JIN, D. S.
Collisional stability of fermionic Feshbach molecules.
Phys. Rev. Lett. 100 (2008), 143201.

[162] Zirbel, J. J., Ni, K.-K., Ospelkaus, S., Nicholson, T. L., Olsen, M. L., Julienne, P. S., and Wieman, C. E.
Heteronuclear molecules in an optical dipole trap.
Phys. Rev. A 78 (2008), 013416.